# UCSF
## UC San Francisco Electronic Theses and Dissertations

**Title**

Musculoskeletal Applications of Iron Loading for Stem Cell Tracking with Magnetic Resonance Imaging

**Permalink**

https://escholarship.org/uc/item/5wg5f9n7

**Author**

Saldanha, Karl Johann

**Publication Date**

2011

Peer reviewed|Thesis/dissertation

Musculoskeletal Applications of Iron Loading for Stem Cell Tracking with
Magnetic Resonance Imaging

by

Karl Johann Saldanha

DISSERTATION

Submitted in partial satisfaction of the requirements for the degree of

DOCTOR OF PHILOSOPHY

in

# Bioengineering

in the

GRADUATE DIVISION

of the

UNIVERSITY OF CALIFORNIA, SAN FRANCISCO

AND

UNIVERSITY OF CALIFORNIA, BERKELEY

**Acknowledgements**

In completing my PhD and throughout my educational career, there are numerous people that deserve my heartfelt thanks. As such, I would like to briefly acknowledge them for helping me to achieve this milestone.

I would first like to thank my advisor Dr. Sharmila Majumdar. I have spent a considerable amount of time in your lab, first as an undergraduate student, and then as a graduate student working towards my PhD. Thanks for giving me the freedom to explore new areas of research within the lab and for your continued support and guidance along the way. Your continued passion and excitement for research is inspiring and has motivated me a great deal in graduate school.

Next, I would like to thank my dissertation committee advisors, Dr. Tejal Desai, and Dr Benjamin Ma. Tejal, thanks for your advice and guidance on my research and for being my academic advisor. Ben, thanks very much for not only providing advice about my research, but also for being such a great physician in dealing with my various sports injuries. In addition, thanks to both of you for serving on my qualifying exam committee.

Thanks very much to Dr. Daniel Vigneron for serving as my qualifying exam chair, and for making it a challenging and rewarding process. I would also like to thank Dr. Xiaojuan Li for serving on my qualifying exam committee and for your advice about my research.

I would particularly like to thank Dr. Steven Conolly for your excellent mentorship during graduate school. I have enjoyed taking your classes, TAing for you, and talking with you about science, research, and life in general. Your support and advice throughout

iii

the members of the CPL, Krista McNally, Benjamin Rhau, Silinda Neou, and Ryan Quan for your all your help and assistance.

I would also like to acknowledge the great group of students in the UCB/UCSF Joint Graduate Group in Bioengineering. Samuel Tia, Anuj Patel, Zachary Lee, Gary Lee, Eric Jabart, and many others have helped to make graduate school a truly enjoyable experience.

I am especially grateful to my girlfriend Jennifer Luu. You are an amazing person, and I feel so fortunate to have you in my life. Thank you so much for believing in me and always being there to listen, support, and encourage me. Your motivation, intelligence, and dedication inspire me, while your sense of humor and sweetness always makes me smile. I love you.

My final thanks are reserved for my parents for their unconditional love and support throughout my life. Mom, thanks so very much for always trying to help in any way you can. I am extremely grateful to you for all the advice, encouragement, selflessness, and "comfort food". Dad, your work ethic, passion, and integrity have always served as a great inspiration to me. Thanks so much for your patience and for continually challenging me throughout my education. Lastly, thank you for instilling in me a life-long love of learning. To both my parents, I could not have done this without you!

# Musculoskeletal Applications of Iron Loading for Stem Cell Tracking with Magnetic Resonance Imaging

Karl Johann Saldanha

**Abstract**:

Stem cells have shown promise for tissue regeneration in a variety of pathological conditions. Specifically, mesenchymal stem cells have demonstrated the ability to promote tissue repair of the musculoskeletal system through differentiation along specific lineages including bone, cartilage, muscle, and fat. As part of the ongoing development of stem cell therapies and the gradual transition of these techniques into the clinic, it is crucial to be able to monitor these cells following implantation into the body. Magnetic resonance imaging (MRI) has the capability to provide *in vivo* non-invasive imaging of cells at multiple time points following implantation. As such, these research studies focus on the development of techniques to generate contrast between cells and the surrounding environment on MR images using iron-based methods. In particular, these studies focus on the application of such techniques to stem cell tracking for tissue engineering of the musculoskeletal system. The techniques investigated include cell loading with iron oxide-based contrast agents of various sizes as well as genetic engineering strategies to increase iron uptake through modified protein expression. Studies using iron oxides demonstrate the ability to non-toxically label cells, detect them via MRI, and quantitatively characterize signal loss associated with labeling. However, issues with excess particles following labeling could potentially hinder the accuracy of this approach. Furthermore, aggregation of excess particles during *in vitro* stem cell differentiation precludes the ability to utilize conventional staining techniques to assess the effect of labeling on differentiation capacity. Genetic engineering studies on (non-stem cell) mammalian cells

suggest no effect on iron uptake resulting from expression of the bacterial gene magA. However, ferritin up-regulation results in increased iron uptake in transiently transfected cells, but not enough to enable MRI detection. Further studies focused on generation of ferritin expressing stable cell lines as well as cells expressing gene combinations known to play a role in iron uptake are warranted. While significant research is still necessary before iron loading techniques can be transitioned into a clinical setting, the promising results of these studies and the clear potential benefits of its successful development are a strong motivation for continued investigation.

**Table of Contents**

---

**List of Tables**

## List of Figures

# Chapter 1: Introduction

## 1.1 Motivation

In recent years, the field of tissue engineering has rapidly expanded based on the development of techniques to improve or replace tissue function within various organ systems of the body. A major underlying supposition of this interdisciplinary field is that engineered techniques designed to mimic the body's own natural biological methods for tissue regeneration will yield the most effective therapeutic strategies in the clinic. Based on this understanding, one particularly large area of active research is the use of stem cells for tissue engineering purposes. Among the two major categories of stem cells, adult stem cells are a natural source of cells within the human body that are capable of self-renewal and differentiation along a variety of lineages. These properties along with the less controversial nature of their use compared to embryonic stem cells (ESCs) have made adult stem cells a major area of focus for cellular-based regeneration of a variety of tissue systems within the body.

In order to assess the effectiveness of stem cell-based therapies, it is important to be able to monitor stem cells after they have been implanted into the body. Ideally, it is important to be able to evaluate both the bio-distribution and functionality of stem cells implanted into the body for tissue regeneration purposes. This is important to determine both that implanted stem cells remain in the particular region of interest (ROI) and that they achieve the desired goals of implantation with minimal side effects. The research presented here focuses on the bio-distribution aspect of monitoring stem cell-based therapies, which has utility both in the further advancement of tissue engineering research and in the continually evolving use of stem cells within a clinical setting.

## 1.2    Thesis Aims

The overall purpose of this research work is to examine the use of magnetic resonance imaging (MRI) to track stem cells through the use of iron-based cell loading techniques. This includes studies based on two general strategies: (1) loading cells with various types of iron oxide contrast agents, and (2) genetically modifying cellular expression of genes that facilitate uptake and storage of iron within the cell. While stem cell-based therapies are applicable to a variety of tissue and organ systems within the body, this work focuses on the use of these techniques for MRI-based cell tracking of tissue regeneration within the musculoskeletal system. The layout of this work consists of a general background section, studies based on the use of nanometer-sized iron oxide particles, micrometer-sized iron oxide particle studies, genetic modification of cellular expression studies, and finally conclusions resulting from this research effort.

The primary contributions of this work include:

1) An analysis of the application of nanometer-sized iron oxide cell labeling to tracking of stem cells implanted for regeneration of the intervertebral disc (IVD).

2)  An analysis of the application of micrometer-sized iron oxide cell labeling to tracking of stem cells implanted for regeneration of articular cartilage and other musculoskeletal tissues.

3) A quantitative characterization of the loss in signal intensity (SI) associated with micrometer-sized iron oxide labeling at both 3 tesla (T) and 14T.

4) An examination of the feasibility of encoding mammalian cells to express bacterial genes important to the internalization and storage of iron, and a comparison to established techniques for up-regulating expression of mammalian genes responsible for iron storage and controlled release.

The background consists of:

**Chapter 2**, which provides an overview of stem cell-based therapies, their applications within a musculoskeletal tissue engineering setting, and an evaluation of current techniques for assessing stem cell-based therapies.

**Chapter 3**, which provides an overview of iron-based cell loading techniques including the use of iron oxide contrast agents of various sizes, the use of transfection agents to facilitate cellular uptake or iron oxide particles, and the use of techniques that genetically modify cells to increase their uptake of iron.

**Chapter 4**, which covers the basic principles of MRI, how quantitative parameters are derived from an MR image, and the effects of iron-based cell loading on resulting MR images.

The experimental section consists of:

**Chapter 5**, which focuses on research studies utilizing Feridex iron oxide nanometer-sized particles and the application of this cell tracking technique to tissue regeneration within the IVD.

**Chapter 6**, which focuses on research studies utilizing Bangs micrometer-sized iron oxide particles (MPIOs) and the application of this cell tracking technique to tissue regeneration of knee articular cartilage and other musculoskeletal tissues.

**Chapter 7**, which examines alternative techniques for cellular loading with iron by modulating expression of various bacterial and mammalian genes responsible for iron internalization and storage.

Lastly,

**Chapter 8** summarizes the results of this work, the resulting implications of this research, and future directions.

# Chapter 2: Background [1]—Stem Cell-based Therapies

## 2.1    Stem Cells

Stem cells are biological cells within multi-cellular organisms that are capable of both self-renewal and differentiation into specialized cell types that form various tissues within the body. Based on these characteristics, stem cell-based research has been a major area of focus as a potential strategy for repair and regeneration of diseased and damaged tissues. In general stem cells are distinguished as ESCs or adult stem cells. Table 2.1 outlines the major properties of ESCs and adult stem cells and highlights the main differences between the two types.

|  | ESCs | Adult Stem Cells |
|---|---|---|
| **Source** | -Isolated from the inner cell mass of a blastocyst (early stage embryo) | -Isolated from various tissues within the body throughout lifetime |
| **Potency** | -Pluripotent—capable of differentiation into any cell type | -Multipotent—capable of differentiation into multiple (but not any) cell type |
| **Renewal Capacity** | -Capable of self-renewal with the potential ability to overcome telomere shortening | -Capable of self-renewal but may be limited due to telomere shortening |
| **Immunogenicity** | -Based on isolation of ESCs from embryos, implantation is inherently allogenic which has potential immune rejection issues | -Cells can be isolated and implanted into the same patient limiting issues associated with immune rejection |
| ***In Vitro* Cell Culture** | -Generally requires culturing of cells on a feeder layer (e.g. mouse embryonic fibroblasts) <br> -Recently developed techniques enable culturing without a feeder layer | -Cells are cultured either in suspension or as a monolayer depending on adult stem cell type |
| **Controversy** | -Ethical issues associated with obtaining ESCs from embryos <br> -Federal limitations on the use of ESCs for research purposes | -No major ethical or regulatory issues involved with use for research purposes |

**Table 2.1—ESCs and adult stem cells: major properties and differences. (Table adapted from Palsson & Bhatia. Tissue Engineering. Prentice Hall 2004. Pages 61-73.)**

### 2.1.1   Mesenchymal Stem Cells (MSCs)

As multipotent cells, adult stem cells are present within the body and naturally function as a source of undifferentiated cells for the rejuvenation of tissue. As part of the body's own repair process, these cells can terminally differentiate along several specific lineage pathways in order to replenish dying cells and regenerate various tissues. Based on the ability to isolate these cells from patients, culture them *ex vivo*, and transplant them back into the body, adult stem cells are currently under investigation for their therapeutic potential. In pathological conditions where the body is unable to repair or regenerate tissue on its own, such stem cell-based therapeutic strategies have shown great promise. In particular, bone marrow-derived MSCs, a subset of adult stem cells, have demonstrated the ability to differentiate into a variety of connective tissue types including bone, cartilage, muscle, tendon, and fat (1). Figure 2.1 depicts the various lineages that MSCs are capable of differentiating into as well as the process by which MSCs commit to a specific lineage.
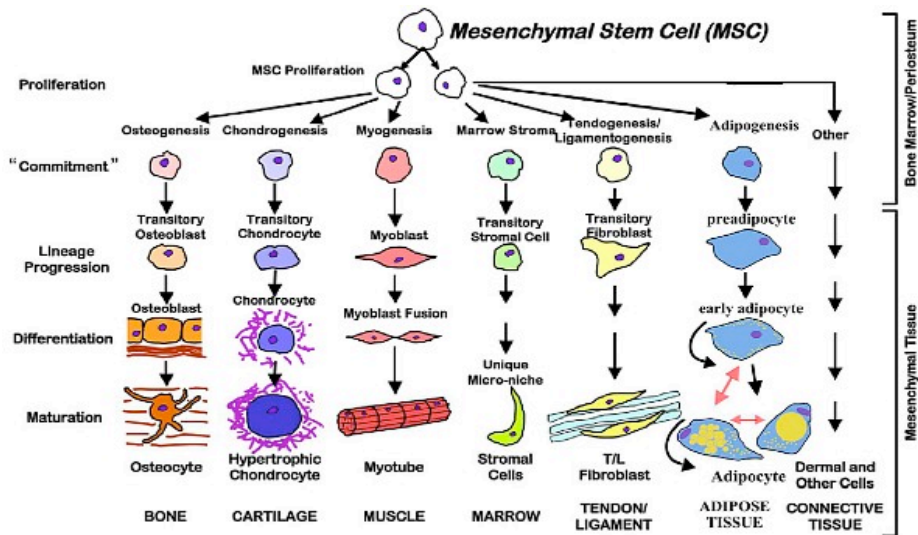


**Figure 2.1—Self-renewal and differentiation potential of MSCs. (Image obtained from Bonfield *et al.* (2))**

*2.1.2   Scaffold Support of MSCs*

6

For tissue engineering applications, MSCs generally require a scaffold support system that promotes 3D cell culture and tissue formation. Depending on the particular application, scaffolds are designed to promote any combination of the following (3):

    a.  Cell attachment, proliferation, differentiation, and migration

    b.  Delivery and maintenance of vital biochemical factors

    c.  Diffusion of cell nutrients, waste, and secreted cellular products

    d.  Influence over cell behavior through mechanical and biological cues

A variety of materials have been utilized as scaffolds for tissue engineering purposes and can be either synthetic or naturally derived (i.e. biologic). In some cases scaffolds can be a combination of both synthetic and biologically based components. Among the types of scaffolds utilized for tissue engineering with MSCs are fibrin-based natural gels and synthetic hydrogels.

Fibrin is a natural polymer formed by the polymerization of fibrinogen with thrombin (3). It is an attractive scaffold candidate because it can be made from autologous blood and is often used as a wound adhesive based on its strong biocompatibility. In addition, stem cells possess integrins that can bind directly to fibrin, and it is believed that fibrin may provide chemotactic and mitogenic stimuli for MSCs (4). Figure 2.2 from studies by Choi *et al*. depicts scanning electronic microscope images of cells encapsulated within a fibrin-based scaffold (5). A variety of studies have examined the use of fibrin as a scaffold for cell-based tissue engineering. For example studies by Dragoo *et al*. demonstrated the production of hyaline neo-cartilage in mice following implantation of stem cells suspended in a fibrin-based scaffold (6). Another study by Westreich *et al*.

demonstrated fibrin biocompatibility and formation of cartilage following autologous

implantation of constructs within the dorsum of immuno-competent rabbits (7).
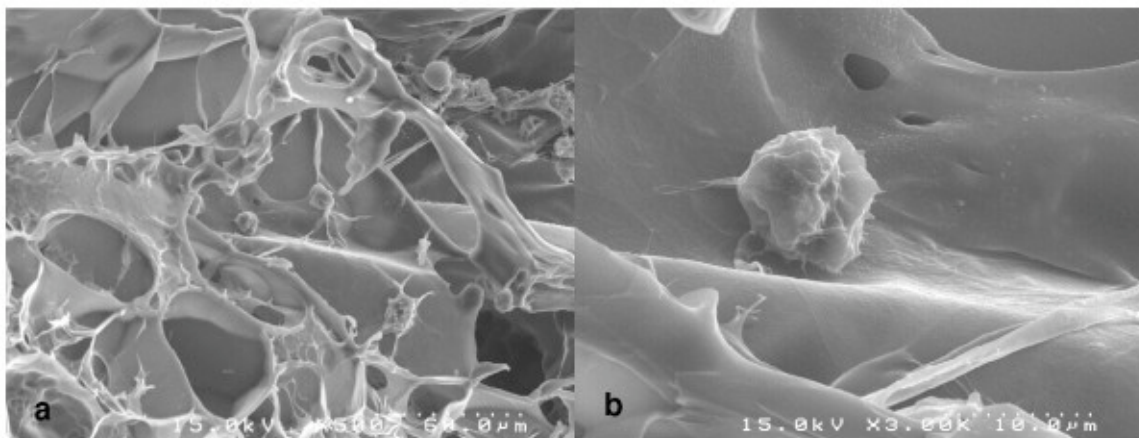


**Figure 2.2—SEM images showing the morphological structure of cells encapsulated within a fibrin-based gel. (a) x 500 (b) x 3000 (Image obtained from Choi *et al.* (5))**

Among the numerous synthetic scaffolds currently under investigation hydrogels

have several advantages that make them attractive for use in tissue engineering.

Hydrogels are cross-linked polymer structures that often have very high water content.

The process of cross-linking through a combination of hydrogen bonds, van der Waals

interactions, and ionic and covalent bonds forms an insoluble polymer. Depending on the

type of hydrogel, cross-linking can be initiated by exposure to changes in temperature,

ionic environment, chemical cross-linkers, or radiation (e.g. light). Hydrogels are capable

of facilitating mass transport of nutrients by matching the water content of the gels to the

tissue of interest. Another general advantage is the ability to encapsulate cells within the

hydrogel in liquid form (making *in vivo* injection easier) and then polymerizing the gel

upon exposure to appropriate conditions.

One particular type of hydrogel is composed of poly(ethylene glycol) (PEG). Figure

2.3 shows the chemical structure of PEG. PEG-based polymers, which are approved by

the Food and Drug Administration (FDA), consist of repeating ethylene oxide units

flanked on both ends by alcohols. The physical and chemical properties of the polymer can be modified by varying the molecular weight of the gel through the number of repeating subunits. PEG-based hydrogels have been well researched for musculoskeletal tissue applications, particularly in the area of cartilage tissue engineering (8,9), and recent studies are focused on understanding methods to control the mechanical properties and diffusion kinetics of PEG hydrogel constructs (10-12).
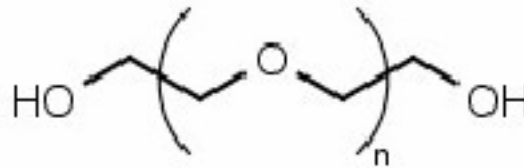
**Figure 2.3—Chemical structure of PEG. (Image obtained from http://www.glycosan.com/peg_science/what_peg.html)**

Another synthetic hydrogel utilized for tissue engineering applications is Puramatrix hydrogel, a commercially available synthetic polymer created by 3DM Inc. Puramatrix consists of a sequence of repeating amino acids that contain polar (hydrophilic) and non-polar (hydrophobic) surfaces. Upon exposure to physiological salt concentrations, the amino acids self assemble into β-sheets through hydrophobic interactions, as well as the formation of hydrogen and ionic bonds (Figure 2.4). The β-sheets then assemble into nano-fibers and eventually into a 3D structure with high water content and low (0.5-1%) peptide concentration. The use of Puramatrix as a scaffold for MSC-based tissue regeneration is a relatively new area of research, but results indicate MSC-Puramatrix implants are capable of promoting tissue regeneration in a variety of areas. For example, results by Henriksson *et al*. demonstrate survival of Puramatrix-encapsulated MSCs for

up to six week following *in vivo* implantation within a porcine IVD degeneration model (13). The implanted MSCs also showed positive markers for differentiation into disc cells during the time course of the study. Another study by Dickhut *et al*. demonstrates *in vitro* survival and chondrogenesis of MSCs when encapsulated within Puramatrix hydrogel (14).



Simple repeating aminoacid sequences    Self-assembled nanofibers
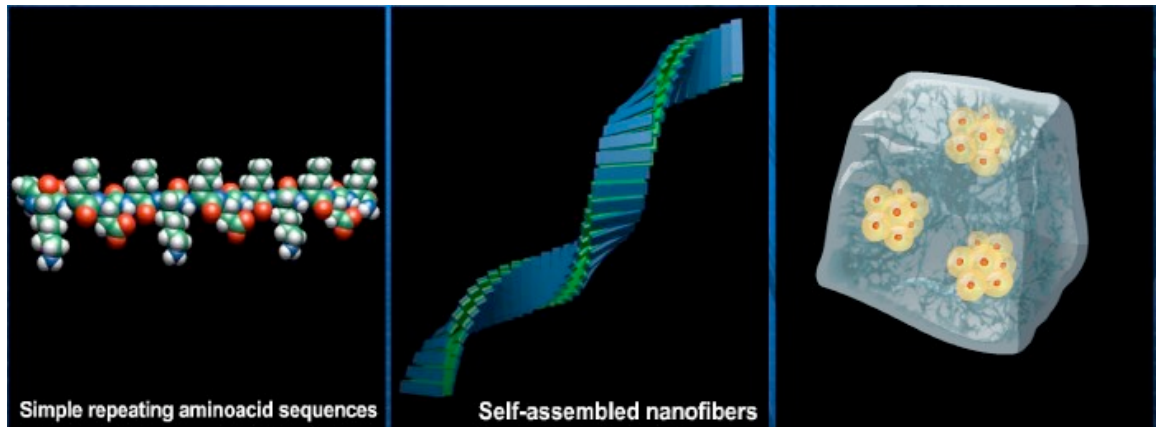
**Figure 2.4—Process of Puramatrix hydrogel formation upon exposure to physiological salt concentrations. The amino acid sequence self assembles into β-sheets which further assemble into nano-fibers and ultimately a 3-D structure with high water content. (Image obtained from http://www.puramatrix.com/tc01.html)**

## 2.2 Musculoskeletal Tissue Engineering with MSCs

Based on the their ability to differentiate into various types of connective tissue, MSCs continue to be investigated as a therapeutic strategy for regeneration of tissues present within the musculoskeletal system. In particular, MSC-based tissue engineering has shown promise in the ability to regenerate tissue within the intervertebral disc (IVD), as well as in the regeneration of hyaline articular cartilage within the knee.

### 2.2.1 MSC-based Tissue Engineering of the IVD

The IVD is made up of fibro-cartilaginous tissue and serves as a cushion to absorb shock and protect the vertebrae, brain, and important nerves of the body. The biology of

the IVD and the changes that occur with degeneration have been extensively reviewed (15,16). Briefly, IVD anatomy consists of an inner core known as the nucleus pulposus, and a surrounding firm ring of tissue called the annulus fibrosis (Figure 2.5). The nucleus consists of a hydrated gel, while the annulus is composed of tightly woven collagen fibers.

At the cellular level, the IVD consists of chondrocytes at the end-plates of the disc, chondrocyte-like cells in the nucleus pulposus, and fibroblast cells in the annulus fibrosis. The nucleus pulposus and annulus fibrosis contain abundant amounts of extracellular matrix (ECM) proteins, particularly collagens and proteoglycans (17). In addition the ECM also contains abundant amounts of water in both the nucleus pulposus (80%) and the annulus fibrosis (65%). The proteoglycans present in the disc are trapped within the network of collagen fibers and based on their negative charge facilitate the entry and exit of water during loading and unloading of the disc.
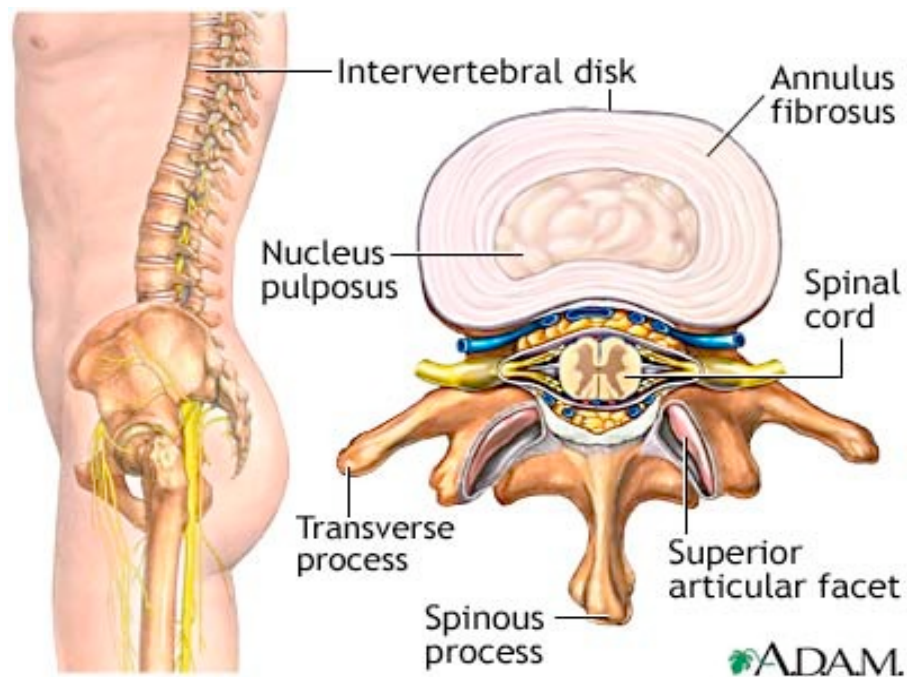


**Figure 2.5—Spinal cord and IVD anatomy. (Image obtained from http://healthguide.howstuffworks.com/intervertebral-disk-picture.htm)**

During degeneration there are a variety of morphological changes that occur (18,19). In general disc degeneration is characterized by a loss of cellularity and degradation of the ECM. In addition, the distinction between the nucleus pulposus and annulus fibrosis degrades, and the disc loses height, pressure, and hydration (20,21). These changes that occur during disc degeneration ultimately alter the morphological structure of the IVD, which affects the biomechanical properties of the disc in response to loading and unloading. Although clinically the link is poorly understood, IVD degeneration is postulated as a potential cause for chronic back pain (22), the leading cause of pain and disability in adults in the United States (23).

Since degradation of the ECM, in particular proteoglycans is known to be an early event in IVD degeneration, current biological therapies are aimed at ECM restoration. In particular, a variety of studies have investigated MSCs as a means of regenerating the IVD. For example, *in vitro* studies by Strassburg *et al*. demonstrate differentiation of MSCs into the nucleus pulposus phenotype after co-culture with nucleus pulposus tissue (24). Of particular importance is the fact that differentiation happened when MSCs were co-cultured with both normal and degenerated nucleus pulposus tissue. Furthermore, cells within the degenerated tissue also exhibited increased matrix gene expression as a result of MSC co-culture. In other studies, rabbit MSC implantation resulted in an increase in proteoglycan content (25,26), partial restoration of disc height and hydration (27,28), and differentiation into the chondrocyte/nucleus pulposus cell phenotype (28).

### 2.2.2   *MSC-based Tissue Engineering of Hyaline Articular Cartilage*

Hyaline (articular) cartilage lines the ends of bones, and allows for low friction motion of articulating surfaces. The main function of cartilage as a viscoelastic material

is variable load bearing through a range of motion and functional activities (29). Articular cartilage anatomy and the biology associated with maintaining its function has been extensively reviewed (29,30). Cartilage is composed of chondrocytes embedded within an ECM (Figure 2.6). The ECM is generated and maintained by the embedded chondrocytes and consists of numerous macromolecules including collagens, proteoglycans, and other proteins. The complex interaction between these proteins and tissue fluid are responsible for providing cartilage with its tensile strength, compressive strength, and resiliency (29,30).
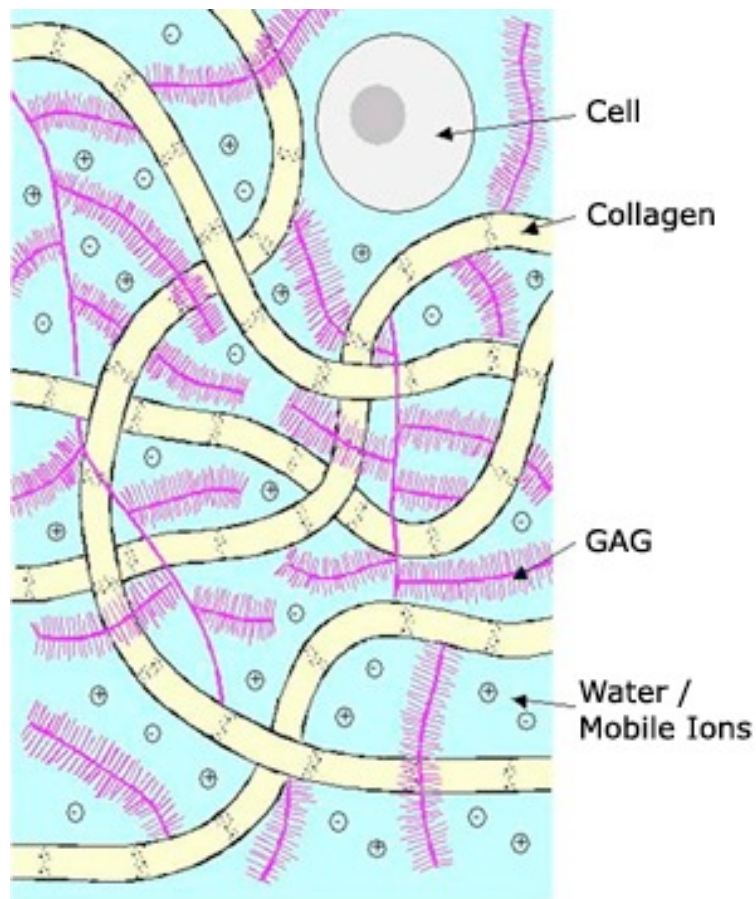


**Figure 2.6—Schematic of cartilage ECM organizational structure. (Image obtained from http://www.bidmc.org/Research/Departments/Radiology/Laboratories)**

Articular cartilage is comprised of four zones (Figure 2.7): superficial, middle, deep, and calcified cartilage (30). Chondrocyte size, shape, and metabolic activity vary within

the different zones. The superficial zone is the thinnest and forms the gliding surface of the joint. The main component of this zone is collagen arranged in fibrils parallel to the joint surface. The middle zone is thicker than the superficial zone and consists of larger collagen fibrils that do not have any distinct orientation. Within the deep zone collagen fibrils are once again oriented parallel to the cartilage surface. Lastly, within the zone of calcified cartilage, collagen fibrils insert into the calcified tissue, which serves to anchor the bone-cartilage interface and provide a mechanical transition between the two tissues. Of particular note, 95% of the collagen present within articular cartilage is Type II (31).
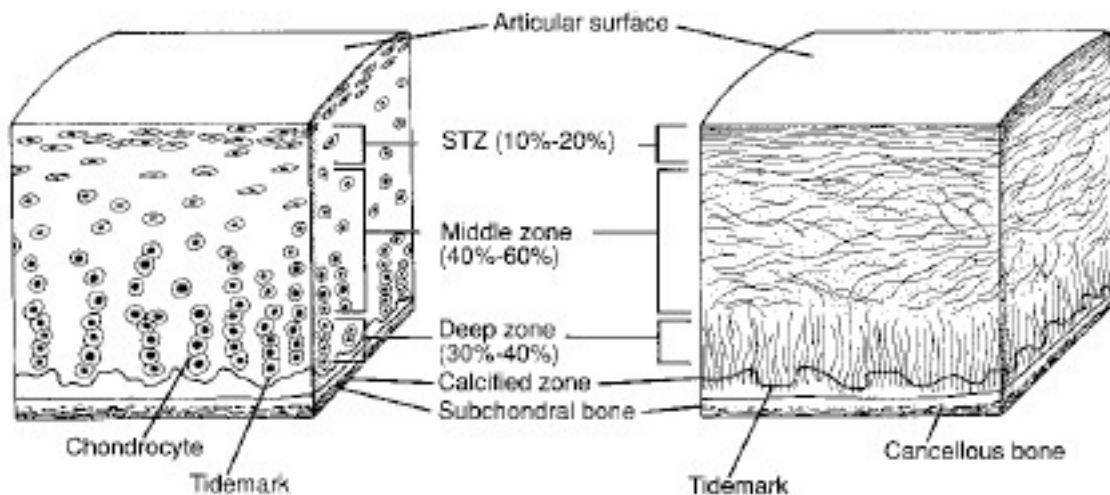


**Figure 2.7—Zonal organizational structure of articular cartilage. (Image obtained from Newman *et al.* (30))**

Proteoglycans are another important component of articular cartilage and are generally maintained by chondrocytes within the ECM. They often exist as aggregates, consisting of a centralized hyaluronic acid chain with proteoglycan monomers attached by way of specialized link proteins. The proteoglycan monomers in turn consist of a central protein core with multiple sulfated glycosaminoglycan (GAG) chains (e.g. chondroitin sulfate, keratin sulfate). These GAG chains are negatively charged, and hydrophilic in nature. Based on their negative charge, GAG chains repel each other,

14

which causes them to be maintained in a distended state. Figure 2.8 depicts the organizational structure of proteoglycans. Within the cartilage ECM, they are compressed by the surrounding collagen fibrils and maintained in a partially hydrated state. During loading, water is forced out of the ECM, and when the load is removed water returns via osmosis. The low permeability of cartilage prevents water from being rapidly squeezed out of the ECM and serves to protect the joint during high impact loading conditions (30).
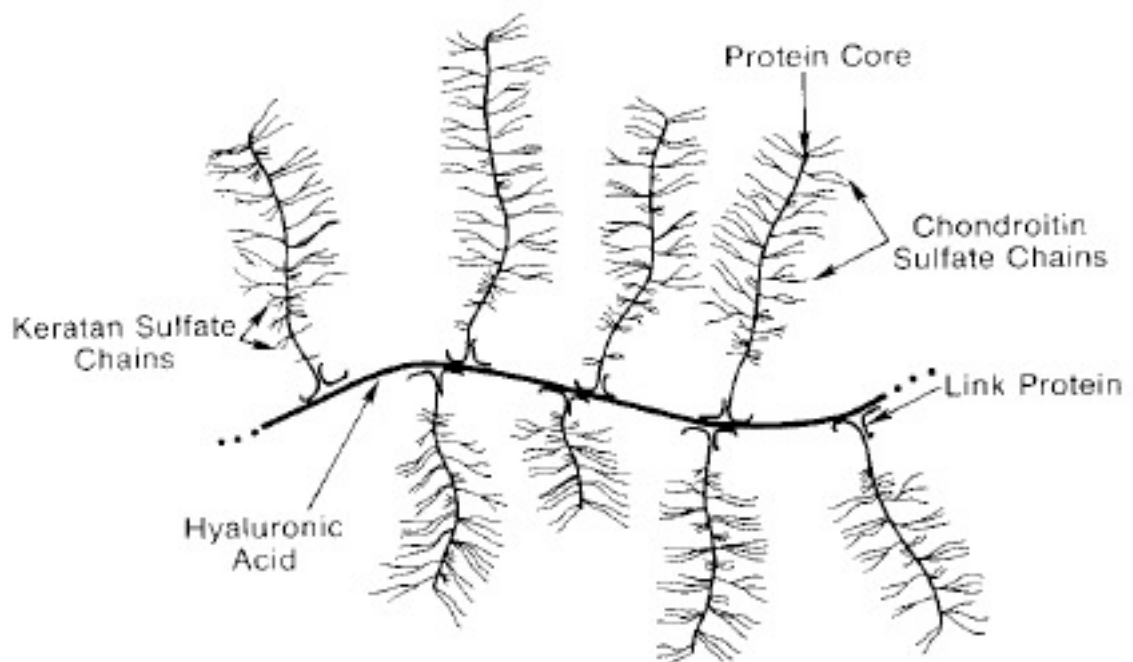


**Figure 2.8—Proteoglycan organizational structure. (Image obtained from Newman *et al.* (30))**

The intricate structure and biology of articular cartilage is limited in its ability to repair or regenerate, due to its avascularity, and the limited ability of mature chondrocytes to move within the ECM, proliferate, or alter their synthetic activity. This is particularly evident in the knee, where damage to hyaline articular cartilage present between the femur and tibia can cause significant pain during daily activities including walking. Over 15 million people worldwide suffer from knee joint failure resulting from

cartilage break down and its inability to self-repair. Figure 2.9 depicts the anatomy of the knee (left) along with an example of a cartilage defect (right).
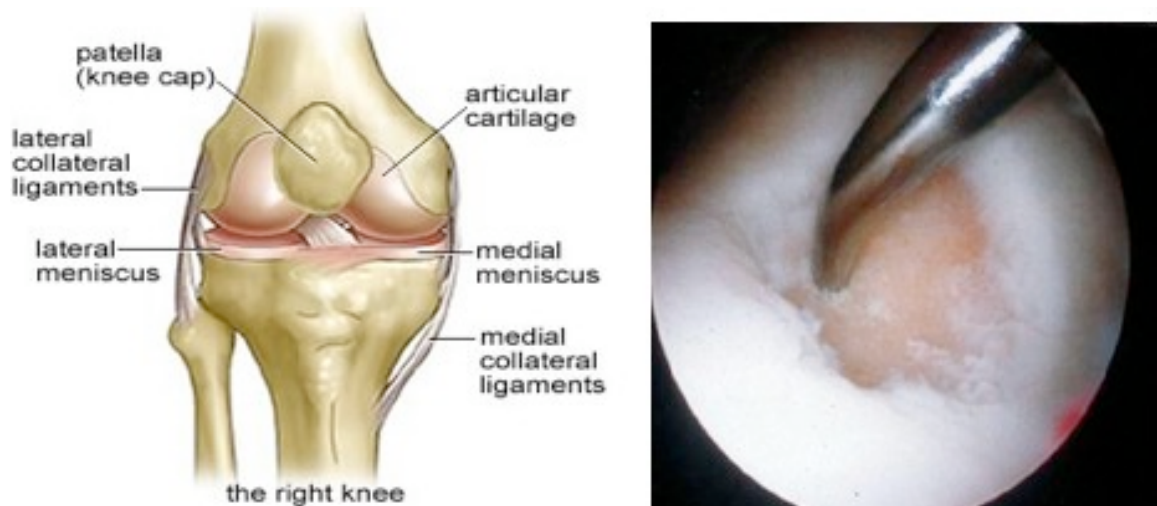


**Figure 2.9—Anatomy of the knee joint (left) and an example of a cartilage defect within a human knee (right). (Left image obtained from http://hubpages.com/hub/KNEE-Injuries. Right image obtained from Bentley *et al.* (32))**

Cartilage injury in the form of focal defects can be classified on a scale of increasing severity as a matrix disruption, partial thickness defect, or full thickness defect. In the case of matrix disruption, the ECM is damaged but if it is not too severe, nearby cells are able to increase their synthetic activity to repair the damaged area to its native state. The other two defects consist of a disruption to the cartilage surface that does not (partial thickness), or does (full thickness) penetrate to the sub-chondral bone. Hyaline cartilage has a limited ability to heal in response to damage. Depending on the extent of the defect, repair is sometimes initiated but not completed, or the repair tissue has an altered composition and weaker mechanical properties than native tissue (33). Over time this can lead to changes in joint loading and altered joint morphology, with the potential for development of osteoarthritis (OA).

Given the limited ability of cartilage to self-regenerate, MSC-based tissue engineering has been a major area of research, and could provide a method to repair damaged or diseased tissues. For example, studies by Williams *et al.* have demonstrated *in vitro* chondrogenic differentiation of MSCs as evidenced by positive staining for proteoglycan and collagen II, as well as quantitative increases in DNA, GAG content, and collagen content (9). *In vivo* studies using a rabbit osteochondral defect demonstrated the survival of implanted scaffold-encapsulated MSCs and the production of immature articular cartilage containing collagen II (34). In addition, synthetic ECM-encapsulated MSCs implanted within a similar *in vivo* rabbit model resulted in the formation of articular cartilage-like tissue and integration with the surrounding native cartilage (35).

## 2.3    Techniques for Assessing Stem Cell Therapies

The general paradigm for stem cell-based tissue engineering involves isolation of the stem cells from a patient, *ex vivo* expansion of the stem cells with optional exposure to special mechanical, chemical, or biological conditions, and subsequent implantation back into the body with the goal of regenerating tissue at the ROI. However, following implantation it is important to have a robust method of assessment for monitoring these cells. In an ideal case assessment should be able to monitor both the bio-distribution and function of implanted cells. Bio-distribution refers to the ability to continuously monitor the location of implanted cells, while functional assessment focuses on determining that the implanted cells behave functionally as expected without major toxic effects to the body.

*2.3.1    Limitations of Current Assessment Techniques*

17

At present, most stem cell-based tissue engineering is still conducted within a research setting, with the majority of *in vivo* work occurring within various animal models of disease and tissue damage. While a variety of assessment techniques following implantation are utilized, the most common techniques rely on histological staining in order to evaluate the effectiveness of stem cell-based therapies. While these techniques are able to provide both bio-distribution and functional information following implantation, they have significant limitations that prohibit their use within a clinical setting. Specifically, as demonstrated by Tatebe *et al*. (34) in order to detect the presence of cells within the ROI, *ex vivo* tissue specimens must be excised from the animal and prepared for visualization using microscopy. The implanted cells are identified via their ability to express a uniquely detectable marker.

While appropriate within a research setting, these techniques are not possible as a method of assessment in human patients for several reasons. First, histological techniques are highly invasive, often requiring the animal to be sacrificed and tissue samples excised prior to visualization of implanted cells. This method also generally requires fixing of the tissue and sample processing prior to visualization, which can often degrade the tissue. Secondly, these methods only allow for discontinuous assessment at a single time point. Essentially, the highly invasive process of visualization makes it impossible for therapy to continue and be assessed again at a later time point within the same individual. Lastly, histological analysis is fundamentally an *ex vivo* assessment, precluding the ability to monitor treatment *in vivo* within the intact organism. As such, in order for stem cell therapies to be clinically applicable, an alternative technique that allows for non-invasive *in vivo* detection and longitudinal tracking of implanted cells is warranted.

18

## 2.3.2 *MRI as a Technique for Stem Cell Bio-distribution Assessment*

MRI has several potential advantages that promote its use as a technique for assessing stem cell-based therapies following implantation into the body. Specifically, MRI is generally non-invasive and has no known harmful effects. Other advantages of MRI include its excellent soft tissue contrast, the ability to image at multiple time points (i.e. continuous assessment), and the ability to image in any plane (i.e. x, y, z, xy, xz, yz). Figure 2.10 shows an example MRI image of the knee along with its anatomical orientation within the body. In the MR image it is possible to clearly make out the region corresponding to bone, and the soft tissue areas corresponding to cartilage, muscle, and fat.
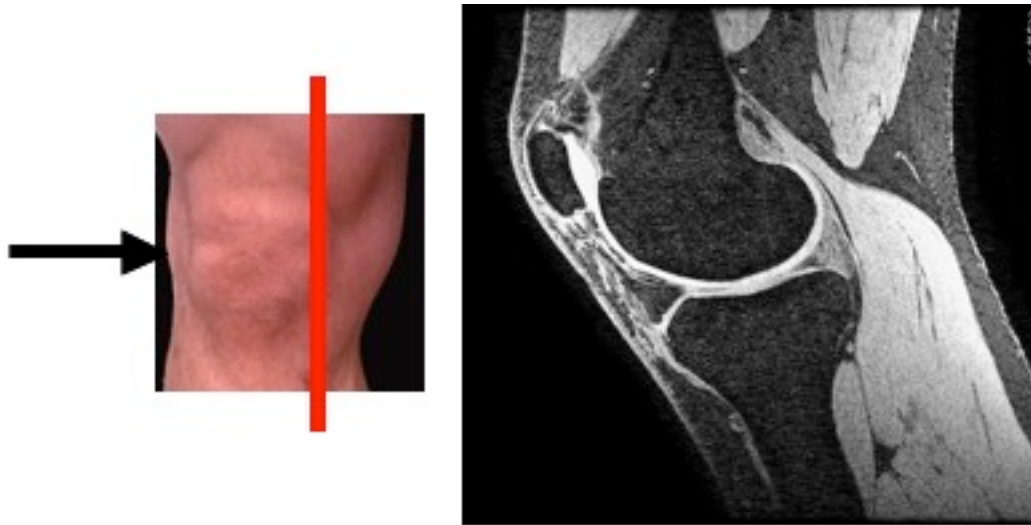


## Sagittal knee MRI

**Figure 2.10—Sagittal knee MR image (right) and anatomical orientation within the body (left). In the MR image it is possible to distinguish the regions corresponding to bone, cartilage, muscle, and fat.**

While ideally an assessment technique for stem cell-based tissue engineering should be able to provide both bio-distribution and functional information, the use of MRI is

generally limited to monitoring bio-distribution. However, analysis of the bio-distribution of stem cells can provide a wealth of information in the development of stem cell-based tissue engineering techniques, and in their transition into the clinic. First bio-distribution can provide information on migration of stem cells following implantation. Depending on the site of implantation it is important to know whether stem cells home to the ROI or travel to other potentially undesirable parts of the body. It is also possible to obtain residence information focused on whether stem cells remain at the ROI after implantation. This is important to assess whether stem cells remain at the ROI for a period of time long enough to initiate and sustain tissue regeneration. Lastly, through bio-distribution information it is possible to assess engraftment of stem cells into the native host tissue. This is important because the tissue formed by the implantation of stem cells should ideally integrate into the host tissue instead of remaining distinctly separate.

In order to utilize MRI as a technique for monitoring the bio-distribution of stem cells, it is necessary to have a way to distinguish the implanted cells from the surrounding host tissue. Armed with a technique for generating this required contrast it is possible to utilize MRI's inherent advantages for continuous non-invasive *in vivo* assessment of stem cell bio-distribution following implantation.

# Chapter 3: Background [2]—Iron-based Cell Labeling

In order to utilize MRI as a technique for monitoring the bio-distribution of stem cells following implantation, a variety of contrast-based techniques have been investigated within a research setting. Among the various types of contrast agents developed for use in MRI applications, iron oxide-based contrast agents have shown promise as a means of labeling cells and detecting them on MR images. Within this class of compounds, there are a variety of agents with different, sizes, chemical properties, and iron content. Other techniques that are similar in nature based on utilizing the same iron-based contrast mechanisms involve genetically modifying mammalian cells to modulate their uptake, storage, and processing of iron. These techniques span the manipulation of a variety of genes identified both in prokaryotic and eukaryotic cells. As such, the use of iron oxide-based contrast agents allows for control at the cellular level, while genetic modification techniques allow for control of iron uptake at an even lower level.

## 3.1    Iron Oxide-based Contrast Agents

Iron oxide-based agents generate contrast on MR images as a result of their strong magnetic properties. Iron oxides are compounds consisting of iron and oxygen, with magnetite ($Fe_3O_4$) being the most common form utilized for MR imaging applications. The crystal structure of magnetite is depicted in Figure 3.1, showing an orderly arrangement of the oxygen and iron atoms. Magnetite has a strong magnetic susceptibility ($\chi$) which when placed in an MR magnet results in a significant distortion in the homogeneity of the applied magnetic field (36). This distortion effect is exploited as the basis of generating contrast using iron oxide-based agents.
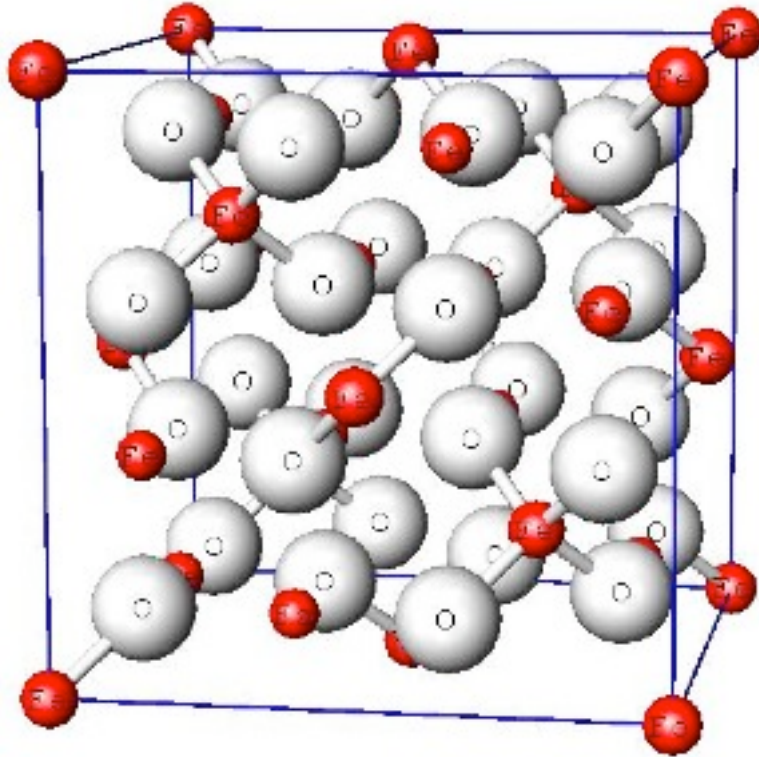
**Figure 3.1—Crystal structure of Magnetite (Fe₃O₄) showing the orderly arrangement of iron (red) and oxygen (white) atoms. (Image obtained from http://www.geocities.jp/ohba_lab_ob_page/structure6.html)**

These agents fall into a class of compounds known as superparamagnetic iron oxides (SPIOs). Paramagnetism is a form of magnetism that occurs only in the presence of an externally applied magnetic field (Figure 3.2). In the absence of a magnetic field thermal motion randomizes spin orientation, and the net magnetic moment averages to zero. However, in the presence of an external magnetic field the spins will align with the applied field resulting in a slight enhancement in the direction of the applied field. In general paramagnetic materials have a magnetic susceptibility ($\chi$) greater than one and thus enhance the applied field. When the external field is removed, paramagnetic materials do not remain magnetized as the spins return to a randomized orientation and the net magnetic moment once again averages to zero. An extension of this phenomenon is superparamagnetism, which is similar to paramagnetism except that instead of

individual atoms being independently influenced by the external field, the magnetic moment of the entire crystallite (e.g. Figure 3.1) aligns with the field.
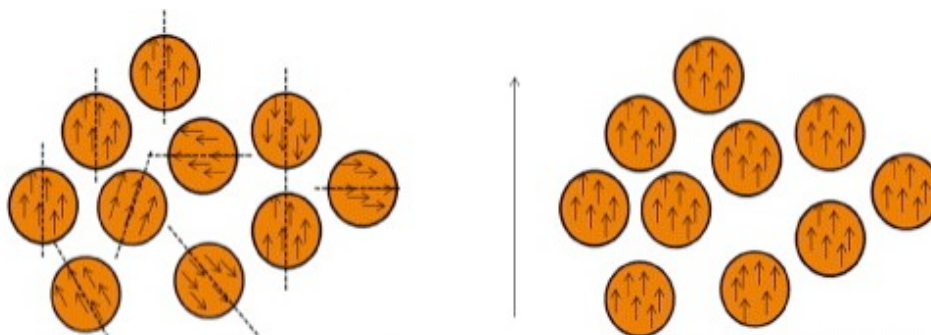


**Figure 3.2—Paramagnetic behavior in the absence (left) and presence (right) of an externally applied magnetic field. In the absence of a field the thermal motion randomizes spin orientation leading to a net zero magnetic moment. In the presence of an external field, the spins align and slightly enhance the applied field. When the applied field is removed, the net moment returns back to zero. (Image obtained from Demas *et al.* (37))**

In addition to characterizing the ability to label cells with iron-based contrast agents and detect them using MRI, it is also important to determine the effect of labeling on the functional capacity of the cells. This includes any toxicity to the cells resulting from iron oxide uptake as well as any potential inhibition of cellular proliferation following labeling. This is especially important in the case of stem cells because of the need for cells to divide into the appropriate number of cells necessary for tissue regeneration purposes. Another important consideration specific to stem cell tracking is the effect of labeling on the ability of cells to differentiate into other cell types. Specifically in the case of MSCs, iron oxide labeling should not inhibit the ability of cells to differentiate into cell types responsible for musculoskeletal tissue formation such as adipogenic, chondrogenic, and osteogenic lineages.

*3.1.1   Nanometer-sized Iron Oxide Particles*

Distinctions between different types of SPIO particles are often made based on the size of the particles used for cell labeling. The most common SPIO particles utilized are generally in the nanometer size range. These particles generally contain an iron oxide core (e.g. magnetite) that is less than 10 nm in size, and are solubilized by adding a coating of hydrophilic polymers such as dextran (Figure 3.3). With the addition of the polymer coating, the size of the encapsulated particles ranges from approximately 10-300 nm in size depending on the specific iron oxide contrast agent used (38).

Phagocytic cells such as macrophages have demonstrated the ability to readily take up iron oxide particles (39). However other cell types including stem cells do not readily take up SPIOs without the presence of a transfection agent (TA) (40). This is in large part due to the negative zeta potential of the SPIO particles, which inhibits the necessary interactions with the cellular surface to promote efficient uptake of the SPIOs by non-phagocytic cells (41). Zeta potential is a measurement of electric potential difference at the interface between two substances in a colloid and is commonly used as a measurement of the stability of a mixture.
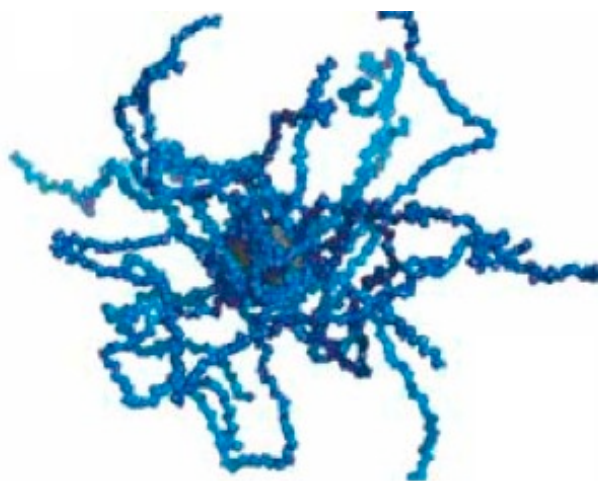


**Figure 3.3—Diagram modeling the structure of a nanometer-sized SPIO. The iron oxide core is solubilized by addition of a hydrophilic polymer coating such as dextran. (Image obtained from http://www.european-hospital.com/en/article/267-Molecular_MRI.html)**

Using a TA allows non-phagocytic cells to internalize SPIO particles by facilitating a positive zeta potential in the contrast agent-TA complex through electrostatic interactions between the two agents (42). The general procedure for cellular uptake of SPIOs combined with a TA is depicted in Figure 3.4. The SPIO particles are mixed with the transfection agent resulting in complex formation. This newly formed complex has a positive zeta potential and can be taken up by non-phagocytic cells such as stem cells. The uptake process is facilitated by mixture of the complex in the media used to culture the cells for a period of 18-24 hours. During this time, the iron oxide contrast agent is taken up and localized within cellular endosomes often by way of receptors on the cell surface.
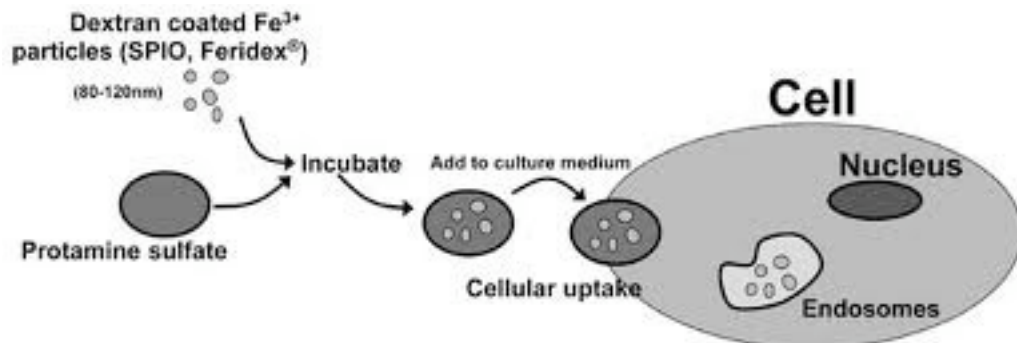


**Figure 3.4—Diagram depicting the cellular uptake process of SPIOs combined with a TA (protamine sulfate). Incubation of cells with the contrast agent and TA complex results in cellular uptake and incorporation within endosomes. (Image obtained from Guzman *et al.* (43))**

Labeling cells with nanometer-sized SPIOs for tracking via MRI has been demonstrated for a variety of cell types and disease conditions (44). For example Hoehn *et al.* demonstrated the ability to label ESCs with an SPIO contrast agent using Lipofectin as a TA and a 24-hour incubation (45). Following labeling, the labeled ESCs were tracked for up to three weeks in a rat model of ischemia. In particular, the results demonstrated the ability to monitor migration of the stem cells from the implantation site

to the area of brain tissue damage. In another study, cells labeled with SPIOs and the TA poly-L-lysine were attracted to the liver by using an external magnet (46). The presence of the magnet caused labeled cells to migrate to the liver and were detected using MR imaging for up to 4 weeks following implantation. In another disease model study, SPIO-labeled pancreatic islet cells were detected using 3T MRI following *in vivo* implantation within the liver of diabetic rats (47).

Focusing on MSC–labeling with SPIO particles, a variety of studies have demonstrated the ability to non-toxically label cells and detect them using MRI. Reddy *et al*. demonstrated the ability to effectively label MSCs with chitosan-coated SPIO particles and detect them within a rat model of ischemia using serial *in vivo* MRI. Using this particular contrast agent resulted in 100% labeling of MSCs without noticeable toxic effects or alterations to the differentiation capacity of the SPIO-labeled cells (48). In another study Addicott *et al*. demonstrated the ability to label MSCs with a SPIO-based contrast agent and quantitatively characterized the *in vitro* detection of labeled cells using MRI (49). One particularly important point about this study is that the contrast agent was designed to promote cellular uptake in non-phagocytic cells without the need for a TA.

Of the various iron oxide-based contrast agents available, one major SPIO utilized in MRI is Feridex. This FDA approved contrast agent was originally developed for imaging disease (e.g. cancer) and damage of the liver (50,51). However, a variety of studies have demonstrated the ability to label multiple cell types utilizing Feridex in combination with a TA. For example, Cohen *et al*. have demonstrated the ability to label neural precursor cells with complex consisting of Feridex and poly-L-lysine (52). Labeled cells exhibited the ability to migrate within brain tissue, differentiate into the appropriate cells within the

brain, and be detected via MRI for up to one week following implantation. In studies by Ke *et al*., bone marrow-derived neural stem cells labeled with a similar Feridex and poly-L-lysine complex were detected *in vivo* within a rhesus monkey model of brain tissue regeneration for up to 8 weeks following implantation (53).

In particular, Feridex has been utilized to label MSCs and for monitoring stem cell-based regeneration of the musculoskeletal system. Arbab *et al*. showed the ability to effectively label MSCs with a Feridex and protamine sulfate (Fe-Pro) complex using an overnight incubation procedure (54). In addition labeling of MSCs did not have any impact on the ability of cells to proliferate or differentiate along chondrogenic or adipogenic lineages. In a complementary study by Pawelcyzk *et al*., MSC labeling with Fe-Pro resulted in increased sustained expression of genes responsible for iron uptake, storage, and processing within the cell (55). This indicates that in addition to regular cellular uptake, MSCs modulated their protein expression levels in order to handle increased iron load following labeling.

### 3.1.2    *Micrometer-sized Iron Oxide Particles (MPIOs)*

In contrast to conventional nanometer-sized iron oxide particles, MPIOs are generally two orders of magnitude larger in size (i.e. ~ 1-5 μM). These commercially available iron oxide particles are also superparamagnetic in nature, and consist of a magnetite core encased within an inert divinyl benzene shell (Figure 3.5). In addition, these particles contain a Dragon Green fluorescent tag that can be used for optional microscopy co-localization studies. The particles are created by expanding the polymer shell using an organic solvent, adding as much fluorophore and iron oxide as possible, and shrinking the shell by replacing the solvent with a sterile aqueous solution (56).
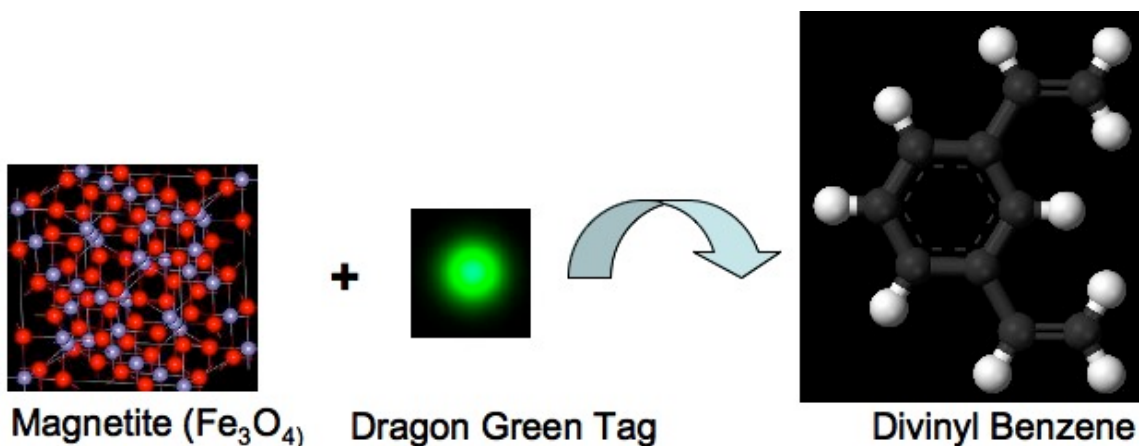
**Figure 3.5—Diagram depicting the components present within commercially available MPIOs from Bangs Labs. The iron oxide (magnetite) core is combined with a Dragon Green fluorescent tag and encased within an inert divinyl benzene shell. (Image adapted from http://uk.ask.com/wiki/Category:Iron_compounds, and http://en.wikipedia.org/wiki/Divinylbenzene)**

These particles were originally developed for diagnostic applications involving separation of cells and bio-molecules. These applications include antibody isolation, bio-assays, mRNA purification, and suspension arrays. However, due to their high iron oxide content they have proved suitable for cell labeling and tracking via MRI.

Focusing on the application of MPIOs to MRI-based cell tracking, these particles have been utilized for a variety of applications. For example, Tang *et al*. demonstrated the ability to label monocytes and neutrophils both *in vitro* and in *ex vivo* blood samples (57). Cells labeled *ex vivo* could be detected using MR imaging, but *in vivo* injection of MPIO particles did not result in *in situ* uptake of the contrast agent by monocytes or neutrophils. In another study, Rohani *et al*. showed the ability to successfully monitor MPIO-labeled dendritic cells *in vivo* for up to one week following implantation into mice (58). Labeling did not result in any toxic effects to the cells but did alter markers of dendritic cell activation and maturation. Among the variety of cell types that can be labeled with MPIOs, several studies have demonstrated the ability to successfully label

28

MSCs. For example, Chen *et al*. showed the ability to label neonatal rat MSCs with MPIOs and follow their migration to the site of brain injury using *in vivo* MRI (59). In addition, MPIO-labeled cells retained their differentiation potential.

## 3.2    Genetic Modification of Iron Uptake

An alternative method for generating contrast between implanted cells and surrounding tissue is to genetically modify cellular uptake of iron. This can be accomplished utilizing a variety of techniques aimed at controlling the expression of genes responsible for iron incorporation, processing, storage, and release. This process involves identifying the exact sequence for the gene of interest, inserting the sequence within an expression vector and utilizing a TA to transfect the gene into the cell of interest. This cloning technique can be utilized to express both prokaryotic and eukaryotic genes within mammalian cells (e.g. stem cells) and is a major foundation of molecular biology.

### 3.2.1   Molecular Cloning Techniques

Recombinant DNA (rDNA) contains DNA from two different sources. This usually consists of the specific gene of interest that needs to be expressed and a host vector that is utilized to introduce the DNA into the cell for expression. The most common type of vector used is a plasmid, which consists of an accessory ring of DNA found in bacteria that is separate from the bacterial chromosome and can replicate independently. Once transfected into a mammalian cell the plasmid contains the appropriate machinery for expression of the gene of interest. This results in transient expression but various techniques can be utilized to select for cells stably expressing the gene of interest.  Figure

3.6 depicts the general molecular cloning procedure for producing a plasmid containing a gene of interest.
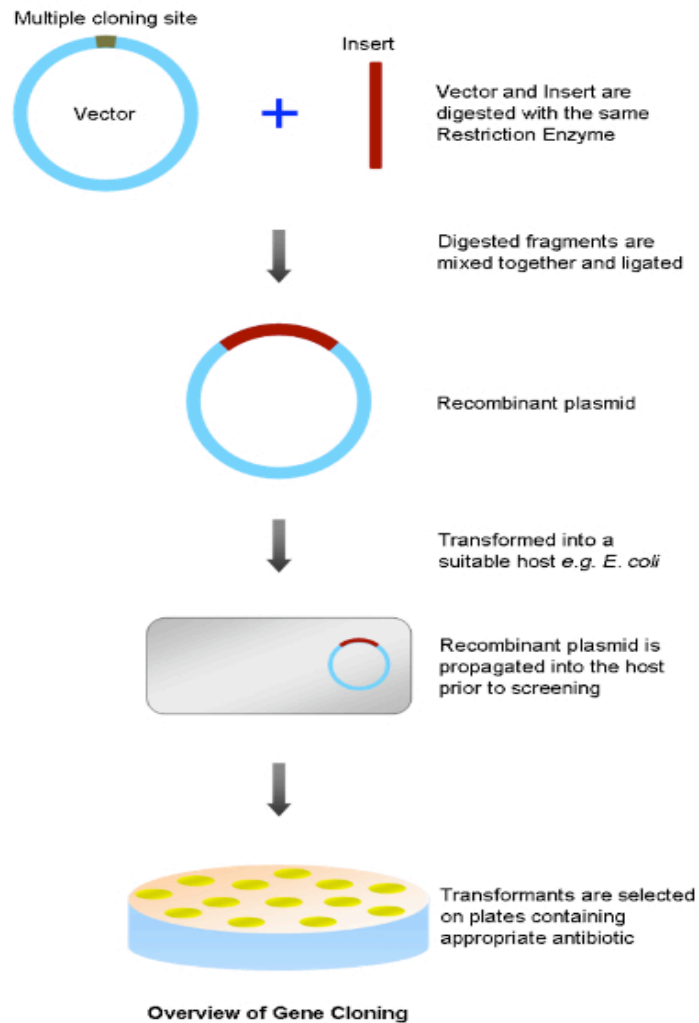


**Figure 3.6—Basic molecular cloning technique for producing a plasmid vector containing a gene of interest for expression in mammalian cells. (Image obtained from http://molecularhub.com/category/gene-cloning/)**

The first step in the process is to identify the gene sequence of interest that needs to be inserted into the plasmid. Once the gene is identified, primers specific for the gene must be designed so that the gene sample can be amplified using polymerase chain reaction (PCR). PCR generates multiple copies of the specific gene of interest which is then gel purified to isolate these specific DNA strands from undesired PCR product. Prior to

30

insertion of the purified DNA into the plasmid, restriction enzymes are used to cut open

the plasmid and the gene of interest at the appropriate location for insertion. Restriction

enzymes are proteins that recognize specific base pair sequences (~ 5 bases in length) and

cut DNA wherever the sequence is found within a template. Figure 3.7 shows an example

plasmid vector with restriction enzymes used for gene insertion.
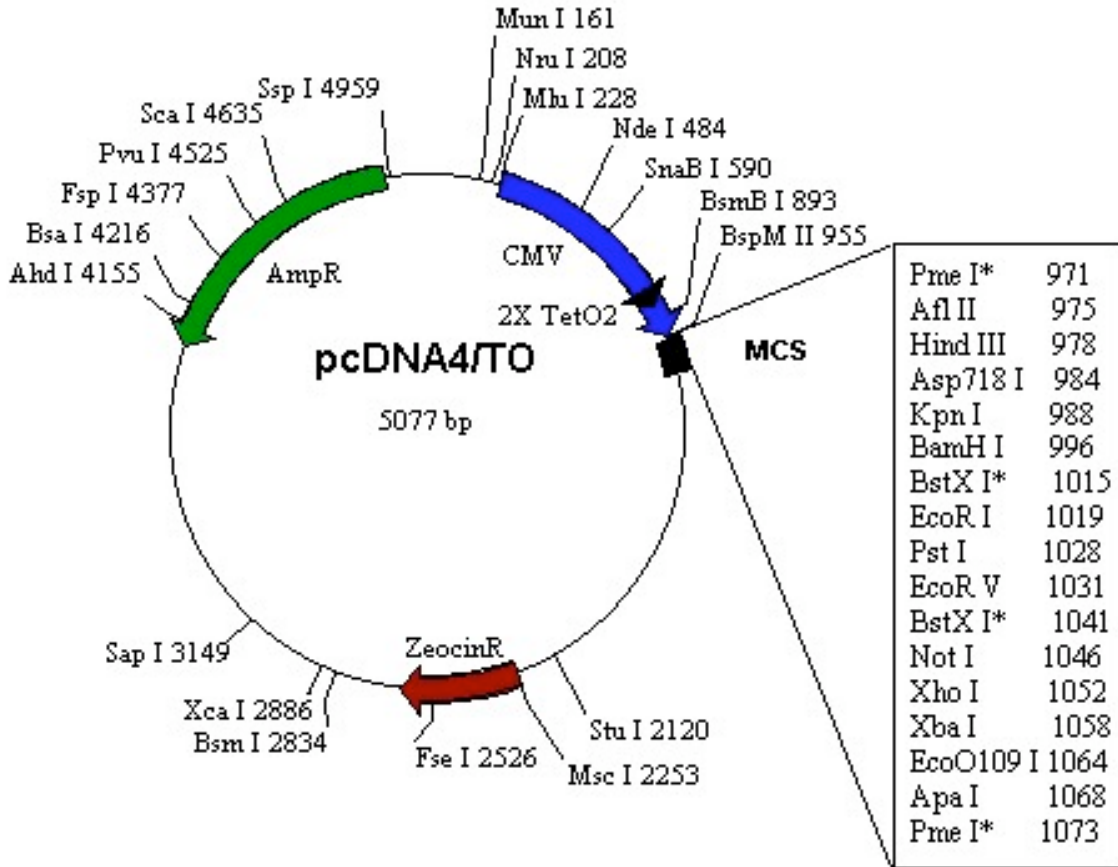


**Figure 3.7—Example of a plasmid vector (pcDNA4) showing the MCS where gene insertion occurs with the appropriate restriction enzymes. (Image obtained from http://www.biocenter.helsinki.fi/bi/peranen/Kotisivunlinkit/Vectors/pcDNA4TO.ht m)**

Within the plasmid, the multiple cloning site (MCS) is the region of the sequence where

gene insertion occurs. Restriction enzymes are located within the MCS and are matched

with the specific restriction sites flanking the gene of interest. Another important feature

present within most plasmids is a gene encoding for antibiotic resistance. In Figure 3.7 the plasmid contains a gene for resistance against the drug Zeocin.

Once the gene of interest has been inserted in the plasmid vector, transformation occurs in which the plasmid is inserted into competent host bacterial cells (e.g. *E. coli*). Once transformed, the host bacterial cells are plated on agar plates and allowed to grow for a period of time (~ 18 hours). During this period the bacterial cells rapidly divide resulting in colonies of cells. The agar plates contain a concentration of antibiotics so that only cells expressing the gene of interest and associated gene for drug resistance will survive on the plate. In this way, colonies of cells containing the plasmid and gene of interest are selected for; this is generally termed screening. Colonies of cells can be expanded by growing them in culture media (under drug selection) and the plasmid DNA extracted using established DNA isolation procedures (i.e. mini-prep).

### 3.2.2   *Cloning of Bacterial Iron Processing Genes for MR-based Cell Tracking*

Magnetotactic bacteria (MTB) are a class of bacteria that are capable of orienting along the field lines of the earth's magnetic field. MTB are able to accomplish this by way of organelles called magnetosomes that contain magnetic crystals. Figure 3.8 shows a transmission electron microscope (TEM) image of *Magnetospirillum magneticum* strain AMB-1. In the image it is possible to make out the ordered arrangement of magnetic crystals stored within magnetosomes. Evolutionarily, the ability of MTB to orient along the earth's magnetic field is believed to aid these bacteria in migrating along oxygen gradients (60). MTB are classified according to the type of magnetic crystals that they produce which are magnetite, greigite ($Fe_3S_4$), or both. MTB that produce magnetite are

particularly responsive to magnetic fields given the considerably higher magnetic moment of magnetite compared to greigite.
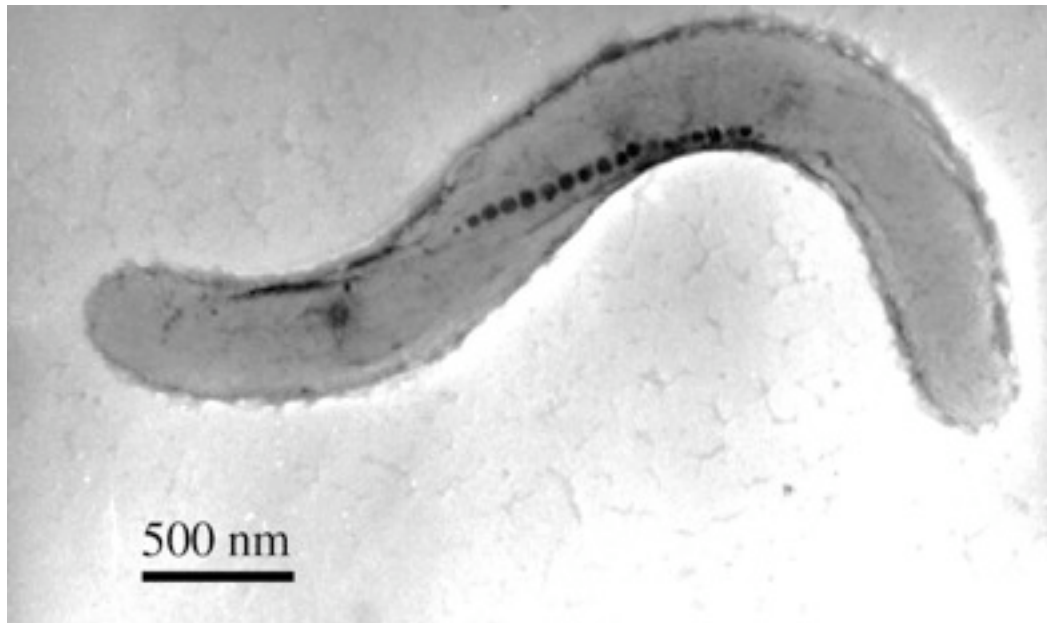


**Figure 3.8—TEM image of MTB strain AMB-1. The ordered arrangement of magnetite crystals stored within magnetosomes is clearly visible. (Image obtained from Arakaki *et al.* (61))**

Magnetosomes are responsible for the bio-mineralization of magnetite and maintaining the appropriate iron concentration within the bacterial cell. Research has focused on identifying the genes responsible for magnetosome formation and control of iron within the cell. These studies have demonstrated an intricate network of genes that play a role in the ability of MTB to produce and maintain magnetite within the cell. For example, Arakaki *et al*. have identified several genes in the AMB-1 bacterial strain that bind iron ions and may be directly involved in the process of magnetite crystal formation (62). Another study identified a 98-kilobase (kb) genomic sequence among other regions related to magnetosome regulation (63). In addition, Suzuki *et al*. showed an up-regulation of 464 genes and a concomitant down-regulation of 263 genes in the AMB-1 strain in response to iron rich conditions (64). Further work by Nakamura *et al*. identified

magA as a gene involved in the production of magnetosomes in *Magnetospirillum magneticum* (65,66). To further support these results, genomic analysis results identified deletions in the magA gene within non-magnetic mutant bacterial samples (67).

Given the research focused on identifying the genes responsible for magnetite production, processing, and storing in MTB, there has also been work using these genes for MR-based cell tracking. The paradigm involves expressing these bacterial genes in mammalian cells in order to promote the bio-mineralization of magnetite through the formation of magnetosomes. For example, Zurkiya *et al*. have reported the ability to stably express the magA gene within human embryonic kidney (HEK) 293 cells, and use it as a MR reporter (68). In particular, the gene was cloned into an inducible vector, which enables the ability to control expression of the gene. Expression of magA within 293 cells resulted in the production of magnetic iron oxide particles and shortened MR transverse relaxation. Lastly, using this system they have reported the ability to promote uptake of endogenous iron *in vivo* and visualize cells expressing magA using MRI. In another study, Goldhawk *et al*. demonstrated the ability to express the magA gene within mouse neuroblastoma N2A cells (69). Expression of the gene resulted in detection via 11T MRI, and a single point mutation in the magA sequence limited the ability to detect mutant cells on MR images.

*3.2.3   Cloning of Mammalian Iron Processing Genes for MR-based Cell Tracking*

Mammalian cells have native genes that are responsible for iron uptake, storage, and processing. Similar to the expression of bacterial genes responsible for iron processing genes, research efforts have also focused on over-expression of the corresponding mammalian cell genes in order to promote increased uptake of iron and subsequent

cellular tracking using MRI. As is the case with magnetosomes in MTB, there are a variety of genes implicated in mammalian cells that are likely involved in cellular iron processing. In the case of MR-based cell tracking, two genes that have been examined extensively are ferritin and transferrin.

Ferritin is a ubiquitous intracellular protein that stores iron within the cell and releases it in a controlled fashion. As a globular protein it consists of 24 subunits, and maintains iron in a soluble non-toxic form. The subunits that make up ferritin consist of polypeptides designated as either heavy chain (FTH) or light chain (FTL). Figure 3.9 shows an example of the structure of FTL.
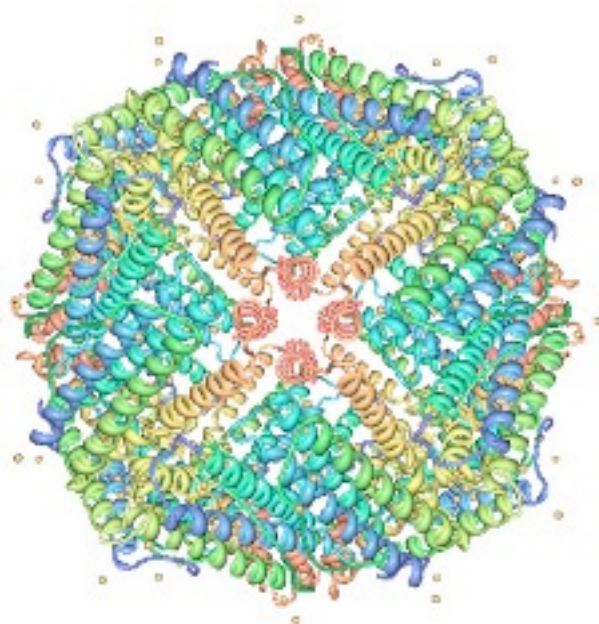


**Figure 3.9—Structural representation of ferritin (FTL) showing the globular orientation. This hollow structure allows variable uptake of iron, which is stored within the center of the structure. (Image obtained from http://faroucheombre.wordpress.com/page/2/)**

Recent studies have examined the ability to detect cells over-expressing ferritin using MRI. For example Naumova *et al*. demonstrated the ability to stably over-express FTH in mouse skeletal myoblast (C2C12) cells (70). Cells expressing the gene could be detected

*in vitro* as well as *in vivo* within a mouse infarcted heart model three weeks after transplantation. Focusing on stem cells, Liu *et al.* developed a transgenic mouse ESC line expressing FTH and were able to monitor cellular grafts *in vivo* using $T_2$-weighted MRI (71).

Another protein of interest for MRI-based cell tracking is transferrin. This protein is encoded for by the TF gene, and is responsible for controlling the level of free iron in biological fluids. Transferrin is capable of binding iron and facilitates its transfer into the cell through receptor-mediated endocytosis using its associated transferrin receptor. Figure 3.10 shows a rendering of the structural organization of transferrin, which contains two high affinity iron-binding sites. Working together with the transferrin receptor, transferrin maintains tight control of iron concentration within the cell.



**Figure 3.10—Structural representation of transferrin showing the open configuration necessary for iron binding. (Image obtained from http://en.wikipedia.org/wiki/File:Protein_TF_PDB_1a8e)**

Based on the role that transferrin plays in maintaining proper iron concentrations within the cell, it has also been investigated for MRI-based cell tracking. For example, studies by Deans *et al.* demonstrated the ability to stably co-express transgenic human transferrin

receptor and FTH in mouse neural stem cells (72). Cells over-expressing the genes accumulated significantly more iron compared to control cells when cultured in iron rich medium. This led to *in vitro* MRI detection of expressing cells, as well as *in vivo* MRI detection of cells transplanted in a mouse brain model.

# Chapter 4: Background [3]—Principles of MRI

## 4.1    MRI Fundamentals

MRI is an imaging modality that was developed in the 1970s, and has rapidly gained popularity for use both in the clinic as well as in a research setting. This imaging modality is based on nuclear magnetic resonance (NMR), which can be used to obtain information about the physical, chemical, electronic, or structural nature of a molecule or compound. NMR was independently discovered by Bloch *et al.* (73) and Purcell *et al.* (74) in 1946. Approximately 30 years later in 1973, Lauterbur *et al.* (75) acquired the first MR image through the use of gradients for spatial localization. This development was key in being able to harness the phenomenon of NMR for imaging applications. Of particular note, Purcell and Bloch were jointly awarded the Nobel Prize in Physics in 1952 for their work related to NMR. Similarly, for his work related to MRI Lauterbur was awarded the Nobel Prize in Medicine in 2003, along with Sir Peter Mansfield who formalized the mathematical analysis necessary to convert an MR signal into a viewable image.

NMR and MR imaging fundamentally depend on the interaction between an atom with a non-zero magnetic moment ($\mu$) and an externally applied magnetic field.  A variety of atoms can be imaged using MRI including phosphorus ($^{31}P$) and sodium ($^{23}Na$), but due to its overall abundance within biological tissues and strong magnetic moment hydrogen ($^{1}H$) with its superior inherent sensitivity is the most common element imaged using MRI.

When a magnetic moment is placed within an external magnetic field (**B**), its associated potential energy is defined by:

$$E = -\mu \cdot B \qquad [4.1]$$

When a group of nuclei with magnetic moments are placed in a magnetic field (Figure 4.1), each can align parallel to the field (low energy state) or anti-parallel to the field (high energy state). Based on its lower energy state there is a slightly higher proportion of nuclei aligned with the field than against it. The ratio of the two populations of nuclei is governed by the Boltzmann distribution:

$$N_{higher}/N_{lower} = e^{-\Delta E/kT} \qquad [4.2]$$

In Equation 4.2 $N_{higher}$ and $N_{lower}$ represent the proportion of hydrogen nuclei in the higher and lower energy states respectively, k is Boltzmann's constant ($1.3805 \times 10^{-23}$ J/K), and T is the absolute temperature. The difference in nuclei populations described by Equation 4.2 governs the fundamental principles of MRI and is proportional to the MR signal used to form an image.
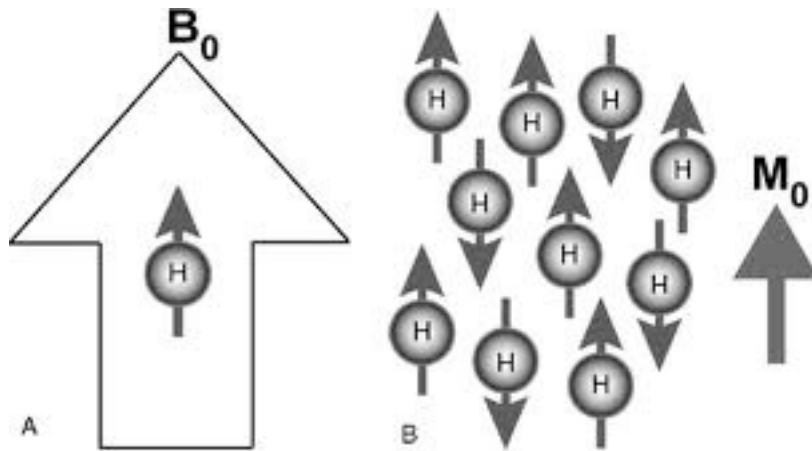


**Figure 4.1—Interaction of hydrogen atoms within an externally applied magnetic field ($B_0$). Atoms align parallel or anti-parallel with the applied field with a slight excess of atoms in the former orientation based on its lower energy state. (Image obtained from http://www.msd.com.mx/msdmexico/)**

When a proton is placed within an externally applied magnetic field with magnitude $B_0$, it experiences a torque and begins to precess with an angular frequency (Figure 4.2). The precession occurs around the axis of the externally applied magnetic field (z). The

frequency of precession $\omega_0$ is denoted as the Larmor Frequency and is governed by the Larmor Equation:

$$\omega_0 = \gamma B_0 \qquad\qquad [4.3]$$

In Equation 4.3 $\gamma$ is the gyromagnetic ratio, and it is clear that the frequency of precession increases linearly with applied field strength. For hydrogen $\gamma$ is 42.575 MHz/T. As such, at clinical field strengths such as 1.5T and 3T, the frequency of precession for hydrogen is ~ 64 MHz and 128 MHz respectively.
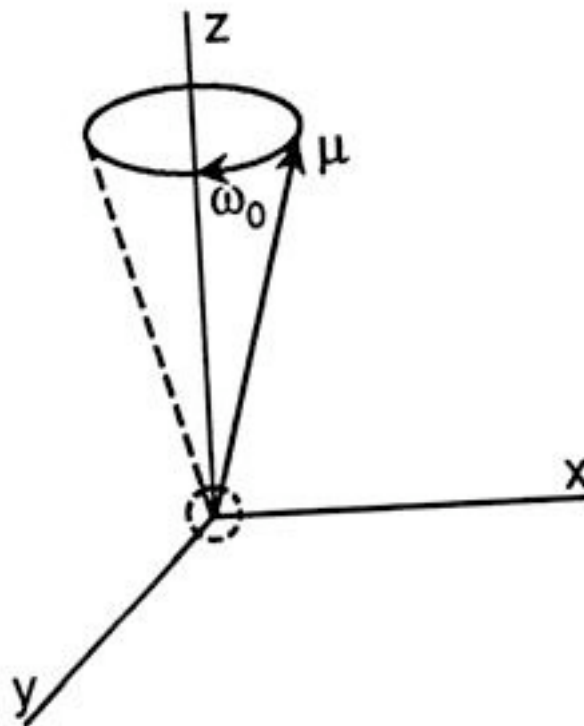


**Figure 4.2—Precession of a proton around the axis (z) of the externally applied magnetic field at the characteristic Larmor Frequency $\omega_0$. (Image obtained from http://www.medcyclopaedia.com/library/radiology/chapter04/4_5.aspx)**

In order to conduct an MR experiment it is necessary to tip magnetization away from the z-axis. This is accomplished by way of a radiofrequency (RF) pulse, which is used to excite the nuclei. This excitation process transitions the nuclei from equilibrium to a

higher energy state. The RF pulse is tuned to match the Larmor Frequency of the precessing nuclei, and is called excitation on resonance. This excitation process causes net magnetization to tilt from the longitudinal (z) axis to the transverse (xy) plane (Figure 4.3).
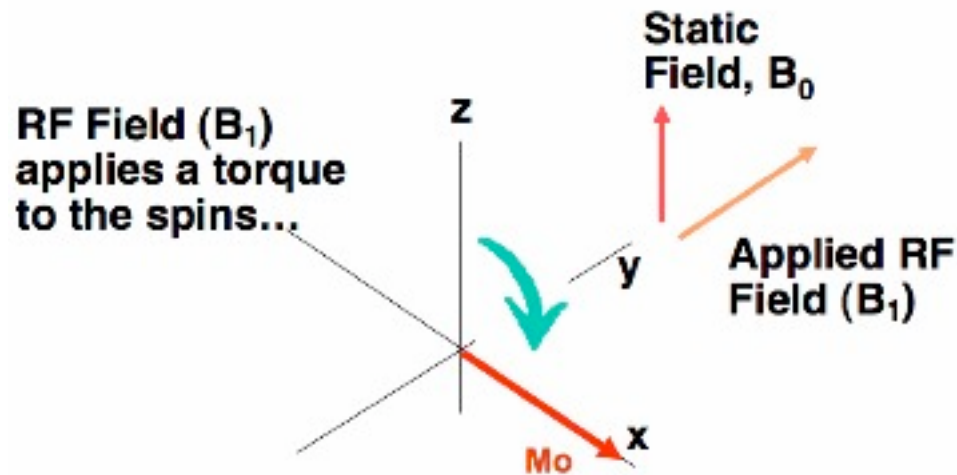


**Figure 4.3—RF pulse excites nuclei from equilibrium to a high-energy state and tips net magnetization ($M_0$) from the longitudinal (z) axis to the transverse (xy) plane. (Image obtained from http://toolsandtutorials.pbworks.com/w/page/26272088/MRI-Physics)**

After excitation of the nuclei, their return to equilibrium results in the emission of a free induction decay (FID) signal that can be measured by a receiver coil. The receiver coil is tuned to the Larmor Frequency of the nuclei in order to detect the signal resulting from the moving magnetic field.

Since the receiver coil detects a FID signal corresponding to the precession of all nuclear spins in the field it is not possible to determine spatial information directly from the signal. Spatial localization, which is necessary in forming an image is accomplished through the use of linear gradient magnetic fields in the x, y, and z direction. Linear gradients encode a slight variation in the experienced magnetic field as a function of

spatial position. For example a gradient along the x direction would result in an applied field in the z direction of the following form:

$$B_z = B_0 + G_x x \qquad [4.4]$$

In Equation 4.4, $B_z$ is the field experienced along the z-axis and $G_x$ is the applied gradient. Based on Equation 4.4 nuclei at different locations along the x-axis will experience slightly different applied fields, and subsequently will precess at a slightly different Larmor Frequency. By applying similar gradients along the y-axis and z-axis it is possible to extract spatial information from the received FID signal.

## 4.2    MR Relaxation Processes

Following RF pulse excitation of the nuclear spins the net magnetization vector relaxes to its original equilibrium state. Two independent processes govern this relaxation process: spin-lattice or $T_1$ relaxation, which is the recovery of magnetization along the longitudinal (z) axis, and spin-spin or $T_2$ relaxation, which is decay of magnetization in the transverse (xy) plane.

### 4.2.1    Longitudinal ($T_1$) Relaxation

$T_1$ relaxation results from the process of energy exchange between the excited nuclei and the surrounding lattice. During this process, the net magnetization vector returns to its original equilibrium state along the z-axis. Longitudinal relaxation behaves according to the following Bloch equation:

$$dM_z / dt = - (M_z - M_0) / T_1 \qquad [4.5]$$

In Equation 4.5 $M_z$ is the longitudinal magnetization, $M_0$ is the magnetization after excitation, t is time, and $T_1$ is the relaxation time constant.   For a 90° excitation, all

magnetization will be initially tipped into the transverse plane.  In this case the solution to

Equation 4.5 is:

$$M_z = M_0(1-exp(-t/T_1)) \qquad [4.6]$$

From Equation 4.6 the $T_1$ relaxation time constant is defined as the time it takes the

longitudinal magnetization to return to 63% of its final equilibrium value. Of particular

note, $T_1$ varies for different biological tissues and increases linearly with field strength.

A variation on $T_1$ relaxation is $T_{1\rho}$ relaxation, which describes spin-lattice relaxation

in the rotating frame (76). This parameter can be used to probe the slow motion

interactions between water and large molecules that have restricted motion and is

governed by the following equation:

$$M_t = M_0exp(-t/ T_{1\rho}) \qquad [4.7]$$

In Equation 4.7 $M_t$ is the detected magnetization, t is time, and $T_{1\rho}$ is the corresponding

relaxation time constant for longitudinal recovery.


## 4.2.2 *Transverse ($T_2$) Relaxation*

Transverse relaxation refers to the decay of magnetization in the xy-plane. This

relaxation happens as a result of fluctuations in the local magnetic field resulting from

microscopic interaction of the magnetic dipoles. These fluctuations cause slight

differences in the experienced field for different spins, a consequent broadening of

resonant frequencies, and ultimately a loss of phase coherence. This process is governed

by the following equation:

$$dM_{xy} / dt = - M_{xy} / T_2 \qquad [4.8]$$

In Equation 4.8 $M_{xy}$ is transverse magnetization, t is time, and $T_2$ is the relaxation time constant. For a 90° excitation, all magnetization will be initially tipped into the transverse plane. In this case the solution to Equation 4.8 is:

$$M_{xy} = M_0\exp(-t/T_2) \tag{4.9}$$

In Equation 4.9 $M_0$ is the initial magnetization in the transverse plane. The $T_2$ time constant is defined as the amount of time that it takes for the signal to decay to 37% of its initial maximum value. Of particular note, $T_2$ varies for different biological tissues and is largely independent of field strength.

In practice, transverse relaxation in the xy-plane is not dependent solely on intrinsic $T_2$ relaxation based on the microscopic interaction of dipoles, but rather is also affected by macroscopic field variations as well. Examples of these variations include inhomogeneities in the uniformity of the main field, sample-induced variations due to differences in bulk susceptibility ($\chi$), and finally variations brought about by the use of contrasts agents (e.g. iron oxide-based agents). The effect of these extrinsic variations on the overall transverse plane magnetization is described by the following:

$$1/T_2{}^* = 1/T_2 + 1/T_2{}' \tag{4.10}$$

In Equation 4.10 $T_2'$ refers to these extrinsic variations which combine with intrinsic $T_2$ decay resulting in an overall transverse relaxation time constant identified as $T_2{}^*$. Figure 4.4 graphically shows the relationship between the various contributions to overall transverse relaxation.

## 4.3 Measuring Transverse Relaxation

Aside from providing anatomical images of the body oriented in any plane, MRI can also be used to determine inherent quantitative information about various tissues

44

throughout the body. This is accomplished by manipulating various MR imaging parameters in order to experimentally determine the relaxation parameters of different tissues and samples. In focusing on transverse relaxation, gradient echo (GRE) sequences can be used to measure $T_2^*$ while spin echo (SE) sequences can be used to determine $T_2$.
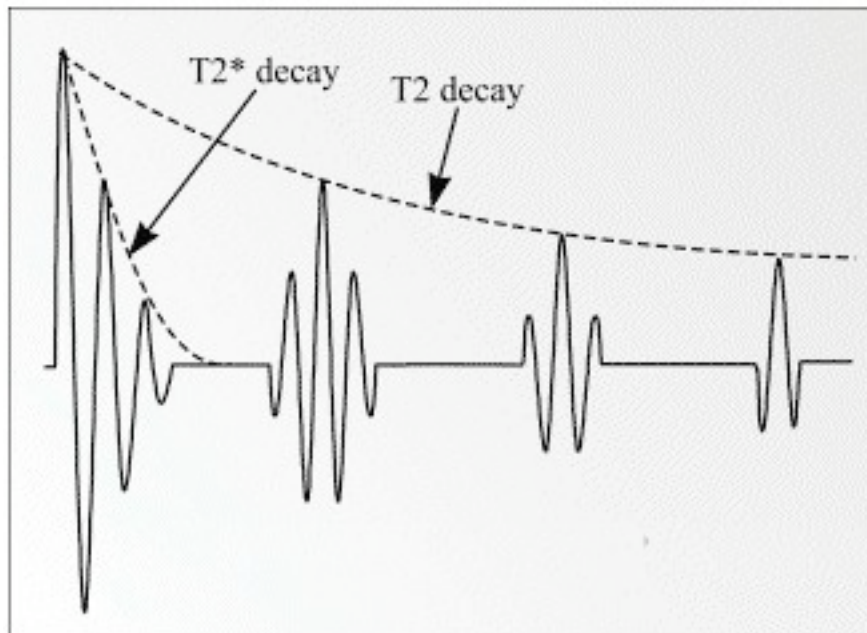


**Figure 4.4—$T_2^*$ which is often determined through the use of a GRE sequence, and $T_2$ decay which can be measured using a SE sequence. (Image obtained from http://www.mikepuddephat.com/Page/1603/)**

### 4.3.1   Measuring $T_2^*$ with GRE Sequences

In order to measure the $T_2^*$ of a sample, an MR imaging experiment is performed using a GRE sequence. Two important parameters that can be used to vary the type of image obtained via MRI are the time to repetition (TR) and the echo time (TE). In forming an image, the sample is repeatedly excited using an RF pulse. Following each excitation, the receiver coil records the FID as the protons in the sample precess and eventually relax back to equilibrium. During each excitation a different part of the image is acquired and combined later to form the final image. During this process of repeated

excitations, the TR is defined as the time in between sequential RF pulses. During this process, the TE commonly refers to the time in between the RF pulse excitation and the point at which the FID signal is recorded by the receiver coil. TR and TE are two main parameters that can be manipulated in MRI to control the contrast of different parts of a sample or tissue within an obtained image.

In order to measure $T_2^*$ of an imaging specimen (e.g. sample, human, etc.) an MRI experiment is performed in which the specimen is repeatedly imaged using a GRE sequence with varied imaging parameters. In particular, the TR is kept constant during each imaging sequence, but the TE is varied each time. Based on Equation 4.9, it is known that transverse relation follows the form of an exponential decay. Therefore, determining the $T_2^*$ consists of experimentally determining the SI at various times, and fitting these experimentally obtained data points to Equation 4.9 (Figure 4.5). In this case the mono-exponential decay equation becomes of the form:

$$S(TE) = S_0 exp(-TE/T_2^*) \hspace{2cm} [4.11]$$

In Equation 4.11 $S_0$ corresponds to the initial SI immediately after RF pulse excitation. Comparing Equations 4.9 and 4.11 it is evident that the SI is quantified at each time point corresponding to a different TE. Given this equation, $T_2^*$ is generally determined by use of an iterative nonlinear least squares (NLLS) fitting method that minimizes the chi-squared statistic between the experimentally obtained values and those predicted by the fitted equation. The $T_2^*$ time constant is defined as the amount of time that it takes for the signal to decay to 37% of its initial maximum value. For an entire MR image this can be done on a pixel-by-pixel basis. This results in a $T_2^*$ map in which the data value associated with each pixel is the experimentally determined relaxation time.
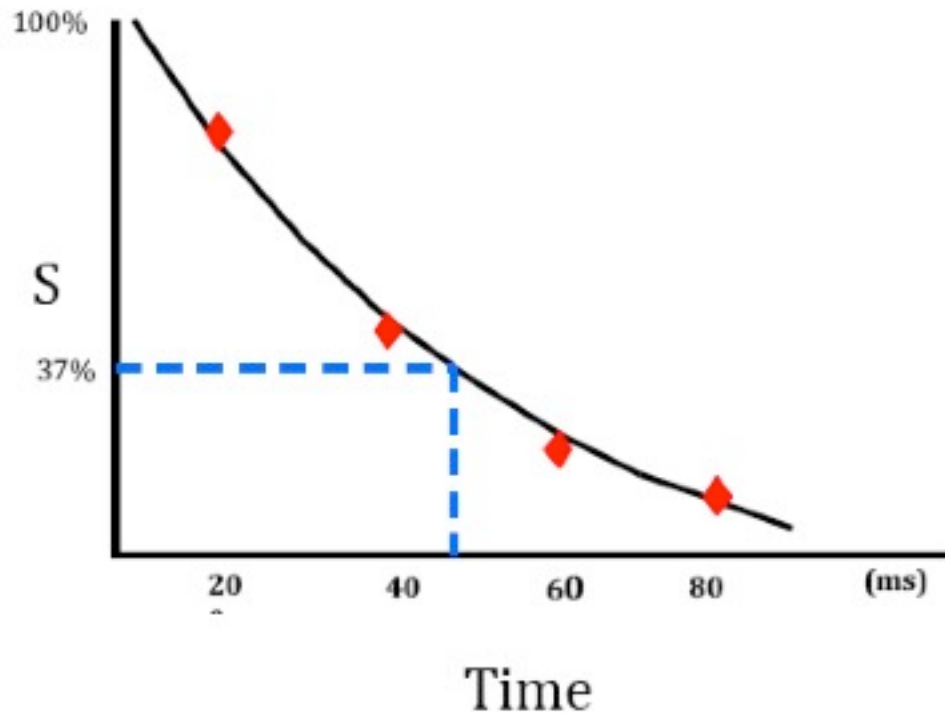
**Figure 4.5—Fitting method for experimentally determining $T_2^*$ and $T_2$. The SI values measured for each TE are fit to the mono-exponential decay equation, and the relaxation time determined as a parameter of the equation. (Image obtained from Dr. Gabrielle Joseph)**

### 4.3.2 Measuring $T_2$ with SE Sequences

The technique for determining $T_2$ is very similar to that used for $T_2^*$. This is to be expected since $T_2^*$ and $T_2$ are closely related as evidenced by Equation 4.10. The primary difference in technique for determining the two relaxation times is the sequence utilized. In order to determine $T_2$ alone resulting from microscopic interactions, without contributions to relaxation from macroscopic field variations, a SE sequence is used. Briefly, the SE sequence consists of a normal 90° RF excitation pulse followed by a 180° refocusing pulse. After the initial excitation pulse the spins will lose phase coherence based on the dominant macroscopic field variations. The purpose of the refocusing pulse is to effectively flip magnetization of the spins within the transverse plane so that they

47

will precess in the opposite direction. This effectively means that the spins will regain

phase coherence. For example, if after the initial 90° RF excitation pulse, the spins begin

to de-phase for a time period of .5t before a 180° refocusing pulse is applied, then at time

t the spins will have regained their phase coherence. This virtually eliminates the

macroscopic field variation-based contributions to relaxation and allows determination of

the inherent $T_2$ of the specimen being imaged.

In order to determine the $T_2$ of an imaging specimen an MRI experiment is performed

in which the specimen is repeatedly imaged using a SE sequence with varied imaging

parameters. In particular, the TR is kept constant during each imaging sequence, but the

TE is varied each time. Based on Equation 4.9, it is known that transverse relation

follows the form of a mono-exponential decay. Therefore, determining the $T_2$ consists of

experimentally determining the SI at various times and fitting these experimentally

obtained data points to Equation 4.9 (Figure 4.5). In this case the mono-exponential

decay equation becomes of the form:

$$S(TE) = S_0 \exp(-TE/T_2) \hspace{2cm} [4.12]$$

In Equation 4.12 $S_0$ corresponds to the initial SI immediately after RF pulse excitation.

Comparing Equations 4.9 and 4.12 it is evident that the SI is quantified at each time point

corresponding to a different TE. Given this equation, $T_2$ is generally determined by use of

an iterative NLLS fitting method that minimizes the chi-squared statistic between the

experimentally obtained values and those predicted by the fitted equation. The $T_2$ time

constant is defined as the amount of time that it takes for the signal to decay to 37% of its

initial maximum value.  For an entire MR image this can be done on a pixel-by-pixel

basis. This results in a $T_2$ map in which the data value associated with each pixel is the

experimentally determined relaxation time. Figure 4.6 shows an example in which a $T_2$ map for knee articular cartilage has been overlaid on top of one of the SE images used to calculate its values.
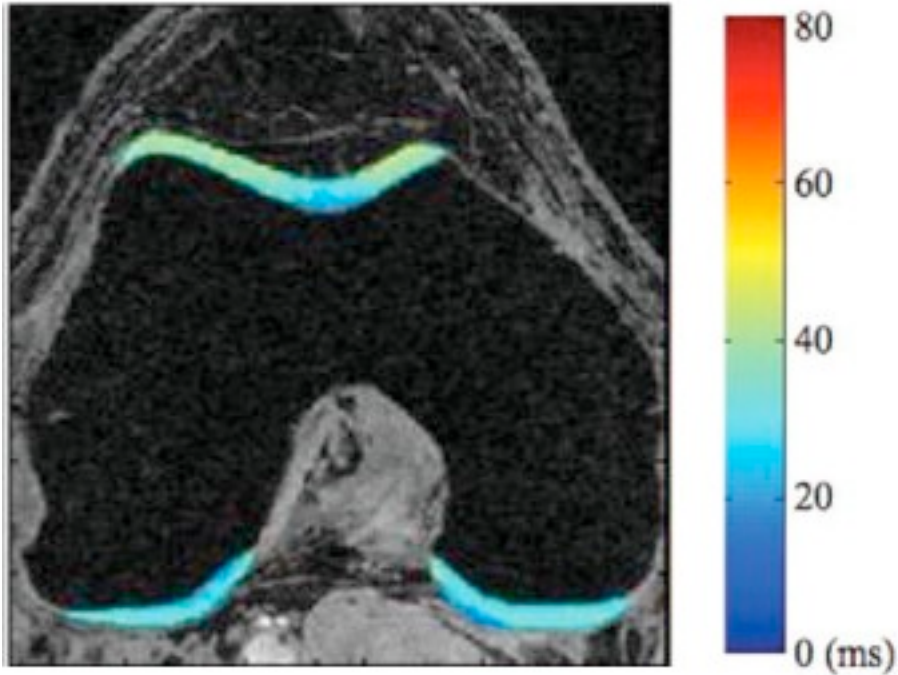


**Figure 4.6—Example $T_2$ map overlaid on an axial knee SE image. The $T_2$ values were calculated by fitting to a mono-exponential decay. As shown in the image, a color map is often associated with relaxation times to allow visualization of the values. (Image obtained from Li *et al.* (77))**

### *4.3.3    Alternative Transverse Relaxation Fitting Techniques*

While fitting the experimentally obtained data to the basic mono-exponential decay equation is the most common technique used to determine transverse relaxation times, depending on the specimen being imaged, other techniques may be more appropriate. These include the use of a multi-exponential fit, or fitting of the data to an exponential decay with an additional noise term.

For some imaging specimens a multi-exponential decay equation may be a better fit for the experimental data. In this case the sample may contain distinct relaxation

components that differ significantly in their values. Although, theoretically the fitting equation can contain any number of exponential decay terms, a bi-exponential decay is most commonly used in this situation (78,79). The underlying assumption in fitting to a bi-exponential decay equation is that the signal consists of a sharp signal drop at short TE, followed by a slower decay at longer TE. In this case the bi-exponential decay equation for $T_2^*$ and $T_2$ fitting is:

$$S(TE) = S_{01}\exp(-TE/T_{21}^*) + S_{02}\exp(-TE/T_{22}^*) \qquad [4.13]$$

$$S(TE) = S_{01}\exp(-TE/T_{21}) + S_{02}\exp(-TE/T_{22}) \qquad [4.14]$$

In Equations 4.13 and 4.14, each term has an associated initial SI value and relaxation value once again defined as the amount of time that it takes for the signal to decay to 37% of its initial maximum value.

In some imaging situations, such as low signal to noise ratio (SNR) images, more accurate values can be achieved by including an additive noise term during fitting (80). This is accomplished by squaring the magnitude image to obtain a power image of the data. Unlike the magnitude image, in a power image the noise present can be considered to be an additive term. This essentially becomes an additional parameter that must be determined during fitting of the experimental data. An alternative approach is to measure the average SI in a region considered to be part of the background (i.e. noise) area, and subtract that from the entire power image. In this case, the exponential fit equation becomes:

$$S^2(TE) = S_0^2\exp(-2TE/T_2) \qquad [4.15]$$

Using Equation 4.15 will yield a $T_2$ value that is half of the true $T_2$ constant. In considering the various fitting techniques it is useful to analyze them in terms of the

number of parameters that must be fit. Fitting a mono-exponential decay equation to the data is a two-parameter fit ($T_2$ and $S_0$). Fitting using the power image with a noise term is effectively a three-parameter fit (noise, $T_2$ and $S_0$). Lastly, fitting the data to a bi-exponential decay is effectively a four-parameter fit ($T_{21}$, $S_{01}$, $T_{22}$, and $S_{02}$). The best fitting technique to use is ultimately dependent on the particular application, and generally minimizes the difference between the calculated and experimentally obtained values (e.g. chi-squared statistic).

## 4.4    <u>**Effect of Iron Labeling on MRI**</u>

The use of iron-based agents for cell labeling results in strong contrast between labeled cells and the surrounding tissue environment. As SPIOs, iron-based agents result in a loss of SI (hypo-intensity) and accordingly are considered to be negative contrast agents. As such, on MR images the labeled cells show up as a dark spot compared to the brighter surrounding tissue. This contrast mechanism is most apparent using GRE ($T_2$*) sequences but is also detectable using SE ($T_2$) sequences.

SPIOs have a high magnetic susceptibility that has the ability to affect the macroscopic homogeneity of the main field when placed within an MRI magnet (36). This magnetic field inhomogeneity results in a rapid loss of phase coherence and corresponding loss of signal detected in the transverse plane (81). This loss of signal manifests as a hypo-intense region compared to the surrounding tissue and can be utilized for effective contrast. A cell labeled with an iron-based contrast agent can be approximated as a magnetically tagged sphere (Figure 4.7) as described by Cunningham *et al*. (82). As expected, this sphere will exert its own magnetic field based on its associated magnetic field lines.
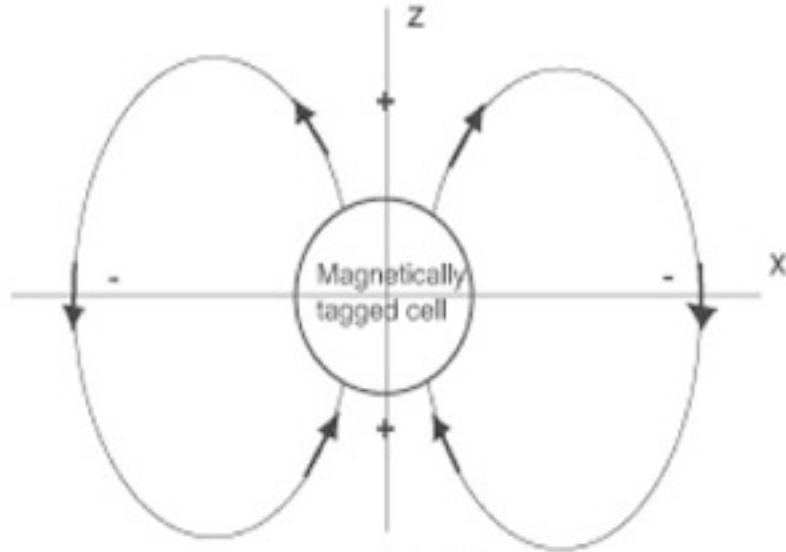
**Figure 4.7—Schematic showing a magnetically tagged cell, which can be approximated as a sphere. The sphere will exert its own magnetic field, which will be enhanced along the z-axis and suppressed along the y-axis. (Image obtained from Cunningham *et al.* (82))**

As shown in Figure 4.7, the magnetic field will be enhanced along the z-axis designated as the poles, and suppressed along the x-axis, designated as the equator. Based on this orientation, the main applied field ($B_0$) is enhanced along the poles, and suppressed along the equator. The field effect of a magnetically tagged sphere can be mathematically approximated by:

$$\Delta B_z(r,\theta) = ((\Delta\chi B_0)/3)(a/r)^3(3\cos^2\theta - 1) \qquad [4.16]$$

In Equation 4.16, $\Delta\chi$ is the difference in magnetic susceptibility between the sphere and surrounding environment, $B_0$ is the main field strength, a is the radius of the sphere, r is the distance from the center of the sphere, and theta is the angle made with the direction of the applied field. There are two important points that can be determined from Equation 4.16. First the enhancement or suppression of the applied field results from the cosine dependence in the equation. This is demonstrated by the simulations of field enhancement and suppression shown in Figure 4.8.
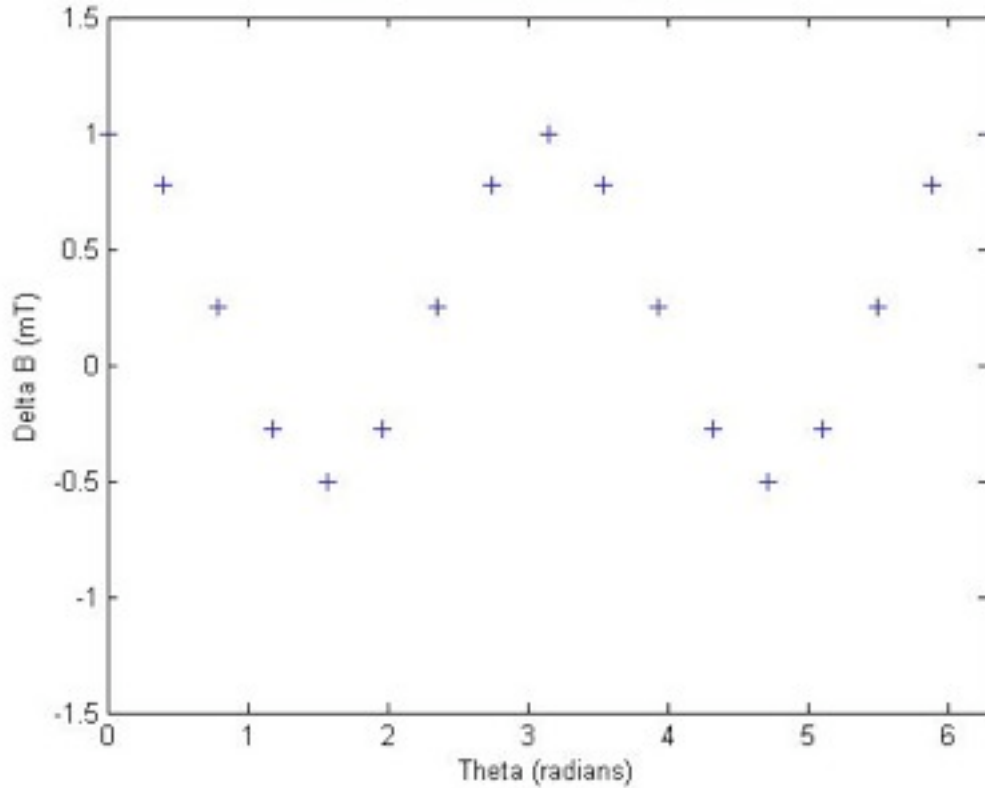
**Figure 4.8—MATLAB plot demonstrating the enhancement (poles) and suppression (equator) of the main field based on Equation 4.16. $\Delta B_z$ shows maximum enhancement at $\theta = 0$, $\pi$, and $2\pi$, and maximum suppression at $\theta = \pi/2$, and $3\pi/2$. ($B_0 = 3T$; $a = 1.63$ $\mu$m; $r = .815$ $\mu$m; $\Delta\chi = 500$ ppm)**

Second, the strength of the suppression or enhancement drops off rapidly based on the cubic dependence of the equation on the distance from the center of the sphere. As an example, Figures 4.9 and 4.10 show a simulation of the drop off in enhancement and suppression of the field for a magnetically tagged sphere of size 1.63 $\mu$m. It is important to note that while the effect for a single particle is relatively small, this effect will be compounded for a cell labeled with multiple iron-based contrast particles, and even more so for a population of labeled cells being imaged using MRI.

While the effect of the field distortion is most easily visualized using a GRE sequence, the loss of SI can also be detected using a SE sequence. SE sequences involve a 180° refocusing pulse in order allow the nuclear spins to regain phase coherence. As

such, this pulse inherently would be expected to negate the effects of the iron-based contrast agent. Essentially, if nuclear spins in the vicinity of an iron-based contrast agent particle were exposed to the same field variation before and after the refocusing pulse, then when the signal is read out the spins would once again be in phase.
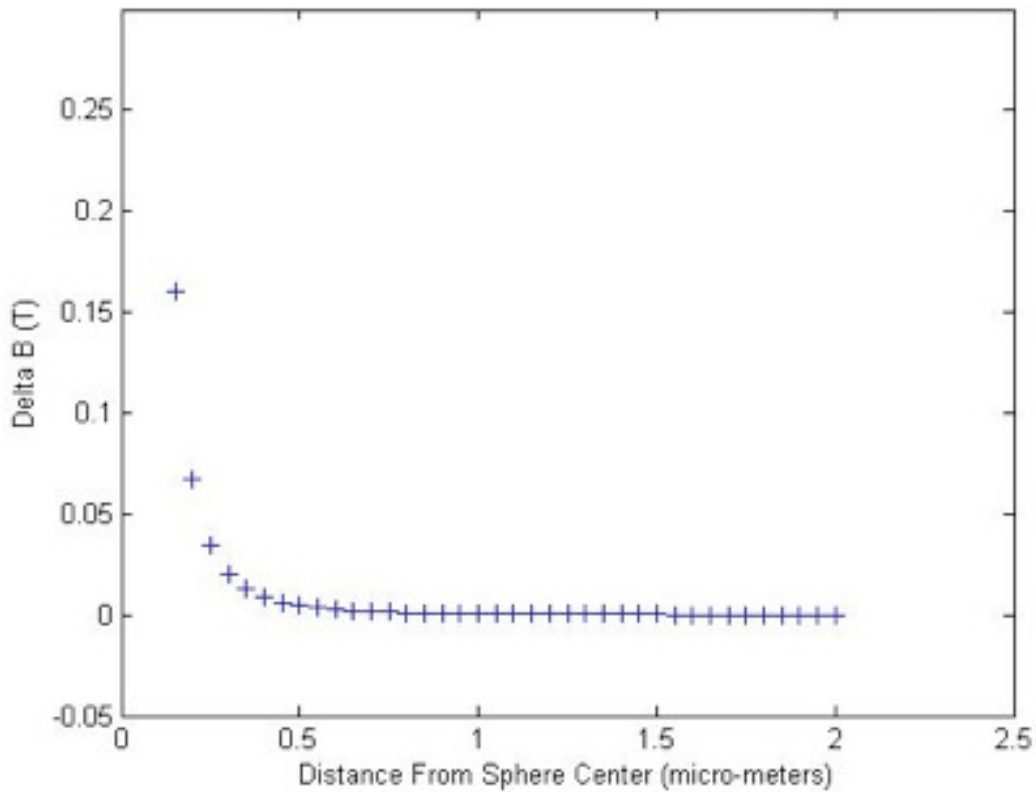


**Figure 4.9—MATLAB plot demonstrating the rapid drop off in field enhancement ($\Delta B_z$) with distance r from the center of the sphere for regions corresponding to the poles. $\Delta B_z$ shows maximum enhancement nearest the center. ($\theta = 0$; $B_0 = 3T$; $a = 1.63\ \mu m$; $\Delta\chi = 500$ ppm)**

However, because of diffusion of protons and the associated spins, the effective field experienced before and after the refocusing pulse may not be the same. Thus during signal readout, the spins have not perfectly rephrased. As such, there is still some residual signal loss, which results in the ability to detect iron-labeled cells using SE sequences in addition to GRE sequences.
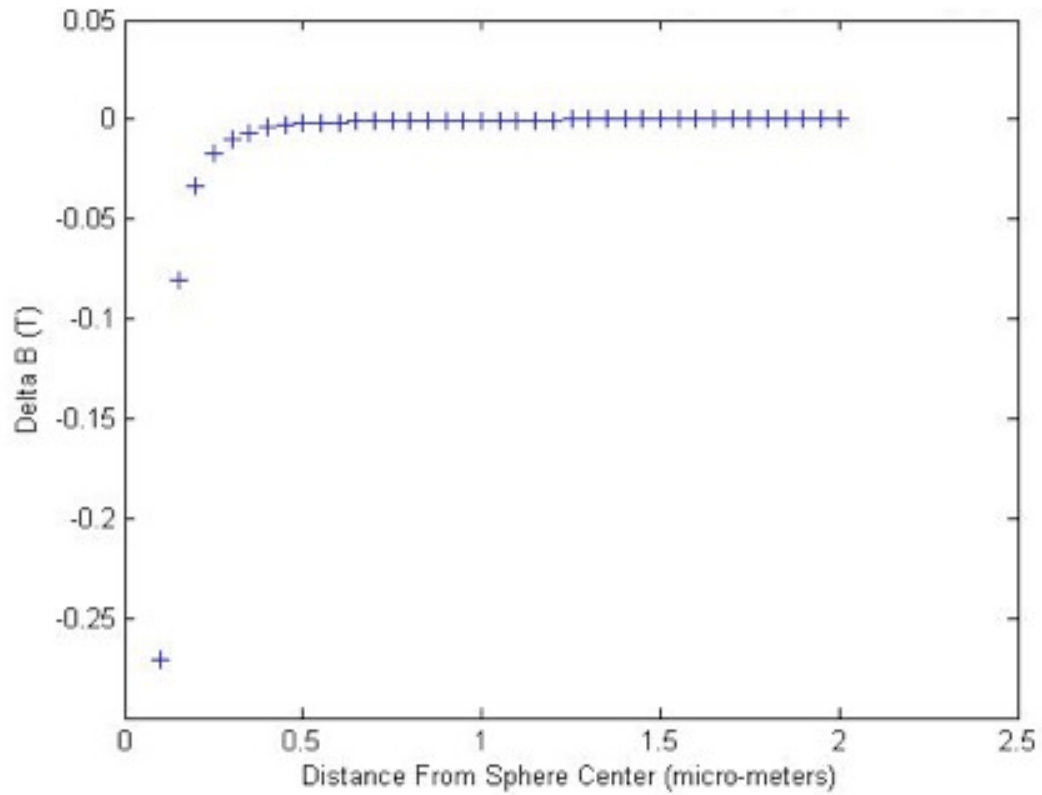
**Figure 4.10—MATLAB plot demonstrating the rapid drop off in field suppression ($\Delta B_z$) with distance r from the center of the sphere for regions corresponding to the equator. $\Delta B_z$ shows maximum suppression nearest the center. ($\theta = \pi/2$; $B_0 = 3T$; a = 1.63 $\mu$m; $\Delta\chi = 500$ ppm)**

# Chapter 5: Research Studies of Cell Labeling with Fe-Pro

## 5.1    Introduction

The purpose of these studies was to investigate and further characterize Fe-Pro labeling of human MSCs (hMSCs), and to explore the potential application of this novel methodology for detection of stem cells implanted into the disc for IVD degeneration repair. Further development of this technique would aid in the development and overall evaluation of stem cell-based therapies for repair and regeneration of this tissue. Also, the ability to reliably and non-invasively monitor stem cells using MRI at multiple time points following implantation would further enable the transition of stem cell-based therapies into a clinical setting for a variety of applications.

These studies investigated *in vitro* labeling of hMSC cultures, MR detection of the associated signal void resulting from labeling, and quantitative characterization of SI loss on MR images (i.e. $T_1$, $T_2$, & $T_2$* relaxation). In addition, the effect of labeling on stem cell viability was also examined. In order to determine whether labeled cells could be detected within 3D scaffolds suitable for implantation, labeled cells were seeded within constructs, and imaged using MRI. Based on the two major types of tissue engineering constructs, synthetic and natural (83), these studies investigated detection of labeled stem cells within each type of matrix. For synthetic polymer investigation, labeled cells were seeded in biocompatible PEG hydrogel plugs and imaged *in vitro* using both MRI and confocal microscopy. As a natural polymer, a fibrin gel was used to load labeled cells and implanted *ex vivo* within a rat model of IVD to demonstrate initial detection of transplanted cells populations via MRI.

## 5.2    Materials and Methods

### 5.2.1    Stem Cells and Culture

Following procedures approved by the Institutional Review Board at the University of California, San Francisco (San Francisco CA, USA), bone marrow tissue was obtained from young adult male patients undergoing surgery for repair of femur fractures. Mononuclear cells were isolated by Percoll (Sigma Aldrich, St. Louis, MO, USA) gradient separation, and then plated in high glucose Dulbecco's Modified Eagle's Medium (DMEM) (Invitrogen, Carlsbad, CA, USA) with 10% fetal bovine serum (FBS; Invitrogen) and 1% penicillin/streptomycin (Invitrogen). After 24 hours, non-adherent cells were washed away. Adherent cells were maintained in the same media, expanded using standard culture condition, (37°C and 5% $CO_2$) and passaged 1:4 at 80-90% confluence. Cells were sub-cultivated using .25% trypsin with 1mM ethylenediamine-tetraacetic acid (EDTA; Invitrogen). Cells used for labeling experiments were between passages 8-10 to avoid potential issues associated with cell senescence.

### 5.2.2    Cell Labeling

The Fe-Pro labeling procedure was performed as described by Arbab *et al.* (54,84). Briefly, the contrast agent Feridex IV (Berlex Laboratories, Wayne, NJ, USA) at a concentration of 100 μg/mL, and the transfection agent protamine sulfate (American Pharmaceutical Partners, Schaumburg, IL, USA) at a concentration of 4 μg/mL were added to DME serum-free media and mixed for approximately 10 minutes. Of note, the stock concentration of Feridex particles is supplied at 11.2 mg/mL. Following mixing, 12.5 mL of the labeling solution was added to an 80% confluent hMSC monolayer in a

150 cm$^2$ cell culture flask. After 2 hours of incubation under standard culture conditions, an equal volume of complete DMEM was added to the cultures for a final iron oxide concentration of 50 µg/mL. Cell cultures were then incubated overnight.

Following labeling with Fe-Pro, samples were washed with phosphate-buffered saline (PBS) containing heparin (Abraxis Bioscience, Los Angeles, CA, USA) at a concentration of 10 United States Pharmacopeia (USP) units/mL. Heparin was used during washing because it competes with the iron oxide particles for binding with protamine sulfate, thus working to dissolve cells surface bound Fe-Pro particles (54) and deactivate extracellular Fe-Pro. Of note, similar to Feridex, heparin is approved by the FDA and is used as an anti-coagulant clinically. Cells were then trypsinized, collected, filtered through a 40 µm mesh (BD Biosciences, Bedford, MA, USA) and counted for further experiments.

### 5.2.3  *Fe-Pro hMSCs in Synthetic Hydrogel Constructs*

To determine if cells labeled with Fe-Pro could be detected *in vitro* when seeded within synthetic 3D constructs, labeled hMSCs were imaged using MRI and confocal microscopy after seeding within PEG hydrogels. The hydrogel precursor solution was formed using 84% volume/volume (v/v) PEG-dimethylacrylate (PEGDMA; MW 750; Sigma), 8% v/v 2,2-Dimethoxy-2-phenylacetophenone (Sigma) photo-initiator in 1-vinyl-2-pyrrolidone (Sigma) cross-linker (60 mg/mL), and 8% v/v PBS. Two milliliters of this solution was placed into a well of a 6-well plate (Corning, Corning, NY, USA) and cells in solution were added to a reach a concentration of $1 \times 10^6$ cells/mL. The plates were then exposed to 365 nm ultraviolet (UV) light (Uvitec, Cambridge, United Kingdom) for 30 s – 5 mins until gelation occurred. Of note, hydrogels seeded with labeled cells took longer

(3-5 mins) to solidify under UV light compared to unlabeled cells and empty hydrogels (30 s – 2 mins).

### 5.2.4    Ex Vivo Detection of Labeled hMSCs Within a Fibrin Gel

In order to determine whether labeled cells could be detected within a natural polymer loaded into an animal model, labeled cells were imaged *ex vivo* within the IVD of excised rat tails. Labeled cells were loaded into a fibrin gel (Tisseel VH Fibrin Sealant, Baxter International Inc., Deerfield, IL, USA) at a concentration of $1x10^7$ cells/mL, according to the manufacturer's instructions. Injection into the IVD was guided by the use of a fluoroscope (Xiscan C-arm Assembly, Xitec, Windsor Locks, CT, USA). A syringe needle was used to push the nucleus pulposus out of the IVD, and 50 µL of the gel containing labeled cells was injected into the region. Based on previous retention studies, approximately 10 µL is retained initially within the disc, yielding an estimate of $1x10^5$ cells present following injection. As a control, an empty fibrin gel was injected into an adjacent disc within the rat tail. X-ray images (Faxitron X-ray, Whelling, IL, USA) were obtained prior to and following the injection, and the difference in disc height measured as an indicator that the gel containing the labeled hMSCs (or empty fibrin gel) was in fact injected into the IVD. All research involving animals was performed under approved guidelines established by the UCSF institutional animal care and use committee.

### 5.2.5    3T MR Imaging

All MR imaging experiments were performed on a 3T scanner (GE Medical Systems, Waukesha, WI, USA) and Mayo wrist coil (Mayo Clinic, Rochester, MN, USA). For *in*

*vitro* imaging of cells in solution, cells at concentrations ranging from $1x10^4$-$1x10^6$ cells/mL were suspended in tubes containing 0.5 mL Ficoll (1.077 g/mL; Amersham Biosciences, Piscataway, NJ, USA). Ficoll was used to suspend the cells in order to maintain osmolarity and prevent cell settling during the imaging procedure. As a negative control, unlabeled hMSCs and an empty Ficoll solution were also imaged. For each concentration of labeled cells, and the unlabeled controls, multiple samples (n=3) were prepared for *in vitro* imaging and the results averaged. For cells labeled and seeded in hydrogels, the cross-linked gels were placed within the imaging tubes without Ficoll. For the hydrogel experiment controls, empty hydrogels were imaged, as well as hydrogels containing unlabeled hMSCs. Tubes were placed in a water bath and imaged at room temperature (20°C). A SE sequence was used to determine $T_1$ (TE/TR = 12/60-1000 ms) and $T_2$ (TE/TR = 12-300/4000 ms) relaxation times. A GRE sequence was used to measure $T_2$* relaxation times using a 90° flip angle and TE/TR = 4-24/34 ms. In addition, in order to determine the effect of flip angle on SI loss using GRE imaging, Feridex particles were diluted (1:10-1:1000) in PBS and imaged at varying flip angles (10-90°) with a TE/TR = 4-24/34 ms. The field of view (FOV) used was 60 x 60 mm, and the in-plane resolution of the single coronal slice was 234 μm on a side with a thickness of 9 mm. Dedicated processing software written in Interactive Data Language (IDL; Research Systems, Boulder, CO, USA) and MATLAB (Mathworks, Natick, MA, USA) was used to quantify $T_2$* relaxation times by performing a two-parameter (initial SI and $T_2$* relaxation time) exponential fit of the experimentally obtained data points. This was done for each of the samples (n=3), and the results averaged. In cases where Fe-Pro labeling led to saturation of SI loss into the background noise, two different methods were used

60

for fitting. In the first method, only the linear region on natural log plots of SI was used for curve fitting. In the second method, the images were converted to power images by squaring the magnitude images. These power images were then used for a three-parameter fit, in which the initial SI, the $T_2$* relaxation time, and an additive noise term were optimized.

For *ex vivo* natural polymer detection of labeled cells within the excised rat tails, specimens were scanned in the coronal orientation using a 3D multi-slice GRE sequence (TE/TR = 8/24 ms). The in-plane resolution of the obtained images was 117 μm on a side, with a slice thickness of 0.6 mm and a total imaging thickness of 14 mm. The FOV for the region imaged was 60 mm.

### 5.2.6   Confocal Microscopy

Labeled hMSCs seeded within PEG-based hydrogels were also imaged using confocal microscopy. Following Fe-Pro labeling, hMSCs were also labeled using CellTracker CMFDA (Invitrogen) according to the manufacturer's directions. These cells were then seeded within PEG-based hydrogels and placed in 6-well plates. A stack of images was obtained throughout the entire volume of the hydrogel using a Nikon C1SI imaging system (Nikon USA, Melville, NY, USA) with a 488 nm excitation wavelength and a 30 nm pass-band centered at 515 nm (green). The imaging setup consisted of a water immersion lens with a 10x objective and a 0.3 numerical aperture (NA). The FOV for each slice in the stack was 615 μm on a side with a slice thickness of 5 μm and a total thickness of 205 μm. The stack of images was processed and combined into a 3D volume using Nikon image processing software (NIS Elements AR 2.30).

*5.2.7   Cell Viability*

To assess viability of cells following labeling, cells labeled with Fe-Pro and control hMSCs were plated at 70% confluence in 2-well Permanox chamber slides (Nalge Nunc International, Rochester, NY, USA). At days, 0, 1, 2, 4, and 8 after labeling, hMSC viability was assessed with the Live/Dead Reduced Biohazard Viability/Cytotoxicity Kit (Invitrogen). Viability of unlabeled cells was also assessed as a control. Cells were incubated in a solution containing 2 μL SYTO 10 green fluorescent nucleic acid stain, and 2 μL ethidium homodimer-2 in 1 mL of (4-(2-hydroxyethyl)-1-piperazineethanesulfonic acid) buffered saline solution at room temperature in the dark for 30 minutes. Cells were then viewed with a fluorescent microscope and digital micrographs were obtained using both a Fluorescein (excitation/emission = 494/517 nm) and Texas Red filter (excitation/emission = 528/617 nm). Images were loaded into Adobe Photoshop (Adobe Systems, San Jose, CA, USA), and using an overlaid grid live and dead cells were quantified through hand counts performed by lab personnel. The ratio of dead cells to live cells was recorded and used for statistical analysis.

*5.2.8   Statistical Analysis*

Statistical analysis of the obtained relaxation times was performed using an analysis of variance (ANOVA) test, followed by a Holm t-test to compare each of the labeled samples against the unlabeled control. For cell viability data, an ANOVA test on the ratio of dead cells to live cells for the 5 experimental groups and single control group was used.

## 5.3   <u>Experimental Results</u>

*5.3.1 Effect of Labeling with Fe-Pro on Signal Characteristics*

The results of the *in vitro* experiments indicate efficient cellular uptake of the contrast agent via Fe-Pro complex formation, and corresponding distinguishable SI loss of labeled cells on MR images (Figure 5.1). Labeled cells (Figure 5.1a) show up considerably darker than unlabeled cells (Figure 5.1b). Digital micrographs showing labeled cells before heparin wash (Figure 5.1c), labeled cells after wash with PBS (Figure 5.1d), and unlabeled cells (Figure 5.1e) are also depicted.
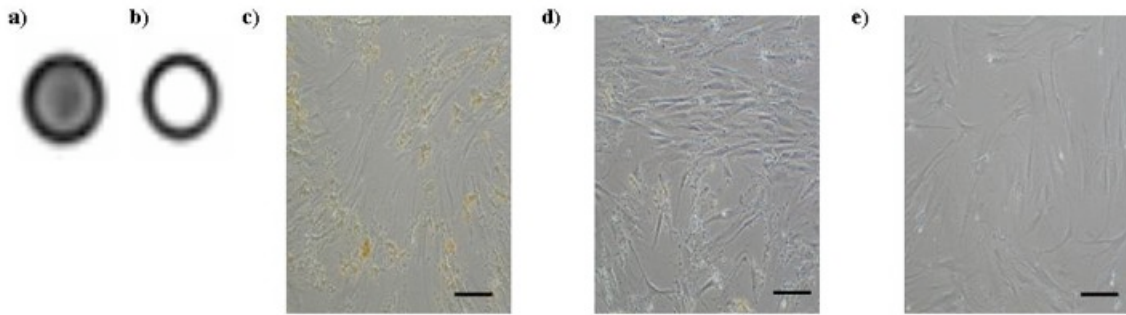


**Figure 5.1—Iron oxide labeling of hMSCs. *In vitro* GRE (TE/TR = 4/34 ms) MR image of (a) iron oxide-labeled cells ($1 \times 10^6$ cells/mL); (b) unlabeled cells ($1 \times 10^6$ cells/mL); (c) optical micrograph of labeled cells before heparin wash; (d) optical micrograph of labeled cells after heparin wash; (e) optical micrograph of unlabeled cells. (Scale bar = 40 $\mu$m)**

Plots of SI versus TR ($T_1$ measurements) and SI versus TE ($T_2$, and $T_2$* measurements) are depicted in Figure 5.2. On $T_1$-weighted images (Figure 5.2a), Fe-Pro labeling does not appear to have an effect on SI, and labeled cells are not distinguishable from unlabeled cells. The effect of Fe-Pro labeling is most pronounced on $T_2$*-weighted GRE images (Figure 5.2b). Cells labeled at the highest concentration of $1 \times 10^6$ cells/mL shows the greatest loss in SI, while labeled cells at a concentration of $1 \times 10^4$-$10^5$ cells/mL also have lower SI values at low TEs compared to unlabeled hMSCs. On $T_2$-weighted images, (Figure 5.2c), labeled cells appear to be distinguishable from unlabeled cells at longer TEs (70-300 ms), but SI loss does not appear to vary with cell concentration.
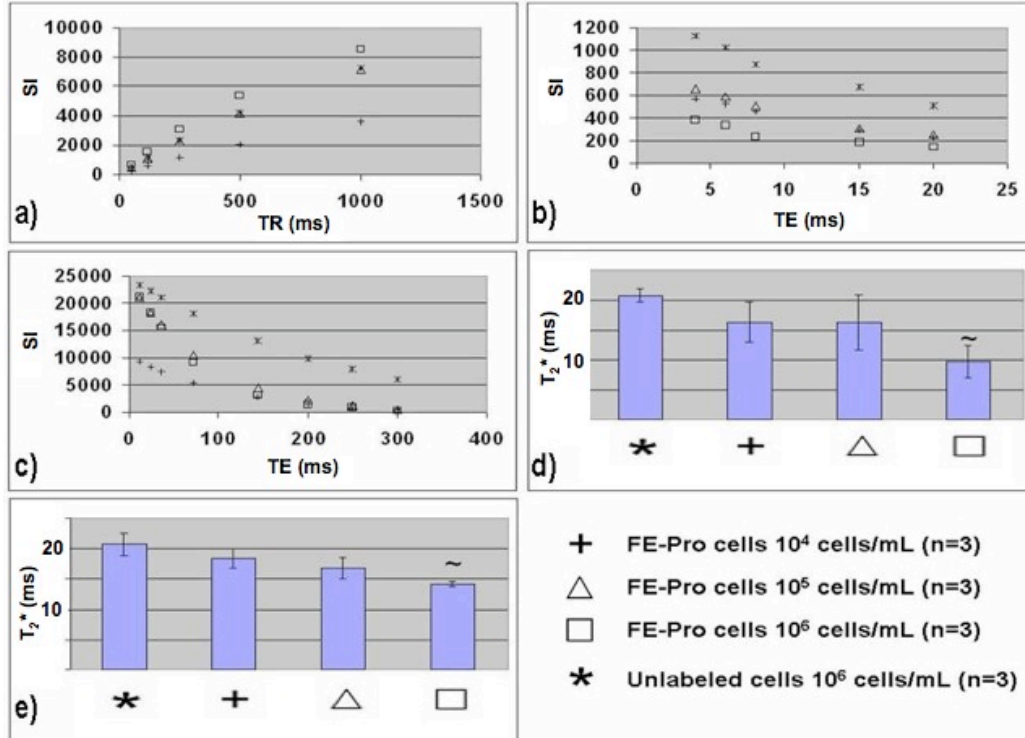
**Figure 5.2—SI and relaxation measurements. (a) SI vs. TR plot resulting from SE sequence. Labeled cells are indistinguishable; (b) SI vs. TE plot resulting from GRE sequence. SI values are lower for labeled cells; (c) SI vs. TE plot resulting from SE sequence. Labeled cells are distinguishable from unlabeled cells at TEs above 70 ms; (d) $T_2^*$ relaxation times for labeled and unlabeled cells obtained by fitting SI values to an exponential curve. For Fe-Pro cells at $1 \times 10^6$ cells/mL only TEs of 4, 6, and 8 ms were used for fitting to account for signal loss saturation; (e) $T_2^*$ relaxation times obtained by including a noise term in the exponential fit. (n = # of samples for each concentration; ~ = statistical significance $p < 0.01$ compared to unlabeled cells)**

Focusing on the $T_2^*$-weighted GRE images where SI loss is strongest, $T_2^*$ relaxation times obtained by using a two-parameter fit are depicted in Figure 5.2d. Compared to the unlabeled control, there is a statistically significant difference ($p < 0.01$) in the $T_2^*$ values for the labeled cells at $1 \times 10^6$ cells/mL. Figure 5.2e shows the $T_2^*$ results of the three-parameter fit. Including noise in the fit yields a higher $T_2^*$ value for $1 \times 10^6$ cells/mL as compared to the two-parameter fit, but the difference between relaxation times for labeled and unlabeled cells at the highest concentration is still statistically significant ($p < 0.01$).

Seeding of labeled stem cells within PEG-based hydrogels results in *in vitro* detection

via MRI (Figures 5.3a-c). Labeled cells within the hydrogel appear as a hypo-intense

region on the obtained images.
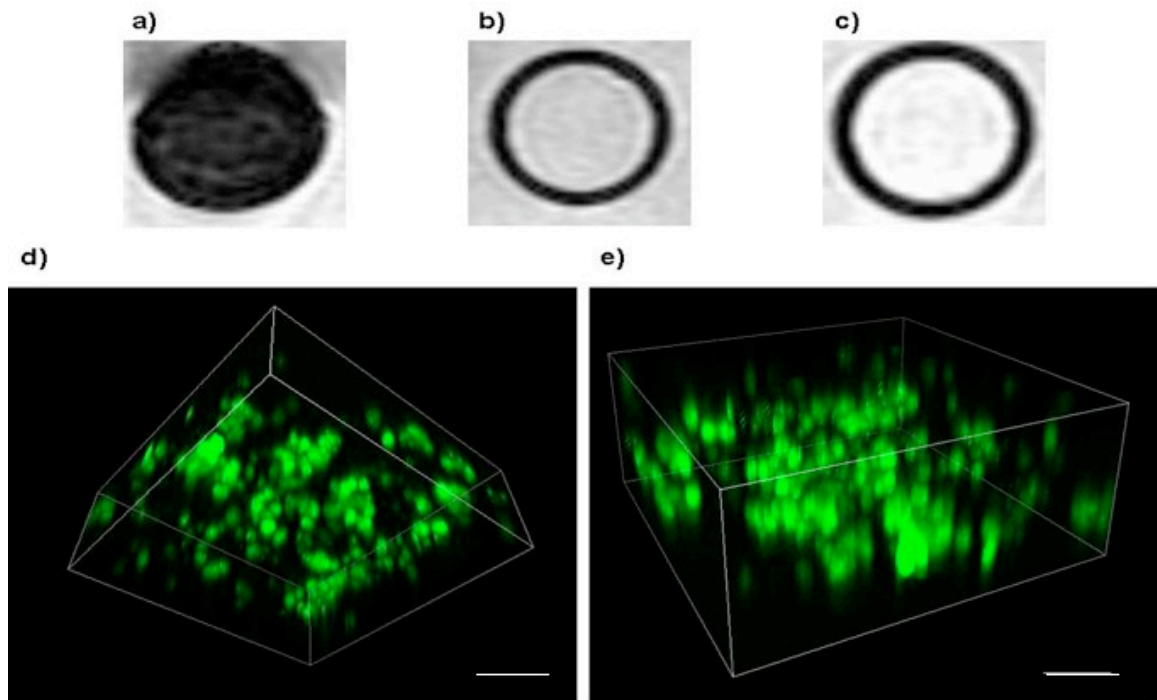


**Figure 5.3—MRI and confocal microscopy of labeled cells. *In vitro* GRE (TE/TR = 6/34 ms) MRI of (a) stem cells labeled with the iron oxide complex seeded within the hydrogel ($1x10^6$ cells); (b) unlabeled stem cells seeded within the hydrogel ($1x10^6$ cells); (c) hydrogel without cells. Labeled cells show up as a hypo-intense region compared to unlabeled cells and the empty hydrogel; (d) & (e) confocal microscopy volume rendered images of labeled stem cells. Positive green staining indicates the position of live cells following labeling and hydrogel polymerization. (Scale bar = 100 μm)**

Imaging of cells using confocal microscopy allowed detection of single cells throughout

the volume of the hydrogel. Representative confocal microscopy volume images are

shown in Figure 5.3d-e. Cells were stained using the CellTracker CMFDA kit, which

stains only live cells. The positive stain indicates that the Fe-Pro hMSCs survived the

labeling procedure and the hydrogel photo-polymerization process.

*5.3.3  Ex Vivo MR Detection of Labeled Cells*

In the rat model (Figure 5.4) the signal loss due to labeling with Fe-Pro is clearly apparent in the injected discs. While the labeled cells in the disc appear black in the image, the disc injected with only fibrin gel is brighter. A radiograph image depicting the sites of injection is also shown.
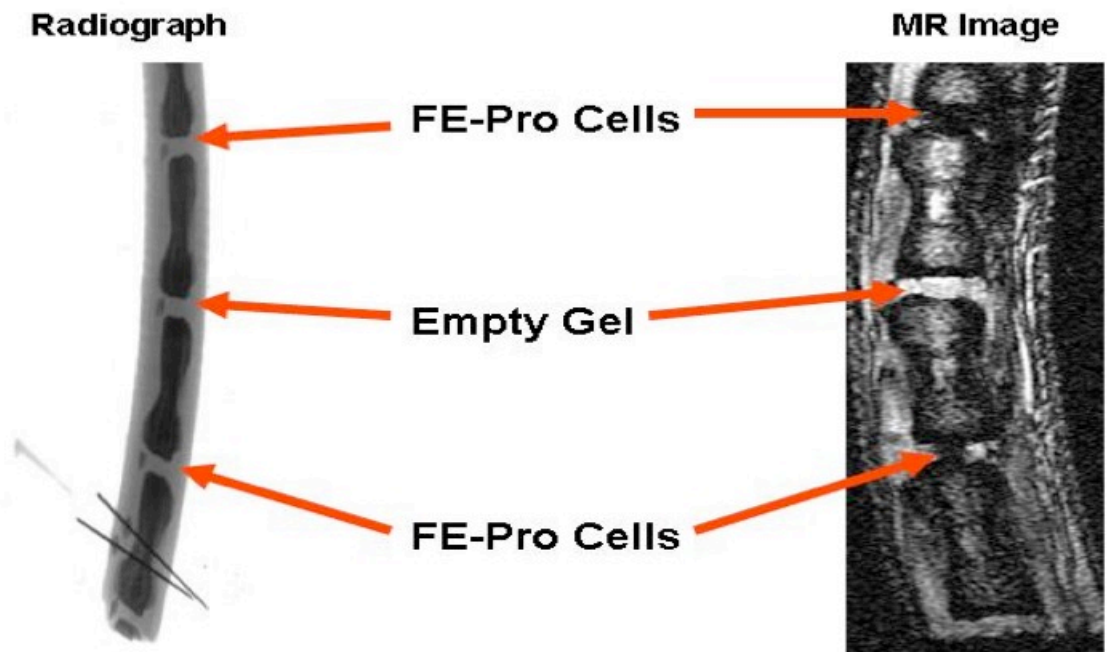


**Figure 5.4—*Ex vivo* detection of iron oxide-labeled cells within a rat model of disc degeneration. Rat discs were injected with a fibrin gel containing labeled cells (1x10$^7$ cells/mL) and imaged using MRI. Discs injected with labeled cells appear darker indicating a loss of signal on the image (right). For comparison, a disc was injected with fibrin gel alone, and appears brighter. A radiograph image (left) shows the sites of injection. Disc height was also increased following injection.**

In addition, disc height following injection as measured on radiographs was increased when compared to disc height prior to injection of the fibrin gel (not shown). This was used as an indictor that the cells seeded within the fibrin gel were in fact injected into the IVD.

*5.3.4  Cell Viability*

66

Labeling of hMSCs with Fe-Pro does not significantly impair cell viability. When compared against unlabeled hMSCs (control) the ratio of dead cells to live cells was not significantly different at day 0, 1, 2, 4, and 8 after labeling ($p > 0.25$). Figure 5.5 shows the ratio of dead cells to live cells for the labeled groups at various days as well as the unlabeled control group.
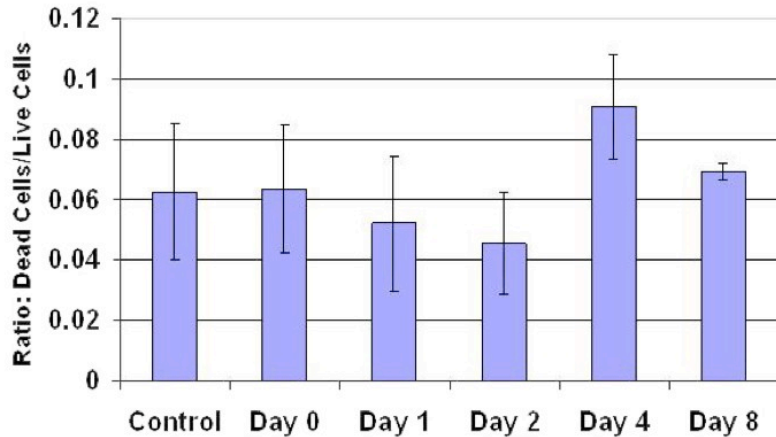


**Figure 5.5—Effect of iron oxide labeling on cell viability. Ratio of dead cells to live cells between unlabeled controls, and labeled cells at day 0, 1, 2, 4, and 8 after labeling was compared. There appears to be no significant difference in cell viability between labeled cells and unlabeled cells. Iron oxide labeling does not impair cell viability. (Error bars correspond to mean ± standard deviation)**

## 5.4  Discussion

The promise of utilizing stem cells to regenerate diseased or damaged tissue inherently requires an effective minimally invasive method for assessment. With MRI tracking, Fe-Pro labeled cells populations appear as signal voids and thus can be distinguished on MR images. Since MR imaging is non-invasive, the ability to track stem cells using this imaging modality is highly favorable. While MRI tracking of iron oxide-labeled cells has been examined in the past, the application of stem cell labeling to monitor IVD regeneration has not been previously investigated. Application of this

technique to the IVD is important because the ability to track implanted hMSCs within the disc would be valuable as a means of non-invasively monitoring the repair and regeneration process; this would make it possible to determine the effectiveness of such treatments. As demonstrated by the results of this study, Fe-Pro labeling and tracking using MRI has promise as a means for studying stem cell-based regeneration of the IVD. Specifically, the results show that SI loss of labeled cells on MR images can be quantitatively characterized by measurements of standard MRI relaxation parameters. In addition, Fe-Pro labeled cells can be distinguished from the surrounding environment, when placed within synthetic scaffolds such as hydrogels, as well within natural polymers implanted within native tissue. Lastly, cell viability of labeled cells does not appear to be affected by labeling with Fe-Pro.

The SI loss and subsequent contrast of labeled cells is strongest on GRE images (Figure 5.1a-b). GRE pulse sequences are utilized because they emphasize differences in magnetic susceptibility between tissues. For this particular methodology, stem cells labeled with Fe-Pro have increased susceptibility due to the highly magnetic iron oxide particles. In addition, GRE imaging allows for imaging at short TEs, where differences in SI and the associated contrast are the greatest for iron oxide-labeled cells. These characteristics of GRE pulse sequences allow for the strong contrast of iron oxide-labeled cells and their detection on the resulting images. Based on the results of the quantitative analysis, cells at a concentration of $1 \times 10^6$ cells/mL are distinguishable from unlabeled cells ($1 \times 10^6$ cells/mL) *in vitro*, with a statistically significant difference in $T_2^*$ values when both the two and three parameter fit are used. Clinically, the number of cells implanted for therapeutic applications will depend on the particular site and tissue of

interest, but it is important that the size of the transplanted cell population is within the detection limits of MRI.

Quantitative analysis of the obtained images reveals a significant loss in SI for labeled cells as compared to their unlabeled counterparts. One particularly interesting result is that addition of an additive noise term for the three-parameter fit resulted in an increase in the measured relaxation time. This is different from the analysis provided by Miller *et al*. suggesting that fitting of power images with an additive noise term should lead to a decrease in the measured relaxation time (80). The differing results of this study are likely because the $T_2$* values measured here for the highest concentration of labeled cells are extremely short. Thus the effect discussed by Miller *et al*. is less dominant in this situation. For the other concentrations of labeled cells, and unlabeled cells, the SI plots indicate that the signal loss is not saturated into the noise region, which leads to similar $T_2$* values using both the two-parameter and three-parameter fit.

Stem cells populations are often implanted within the body using a scaffold to create an environment that is conducive to cell attachment, proliferation, required gene expression, and formation of new functional tissue (85). Ideally, the scaffold should mimic the *in vivo* environment of the implanted cells for a defined period of time, until the implanted cells integrate into the surrounding native tissue. Presently, a variety of synthetic and natural polymers have been utilized for this purpose (3). MRI detection of labeled cells specifically within 3D scaffolds is an important consideration, because each type of polymer will have its own MRI signal characteristics and associated SI based on its material composition. Thus, the signal characteristics of the Fe-Pro labeled cells seeded within the 3D scaffold must be iron oxide dominated with sufficient SI loss and

associated contrast to allow for adequate detection. Among synthetic polymers, the use of hydrogels as 3D scaffolds for cell implantation has been well documented (86). The results of the present study demonstrate *in vitro* MR detection of Fe-Pro labeled hMSCs seeded within hydrogels. Labeled cells within the synthetic PEG hydrogels were also stained and imaged using confocal microscopy, illustrating that Fe-Pro labeled stem cells can be enclosed in a scaffold and remain live and viable. The resolution limits of a 3T MRI scanner preclude the ability to image single cells without the use of specially designed coil inserts. However, the ability to track a transplanted population of labeled stem cells longitudinally represents a significant step in the assessment of stem cell-based therapies. Furthermore, the ability to image single cells is possible with higher field strengths, and could become a clinical reality with advances in MR hardware technology.

In addition, the present study demonstrates the *ex vivo* detection of a transplanted population of labeled hMSCs seeded within a fibrin-based gel, a well characterized natural polymer utilized in tissue regeneration studies (7,87). As expected the discs implanted with Fe-Pro labeled cells appear as a hypo-intense region and so are detectable using MRI (Figure 5.4). These results are similar to those reported by Sykova *et al*. who were able to detect iron oxide-labeled rat stem cells when implanted *in vivo* within the spinal cord of injured rats (88). MRI has already been extensively used to image the IVD (78,89), and techniques have been developed to classify disc degeneration based on MR images (19,90-94). Consequently, as stem cell-based techniques for IVD regeneration are developed, utilizing MRI to image the disc and monitor therapy seems to be a feasible and promising endeavor.

Labeling of hMSCs with Fe-Pro does not appear to affect cell viability. These results are in agreement with those obtained by Arbab *et al.* who reported no increased cell death following labeling, and no reduction in proliferation capacity (54). As an indication that cells were in fact labeled in the present study and not attached to the cellular surface, Arbab *et al.* report 100% labeling efficiency, as determined by Prussian Blue staining and manual counting of cells prepared on microscope slides. In looking to future applications, both components of the Fe-Pro complex as well as heparin used for washing are FDA approved and so would not be expected to have toxic effects when utilized for cell labeling *in vivo*.

While this study utilized Fe-Pro labeling to provide negative contrast via SI loss, it is also possible to generate positive contrast with iron oxide labeling. Cunningham *et al.* have demonstrated the ability to label cells with SPIOs and use spectrally selective pulses to excite the off-resonance water surrounding the labeled cells (82). This allows for positive contrast of labeled cells compared to the surroundings. Based on these preliminary results, future studies should consider the ability to detect Fe-Pro labeled hMSCs using positive contrast MR imaging sequences, and the effects on detection within the surrounding tissue of the IVD. This can be done both qualitatively using the obtained images and quantitatively via MR relaxation parameters. Since negative contrast imaging is limited in its ability to distinguish between the presence of labeled cells and an inherent signal void in the image, the use of positive contrast to confirm the presence of labeled cells would be beneficial. In principle, it is possible to use a combination of positive and negative contrast imaging to track transplanted labeled cells simply by varying the pulse sequence used during each scan. As a result, it is expected that positive

contrast imaging could be used for initial detection following transplantation of labeled cells within the IVD, followed by high resolution negative contrast imaging to image cells within the surrounding tissue once they have been detected.

In conclusion, these studies demonstrate that the established technique of labeling iron oxides and subsequent MR imaging appears to be a feasible methodology for monitoring stem cell-based regeneration of the IVD. As stem cell-based therapies continue to emerge as treatment methods for diseased or damaged tissues, the use of this technique for non-invasive assessment shows promise. With the demonstrated *in vitro* and *ex vivo* results presented here, future studies should include *in vivo* longitudinal studies of stem cell tracking by means of MRI. As this technique continues to show promising results, its clinical application to treatment of IVD degeneration and a variety of other disease conditions is expected.

## 5.5   <u>Acknowledgements</u>

# Chapter 6: Research Studies of Cell Labeling with MPIOs

## 6.1 Introduction

While MR-based stem cell tracking and stem cell-based regeneration of cartilage have been active fields of study independently, no studies to date have looked at the potential of MPIO-based stem cell labeling to monitor cartilage regeneration. Consequently, a major aim of these studies was to further examine MPIO labeling of MSCs and investigate this technique for clinically applicable monitoring of cartilage tissue regeneration. To this end, MSCs were labeled with MPIOs and a population of cells was detected *in vitro*, and *ex vivo* using a clinical MR scanner. In addition to detection, applying this technique to monitoring cells within cartilage raises questions about the effect that labeled cells will have on MR scans typically used to probed cartilage integrity. Hence *ex vivo* $T_{1\rho}$ imaging typically used to detect proteoglycans (96-98) within cartilage was performed in the presence of MPIO-labeled cells. Furthermore, fluorescence microscopy was used for co-validation of labeling and to investigate the presence of extracellular particles following labeling. In addition, labeled cells were tested for labeling efficiency, cell viability, and the effect of labeling on chondrogenic differentiation.

In addition to studies examining clinical monitoring of stem cells labeled with MPIOs, experiments were also conducted in order to investigate the ability to detect labeled cells using high-field (14T) MRI. The increase in signal associated within this field strength makes it possible to image labeled cells at near cellular resolution. As a result it is likely possible to detect single cells containing multiple particles or small numbers of cells within a local environment. Labeled cells were imaged at 14T *in vitro*

within a commercially available hydrogel, as well as *ex vivo* within the muscle of a mouse hind limb. Finally, imaging of labeled cells at multiple time points following labeling was performed at 14T in order to examine the longitudinal ability to detect MPIO-labeled cells using MRI.

The results of these studies demonstrate the promise of utilizing the MPIO-labeling technique for monitoring cartilage regeneration as well as in other musculoskeletal tissue engineering applications. In addition, these studies highlight the need for future development of this technique as a clinically relevant means of monitoring cell-based tissue engineering strategies. Lastly, the results of the high-field imaging studies demonstrate the future potential of MRI for clinically applicable cell tracking with continued advancements in imaging technology.

## 6.2    Materials and Methods

### 6.2.1   Cell Isolation and Expansion

Bone marrow-derived MSCs were harvested from the iliac crest of female young adult (>5 kg) New Zealand White rabbits immediately after animal sacrifice based on a technique adapted from Johnstone *et al*. (99). Briefly, the marrow was aspirated using a 10 mL syringe containing heparin (5000 U). The samples were placed in 75 $cm^2$ tissue culture flasks containing standard tissue culture media: high glucose DMEM (Invitrogen) with 10% FBS and 1% penicillin/streptomycin (Invitrogen). After 48 hours, non-adherent cells were removed, and the remaining adherent cells were maintained in the same media (changed every 2-3 days), expanded using standard conditions (37°C and 5% $CO_2$), and passaged 1:4 at 80-90% confluence. Cells were sub-cultivated using 0.25% trypsin with 1

mM EDTA (Invitrogen) and used for experiments between passages 6-10 to avoid issue with cell senescence.

### 6.2.2 Stem Cell Labeling

Rabbit MSCs (rMSCs) were labeled with MPIOs using a technique described by Hinds *et al*. (100). Briefly, 1.63 μm diameter encapsulated micro-spheres (Bangs Laboratories, Fishers, IN, USA) were added to standard tissue culture media at a concentration of 10 μL/mL and mixed for 10 minutes. The stock solution of contrast agent particles used for cellular labeling consisted of an iron concentration of ~ 4.25 mg/mL, and addition into the cell culture media resulted in a final iron concentration of 2.8 μg/mL used for labeling. After mixing, the labeling media was added to an 80% confluent MSC monolayer in 75 cm$^2$ tissue culture flasks (n=3), and cell cultures incubated overnight. Unlabeled cell flasks (n=3) were also used as controls for each set of experiments. Following overnight labeling with MPIOs samples were washed three separate times with PBS to remove excess particles not taken up by cells. Cells were then treated with trypsin, collected, and counted for further experiments. Cell viability was assayed during counting using Trypan Blue (Invitrogen). For longitudinal imaging experiments, cells were maintained under standard conditions, and sub-cultivated upon confluence for the length of the culture period.

### 6.2.3 Chondrogenesis

*In vitro* chondrogenesis via pellet culture of labeled MSCs and unlabeled MSC controls was induced using a Chondro-Bulletkit containing transforming growth factor (TGF)-β3 (Lonza, Walkersville, MD, USA) according to the manufacturer's protocol for

4 weeks. Following differentiation, labeled (n=2) and unlabeled (n=2) pellets were fixed in 10% formalin, dehydrated in ethanol, and embedded in paraffin using standard tissue processing techniques. Embedded sections (5 μm thickness) were stained with hematoxylin and eosin (H&E), safrinin-O, and fast green, visualized by light microscopy (Olympus CX41, Center Valley, PA, USA), and photographed (Nikon Coolpix 5000, Melville, NY, USA). For GAG content, labeled (n=6) and unlabeled (n=6) samples were digested overnight in papain, and chondrotin sulfate concentration was measured using dimethylmethylene blue dye (DMMB; Biocolor, Carrickfergus, UK). A spectrophotometer (Varian Carey 300, Walnut Creek, CA, USA) was used to measure the absorbance of the pellet samples at 656 nm and GAG content was determined by comparing the obtained values to a known standard curve. The range of standards was large enough to ensure that all experimental samples fell within the linear range. Differences between labeled and unlabeled cells were compared using a Student's $t$ test (p<0.05).

### 6.2.4  Fluorescence Imaging and Analysis

To visualize the presence of MPIOs within cells following labeling, fluorescence imaging of the Dragon Green tag (Ex/Em: 480/520 nm) associated with the MPIOs was performed along with unlabeled cell controls. For studies investigating the presence of excess unincorporated particles following labeling and PBS washing, cells were seeded on Permanox Lab-Tek tissue culture slides (n=4; Fisher Scientific; Hampton, NH, USA) and grown to 80% confluence before labeling. Following labeling and three PBS washes, cells were co-labeled with a Hoechst stain (Fisher; Ex/Em: 350/461 nm) by adding a 1:200 dilution of the stock solution to each tissue culture well for 5 minutes. Cells labeled

only with the Hoechst stain was also visualized as controls (n=4). Images were obtained using an Olympus BX60 microscope with fluorescent attachment and captured using an AxioCam MRm system (Zeiss, Thornwood, NY, USA). National Institutes of Health ImageJ (Bethesda, MD, USA) software was used for processing and image overlay.

Flow cytometry was used to quantify the mean fluorescent intensity (MFI) in order to analyze MPIO labeling efficiency (n=3 flasks). Following labeling and PBS washing, cells were collected and analyzed using a FACS Calibur Cell Counter System (BD Biosciences) set to the FL1 channel (Ex/Em: 488/530±15 nm). The forward and side scatter of the events was adjusted to differentiate between live and dead cells. Events within the gated live cell population were measured for MFI with at least 10,000 events per sample. Unlabeled cells were used for calibration and multiple samples from each labeled flask were analyzed and the results averaged. All flow cytometry parameters were fixed in comparing a single analysis and all samples were run consecutively on a single machine with conserved analysis parameters.

### 6.2.5   Ficoll Suspension and Hydrogel Encapsulation

In one set of experiments, labeled cells ($1 \times 10^6$ cell/mL) were suspended in eppendorf tubes containing 1.0 mL Ficoll (n=3; GE Healthcare Biosciences, Piscataway, NJ, USA) to prevent cell settling during imaging. As negative controls, unlabeled cells (n=3) at the same concentration and Ficoll alone (n=3) were also imaged. For longitudinal imaging experiments, cells were suspended in 1.0 mL of Ficoll within 10 mm NMR tubes at concentrations of $5 \times 10^4$ cells/mL. Unlabeled cells at the same concentrations were utilized as negative controls For the second set of experiments, labeled cells were loaded into Puramatrix hydrogel (3DM, Cambridge, MA, USA) at a concentration of $5 \times 10^4$ or

$5\text{x}10^5$ cells/mL within 10 mm NMR tubes. Encapsulation of the cells within the gel was performed according to the manufacturer's instructions. Unlabeled cells at the same concentrations were also encapsulated within Puramatrix as experimental controls.

### 6.2.6  *Confocal Microscopy and Nomarski Optics*

For studies validating internalization of MPIO particles within rMSCs following labeling, cells were seeded on Permanox Lab-Tek tissue culture slides (n=2) and grown to 80% confluence before labeling. Following labeling and PBS washing, cells were co-labeled with a Hoechst stain (Fisher; Ex/Em: 350/461 nm) by adding a 1:200 dilution of the stock solution to each tissue culture well for 5 minutes. Cells labeled only with the Hoechst stain was also visualized as a control (n=2). Confocal microscopy was performed using a Nikon FN1 microscope and Nikon C1si Spectral Confocal using an Ex/Em: 405/450±30 nm for Hoechst stain detection, and Ex/Em: 488/525±50 nm for detection of the Dragon Green tag present within the MPIO particles. Each slice of the 40-slice volume stack had a thickness of .625 μm resulting in a total volume of 25 μm.

In order to validate the presence of MPIO particles contained within the cells throughout longitudinal MR imaging, differential interference contrast (DIC) imaging was performed at each time point (0, 1, 3, and 6 weeks post labeling). The day before microscopy, labeled cells in culture were lifted using trypsin and seeded on Permanox Lab-Tek tissue culture slides (n=4) at 80% confluence. DIC was performed using a Nikon Eclipse Ti microscope and images were acquired using a Photometrics Evolve 512 electron multiplying charge coupling device (EMCCD) black-and-white camera attachment (Tuscon, AZ, USA).

### 6.2.7  Ex Vivo Animal Model Implantation

To investigate detection of MPIO-labeled rMSCs within native tissue, an *ex vivo* bovine osteochondral knee defect model was used. A cylindrical defect (diameter = 5 mm; height ~ 9 mm) was created in each condyle of a single bovine distal femur. Prior to implantation, MPIO-labeled rMSCs were encapsulated within Puramatrix according to the manufacturer's instructions. Unlabeled control rMSCs were also encapsulated within a separate Puramatrix hydrogel. Following gelation, the two constructs were filled as follows: (1) Puramatrix construct containing MPIO-labeled rMSCs ($5x10^6$ cells/mL); (2) Puramatrix construct containing unlabeled rMSCs ($5x10^6$ cells/mL). Care was taken to ensure that the constructs would not leak out of the defects during imaging, and following MRI each defect was visually reexamined to verify the presence of the construct.

Labeled cells were also injected into a mouse muscle hind limb model. Prior to implantation, $1x10^6$ labeled cells were concentrated in 50 μL PBS. Injection into the soleus muscle of a mouse hind limb was performed using a 3 mL Luer-Lok Tip with a 21-gauge needle attached (BD Biosciences). The entire volume of the cell suspension was injected into the limb. As a negative control, unlabeled cells at the same concentration were injected into the soleus muscle of a separate mouse hind limb.

### 6.2.8  3T and 14T MRI

All 3T imaging was performed on a 3T Signa Excite system (GE Medical Systems) using a quadrature transmit/receive knee coil (GE Medical Systems). For *in vitro* cell imaging in solution, the tubes containing samples were placed in a plastic container filled with water in order to remove the air susceptibility artifact, and all imaging was carried out at room temperature (20°C). Each tube was imaged alone to prevent image distortions

caused by the iron present in neighboring tubes and all tubes were imaged within the same location in the magnet to limit the effect of main field inhomogeneities. 2D GRE imaging of the tubes was performed as a single coronal slice with a TE/TR = 4-24/500 ms, a 12 cm FOV, flip angle = 90°, matrix size = 256x256, 468 μm in-plane resolution, bandwith (BW) = 15.63 kHz, and slice thickness = 3 mm. SE imaging was performed using the same parameters, except with a TE/TR = 20-200/2000 ms. Image analysis was performed using dedicated software written in MATLAB to measure the SI as a line profile passing through the center of the tube in each image, and to determine the mean SI for a defined ROI. The line profile analysis consisted of sampling the SI value for every fifth pixel of the image passing horizontally through the center of the tube. Differences in SI between labeled and unlabeled cells were compared using a Student's *t* test (p<0.05) for both the line profile and ROI analysis.

*Ex vivo* imaging of cells within the bovine knee was performed using a 3D sagittal spoiled GRE (SPGR) sequence with a TE/TR = 6.7/15 ms, flip angle = 12°, FOV = 12 cm, matrix size = 512x256, and slice thickness = 1 mm. In addition, a 3D $T_{1\rho}$-weighted sequence (101) was used to image the bovine knee sagittally, with TE/TR = 3.7/9.3 ms, FOV = 12 cm, matrix size = 256x128, slice thickness = 1 mm, BW = 31.25 kHz, views per segment = 64, time of recovery ($T_{rec}$) = 1500 ms, time of spin lock (TSL) = 0, 10, 40, and 80 ms, and frequency of spin lock = 500 Hz. Image processing software written in IDL was used to generate $T_{1\rho}$ maps by fitting the data on a pixel-by-pixel basis to the equation:

$$S(TSL) \sim \exp(-TSL/ T_{1\rho}) \tag{6.1}$$

Following segmentation using dedicated IDL software masked $T_{1\rho}$ maps were overlaid onto the SPGR images using software written in MATLAB.

High-field imaging was performed using a 600 MHz scanner (Varian, Palo Alto, CA, USA) with either a 10 mm broadband or 40 mm broadband coil (Varian). NMR tubes containing samples were imaged using the 10 mm coil, and all *in vitro* experiments were performed in duplicate. GRE multi-slice (GEMS) 2D imaging was performed using a TE/TR = 4.48-26.88/200 ms with a scan time of ~ 7 minutes, and flip angle = 50°. SE multi-slice (SEMS) 2D imaging was performed using a TE/TR = 15/1000 ms with a scan time of ~ 17 minutes. Both sequences were acquired with a slice thickness = 0.4 mm, FOV = 10 mm, and matrix size = 256x256, resulting in an in-plane resolution of 40 μm. Longitudinal MR imaging experiments were performed using the same setup and imaging parameters at 0, 1, 3, and 6 weeks post labeling. Quantitative line profile analysis was performed on 10 sample points per tubes using VnmrJ software (version 2.3A; Varian). The resulting measurements were used to create plots of SI versus distance from the chosen sample point (pixel) in Microsoft Excel. *Ex vivo* MR imaging at 14T was performed on the mouse hind limb by placing it in a 50 mL tube and using the 40 mm coil. A 3D GRE sequence with TE/TR = 2.19/25 ms, and flip angle = 12° was utilized. The resolution of the obtained images was $125x117x250 \ \mu m^3$.

## 6.3    Experimental Results

### 6.3.1    *MPIO Labeling and Signal Characteristics*

The *in vitro* results indicate efficient cellular uptake of MPIOs and corresponding distinguishable SI loss of labeled cells on MR images. Figure 6.1a shows a single MSC

cell labeled with MPIOs (fluorescence overlaid on bright field) as demonstrated by the fluorescent tag associated with the iron oxide contrast agent that is not present within the control cell (Figure 6.1b).
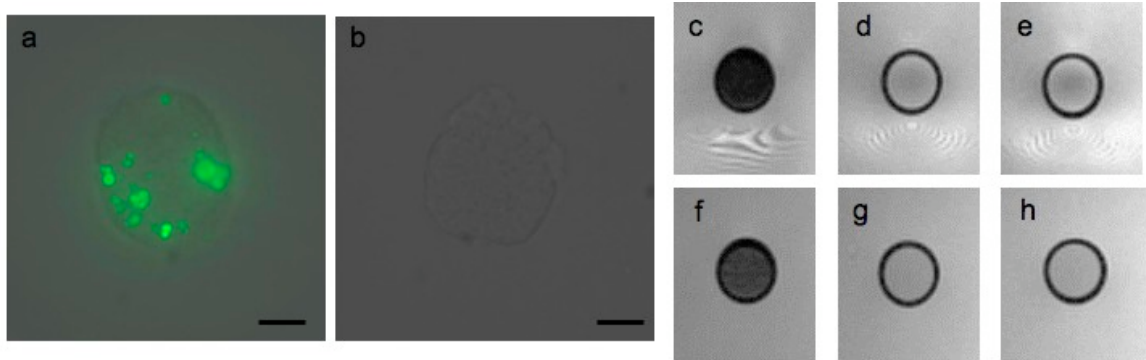


**Figure 6.1—Iron oxide labeling of rMSCs with MPIOs. (a) Fluorescence microscopy image of a representative cell after overnight labeling. The Dragon Green fluorescence indicates cellular uptake of the iron oxide contrast agent, which is not present within the (b) representative unlabeled control cell; (c) (d) & (e) GRE imaging (TE/TR = 8/500 ms) of labeled cells ($1x10^6$ cells/mL), unlabeled cells ($1x10^6$ cells/mL), and empty Ficoll respectively; (f) (g) & (h) SE imaging (TE/TR = 150/2000 ms) of labeled cells ($1x10^6$ cells/mL), unlabeled cells ($1x10^6$ cells/mL), and empty Ficoll respectively. Both GRE and SE imaging demonstrate a visible signal loss associated with iron oxide labeling that is not present within unlabeled cells or the Ficoll solution alone. (Scale bar = 10 μm)**

Flow cytometry analysis following overnight labeling resulted in a labeling efficiency of 86±3 %. Trypan blue staining to detect the presence of dead cells did not show any effect of labeling on cell viability as compared to unlabeled controls (not shown). Figure 6.2 shows confocal microscopy images of labeled cells and further validates cellular uptake and internalization of the MPIO particles. The volume rendering of the stack obtained shows the presence of MPIO particles throughout the cell (Figure 6.2c). In addition, the vast majority of the MPIO particles within the cells are outside of the nucleus as expected.

MPIO-labeled rMSCs appear as a distinct hypo-intense region when imaged *in vitro* via 3T MRI using both GRE (Figure 6.1c-e) and SE imaging (Figure 6.1f-h). MPIO

labeling has a greater effect on the GRE sequence but is still clearly visible as a signal

void on the SE image.
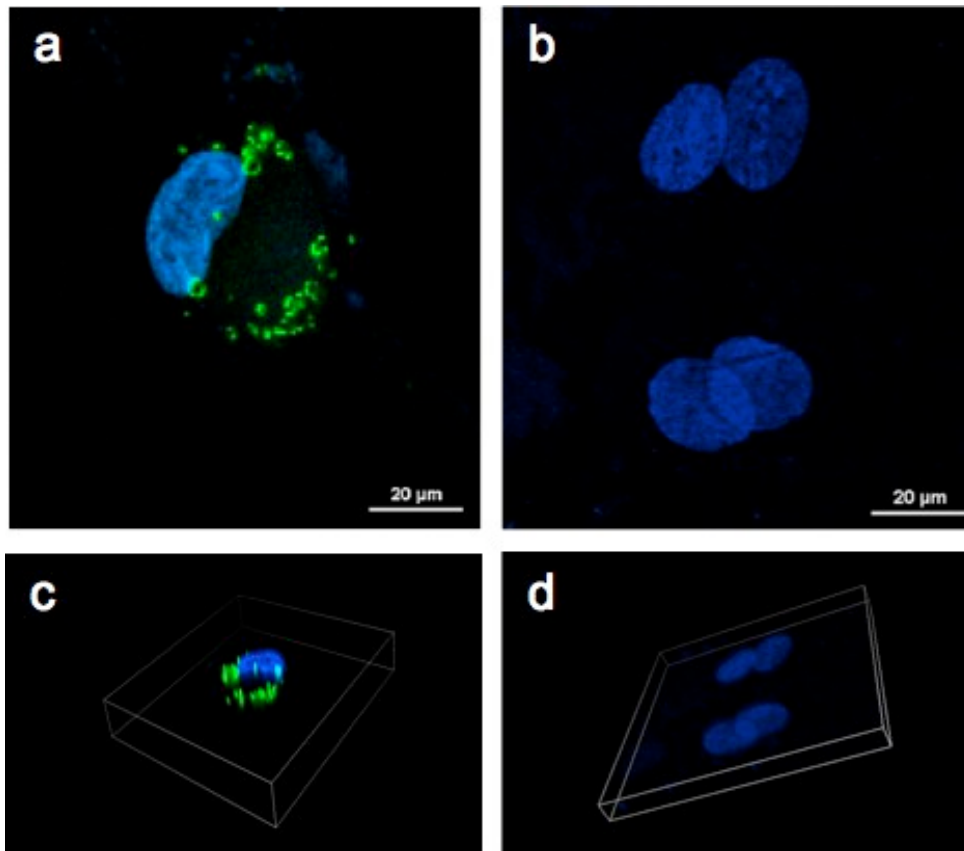


**Figure 6.2—Confocal microscopy of MPIO-labeled rMSCs. (a) Single slice of an MPIO-labeled cell showing the presence of MPIO particles (green fluorescence) within the cell outside of the nucleus (blue fluorescence); (b) unlabeled control cells showing only staining of the nucleus; (c) volume rendering of a labeled cell obtained by combining each individual slice into a compressed stack. The rendering confirms MPIO internalization within the cell and the 3D distribution of the MPIO particles; (d) volume rendering of unlabeled cells. The unlabeled cells are likely in the process of cell division. (Scale bar = 20 μm)**

Quantitative characterization of this SI loss based on line profile analysis and

measurement of the mean SI for the ROI corresponding to each tube is depicted in Figure

6.3. For 3T GRE imaging, MPIO-labeled cells ($1 \times 10^6$ cells/mL) produce a significant

($p < 0.05$) loss in SI throughout the tube compared to the control tubes (Figure 6.3a). SE

imaging results in a similar significant ($p < 0.05$) loss in SI throughout the tube containing

labeled cells (Figure 6.3b). The particular TE values for the GRE (TE = 8 ms) and SE (TE = 150 ms) sequence were chosen because they resulted in the greatest contrast between labeled cells and the control tubes. Figure 6.3c shows the mean SI for the ROI corresponding to each tube for both GRE and SE imaging. The significant loss (p<0.05) of SI for MPIO-labeled rMSCs is clearly visible.
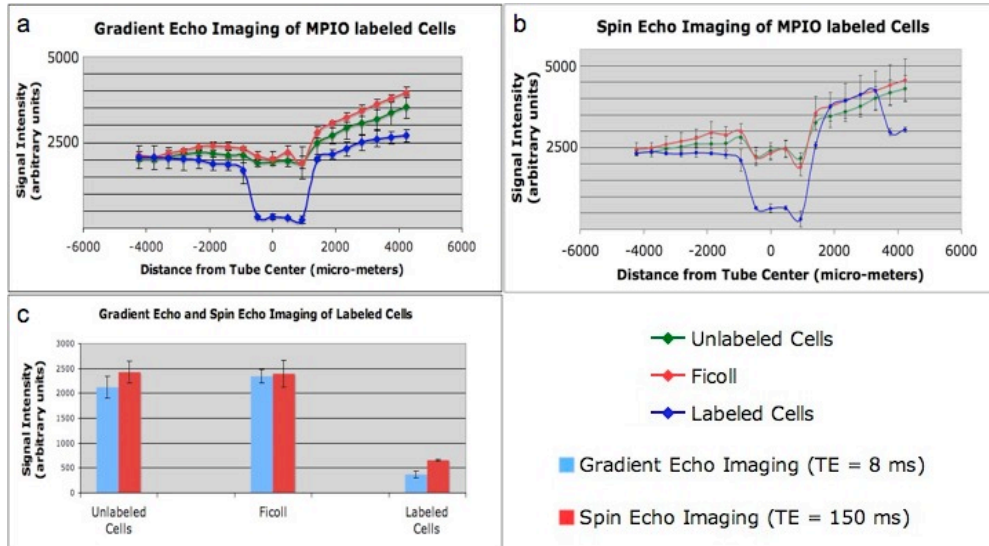


**Figure 6.3—Quantitative analysis of signal loss associated with MPIO labeling of cells. Line profiles demonstrate the sharp signal drop off associated with labeled cells, detectable using both (a) GRE (TE/TR = 8/500 ms) imaging; and (b) SE (TE/TR = 150/2000 ms) imaging. Differences in SI between labeled cells and control tubes are significant (p<0.05) for both GRE and SE imaging; (c) SI values for ROIs corresponding to tubes of labeled cells, unlabeled cells, and Ficoll, demonstrating significant (p<0.05) SI loss that is detectable using both GRE and SE imaging. (Data is presented as mean±standard deviation for n=3 samples; cell concentration = $1 \times 10^6$ cells/mL)**

High-field MR imaging at 14T also demonstrates the ability to distinguish MPIO-labeled cells. With the resolution achieved at this field strength it is possible to detect small populations of cells that are loaded with multiple particles. Figure 6.4 shows GRE imaging of MPIO-labeled cells encapsulated within a Puramatrix hydrogel, as well as unlabeled cells utilized as a negative control.
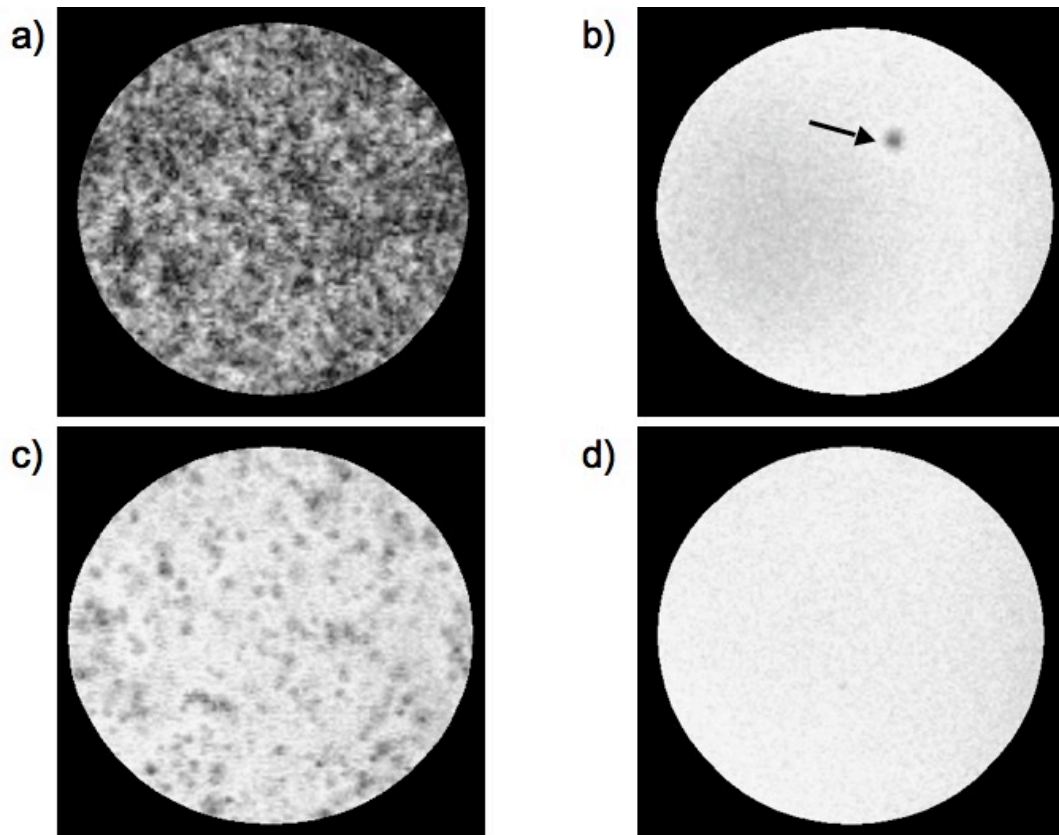
**Figure 6.4—GEMS MR imaging of MPIO-labeled rMSCs encapsulated within Puramatrix hydrogel. Single slice GRE image (TE/TR = 4.48/200 ms) of (a) MPIO-labeled cells ($5x10^5$ cells/mL); (b) unlabeled (control) cells ($5x10^5$ cells/mL); (c) MPIO-labeled cells ($5x10^4$ cells/mL); (d) unlabeled (control) cells ($5x10^4$ cells/mL). Labeled cells are distinguishable as a signal void compared to unlabeled cells especially in (c) where the cell seeding density is low. The hypo-intense region (arrow) present in (b) is likely due to an impurity or bubble formed during gelation of the Puramatrix hydrogel.**

At the high concentration of cells there appears to be a saturation of signal loss resulting from the high cell density and abundance of loaded iron. Similarly, Figure 6.5 shows SE imaging of MPIO-labeled cells encapsulated within Puramatrix along with unlabeled cells for comparison. The signal loss associated with labeling is less apparent than for GRE imaging but labeled cells are still clearly distinguishable compared to unlabeled control cells at the same concentration.
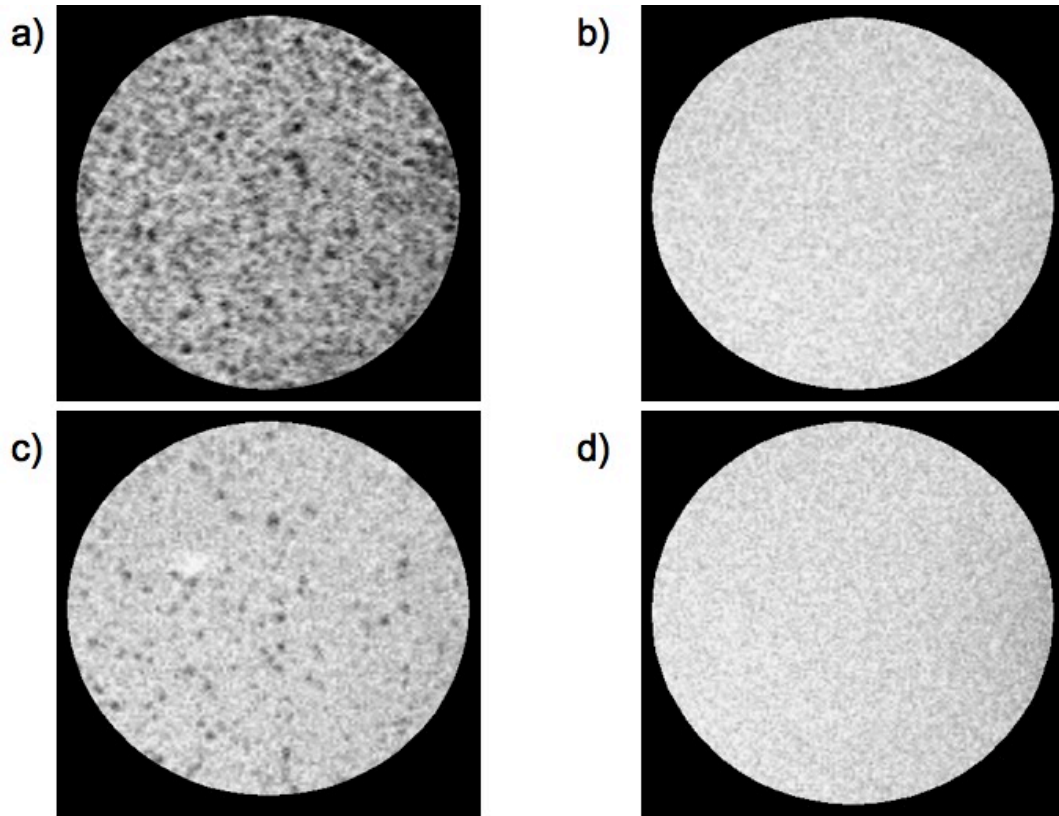
**Figure 6.5—SEMS MR imaging of MPIO-labeled rMSCs encapsulated within Puramatrix hydrogel. Single slice SE image (TE/TR = 15/1000 ms) of (a) MPIO-labeled cells (5x10$^5$ cells/mL); (b) unlabeled (control) cells (5x10$^5$ cells/mL); (c) MPIO-labeled cells (5x10$^4$ cells/mL); (d) unlabeled (control) cells (5x10$^4$ cells/mL). Labeled cells are distinguishable as a signal void compared to unlabeled cells, especially in (c) where the cell seeding density is low.**

Quantitative line profile analysis of the obtained 14T MR images demonstrates the loss in SI associated with MPIO-labeling and the effect on the surrounding *in vitro* environment (Figure 6.6). For GRE imaging at the highest concentration of labeled cells (Figure 6.6a), labeling causes a drop in SI that is approximately 10% of background. In addition, the extent of the signal loss though decreasing with distance from the center, still results in SI values ~ 50-60% of background at a distance 400 μm away. At the lower concentration of MPIO-labeled cells (Figure 6.6b) the SI drop is less pronounced reaching only 40% of background at the center. In addition, at a distance of 400 μm away from the center point, the SI values are close to 100% of background.
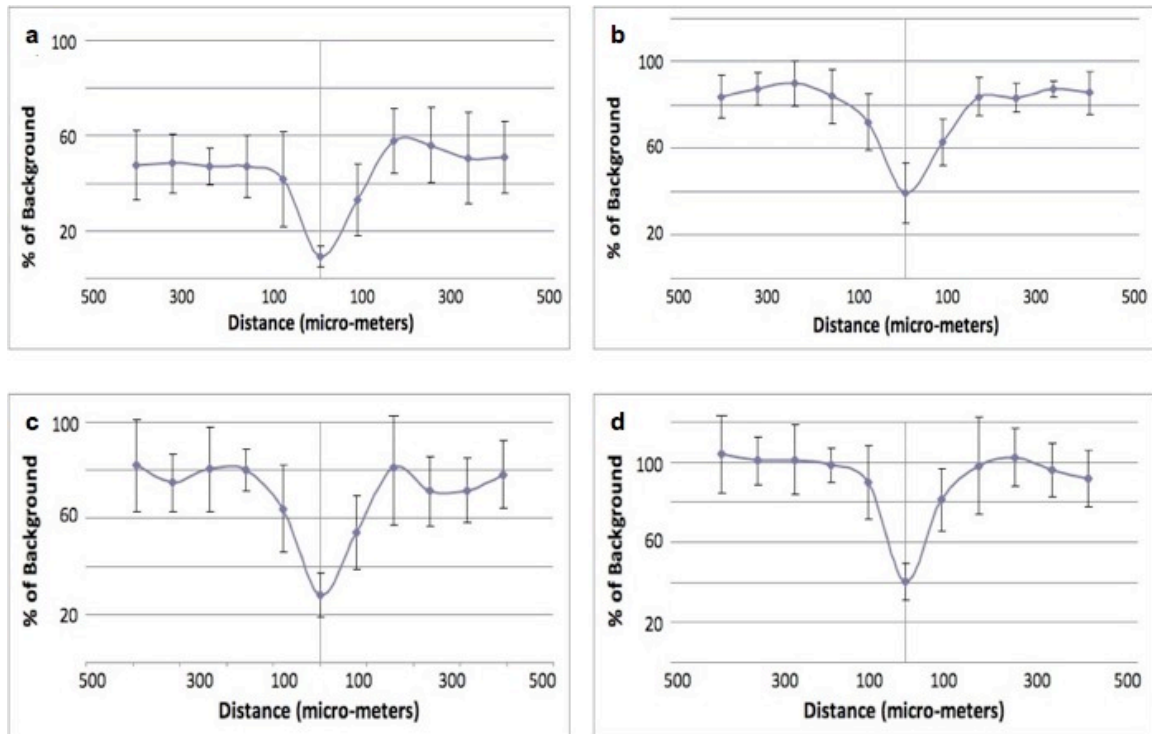
**Figure 6.6—Line profile analysis of MR images of MPIO-labeled cells encapsulated within Puramatrix hydrogel. Profile plots for ten representative points on the image demonstrating the linear extent of cell labeling (x-axis) and the amount of SI loss compared to the background hydrogel (y-axis). Values are represented as % of background in which background SI corresponds to Puramatrix hydrogel alone. (a) GRE imaging ($5 \times 10^5$ cells/mL); (b) GRE imaging ($5 \times 10^4$ cells/mL); (c) SE imaging ($5 \times 10^5$ cells/mL); (d) SE imaging ($5 \times 10^4$ cells/mL). Each point likely corresponds to a single labeled cell or small cluster of labeled cells encapsulated within the hydrogel.**

For SE imaging of MPIO-labeled cells at the higher concentration (Figure 6.6c), at the center point there is SI drop to 30% of background. Moving out from the center point in both directions, there is a gradual return to background intensity values with distance, but at 400 μm SI values remain at 80% of background. Finally for SE imaging of MPIO-labeled cells at the lower concentration, the SI drop at the center point is approximately 40% of baseline, and returns rapidly to 100% of background with distance in both directions.

*6.3.2    Longitudinal MR Imaging of MPIO-labeled Cells*

MPIO labeled cells were also imaged at successive time points in order to determine the ability to longitudinally detect labeled cells *in vitro*. Figure 6.7 shows the result of the GRE MR imaging at 0, 1, 3, and 6 weeks post labeling. The day after labeling, images show the greatest distribution of signal loss, but signal loss associated with MPIO particles is still present at the 6-week time point.
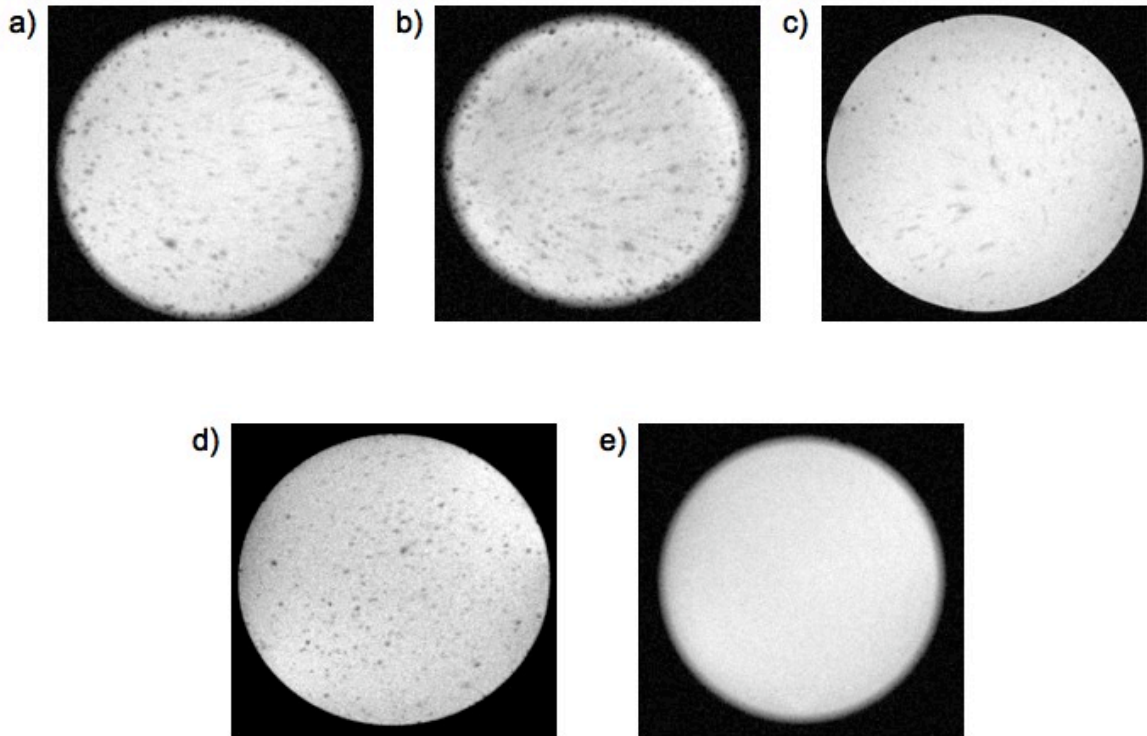


**Figure 6.7—Longitudinal GRE (TE/TR: 4.48/200 ms) MR imaging of MPIO-labeled cells. (a) 1 day after labeling (initial detection); (b) 1 week after labeling; (c) 3 weeks after labeling; (d) 6 weeks after labeling; (e) unlabeled control cells. High resolution MRI demonstrates detection of labeled cells throughout the 6-week imaging study with clear signal loss still present at the last time point. (Concentration = 5 x 10$^4$ cells/mL; image resolution ~ 40 $\mu$m)**

As expected, signal loss associated with MPIO-labeling is less pronounced using SE imaging (Figure 6.8), but distinct signal voids are still detectable. Immediately following labeling there are several signal voids within the image, which gradually diminishes to a few distinct voids at the 6-week time point. To validate the presence of MPIO particles within cells at each of the time points, DIC microscopy was performed on cells in culture

at 0, 1, 3, and 6 weeks post-labeling (Figure 6.9). DIC imaging shows the abundance of MPIOs immediately following labeling, and a gradual decrease in the number of particles throughout the 6-week period. However, trace MPIOs are still detectable via DIC microscopy at the 6-week time point.
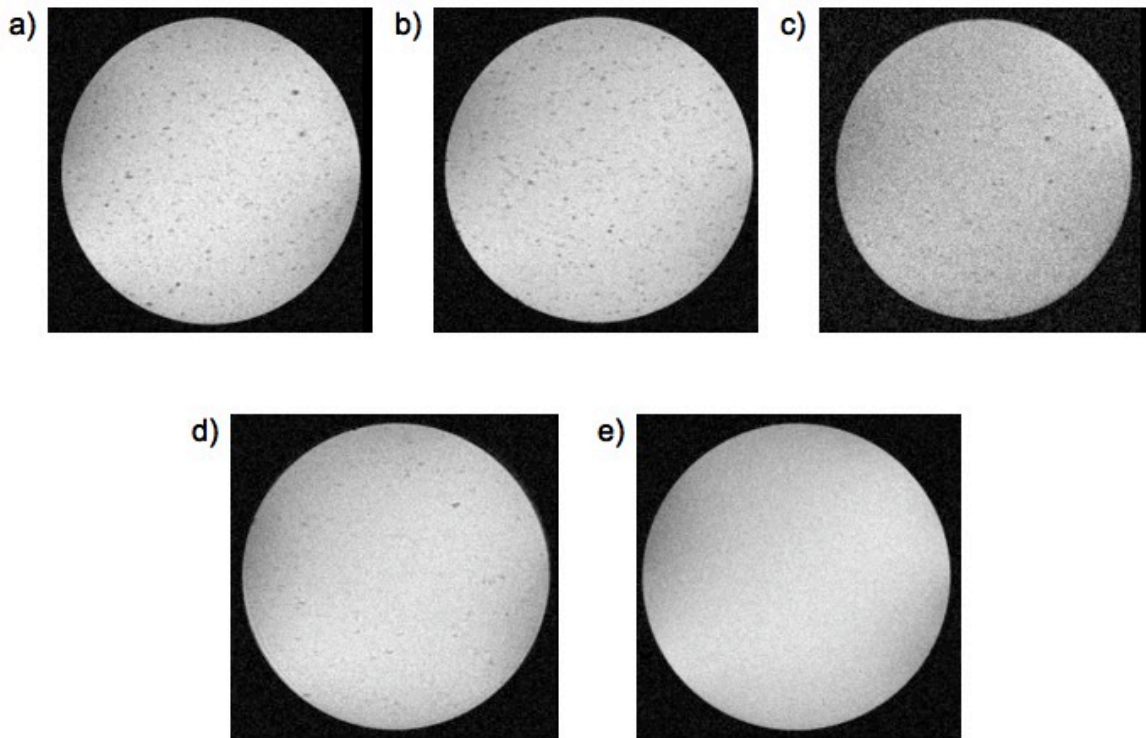


**Figure 6.8—Longitudinal SE (TE/TR: 15/1000 ms) MR imaging of MPIO labeling. (a) 1 day after labeling (initial detection); (b) 1 week after labeling; (c) 3 weeks after labeling; (d) 6 weeks after labeling; (e) unlabeled control cells. High resolution MRI demonstrates limited detection of labeled cells throughout the 6-week imaging study compared to GRE imaging. While SI loss associated with labeling can be detected at 1 day and 1 week after labeling, few particles are detectable at the later time points. (Concentration = 5 x 10$^4$ cells/mL; image resolution ~ 40 μm)**

### 6.3.3  Ex Vivo Imaging

MPIO-labeled cells were seeded within a Puramatrix hydrogel and detected *ex vivo* within a bovine knee osteochondral defect (Figure 6.10). While unlabeled cells in the hydrogel appear to have similar signal characteristics to the cartilage (Figure 6.10a),

MPIO-labeled cells can be visualized as a distinct hypo-intense region within the osteochondral defect (Figure 6.10b).
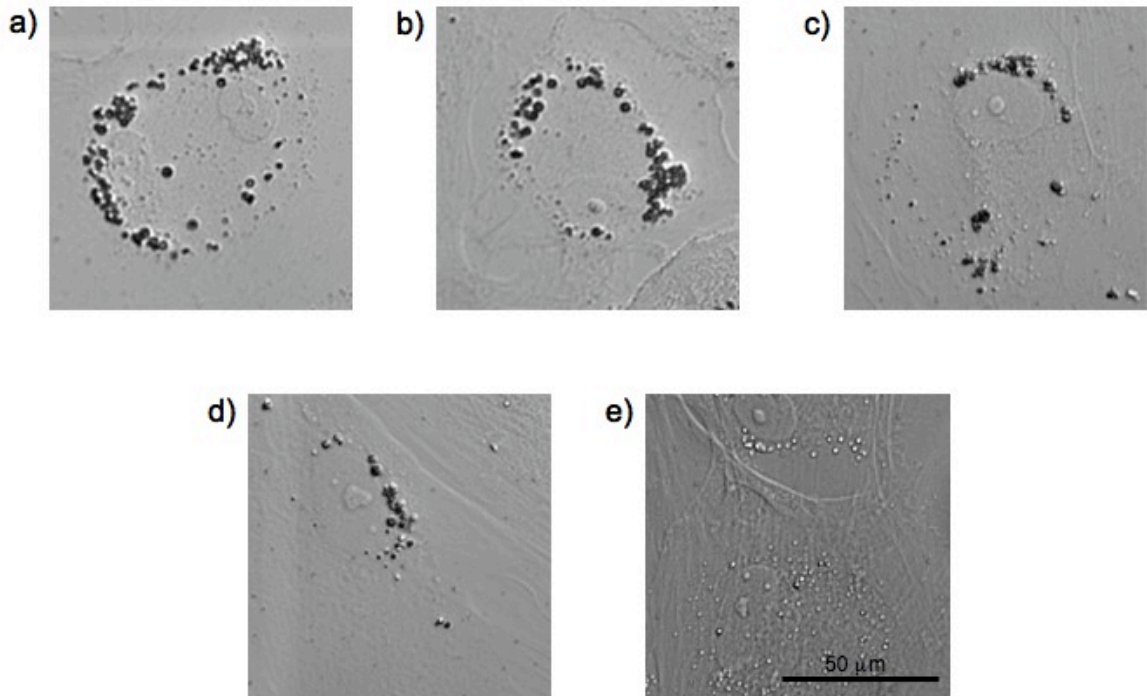


**Figure 6.9—Longitudinal DIC microscopy of MPIO-labeled cells. (a) 1 day after labeling (initial detection); (b) 1 week after labeling; (c) 3 weeks after labeling; (d) 6 weeks after labeling; (e) unlabeled control cells. Iron oxide particles are detectable over the 6-week period, but show an overall longitudinal decrease in the concentration of particles within cells. (Scale bar = 50 μm and applies to all images)**

This loss of SI can be distinguished from the native articular cartilage as well as the underlying bone. $T_{1\rho}$ imaging of the implants within the osteochondral defects demonstrates strongly elevated $T_{1\rho}$ values for both unlabeled and labeled cells (Figure 6.10c-d), as compared to native cartilage, which has values ranging from 80-100 ms. For both the unlabeled and the labeled cells in Puramatrix, there also appears to be a large degree of heterogeneity in the $T_{1\rho}$ values.

*Ex vivo* imaging was also performed of MPIO-labeled cells implanted within the soleus muscle of a mouse hind limb. Figure 6.11a shows four consecutive slices from a

3D GRE sequence in which the labeled cells can be detected as a hypo-intense region within the surrounding muscle tissue environment.
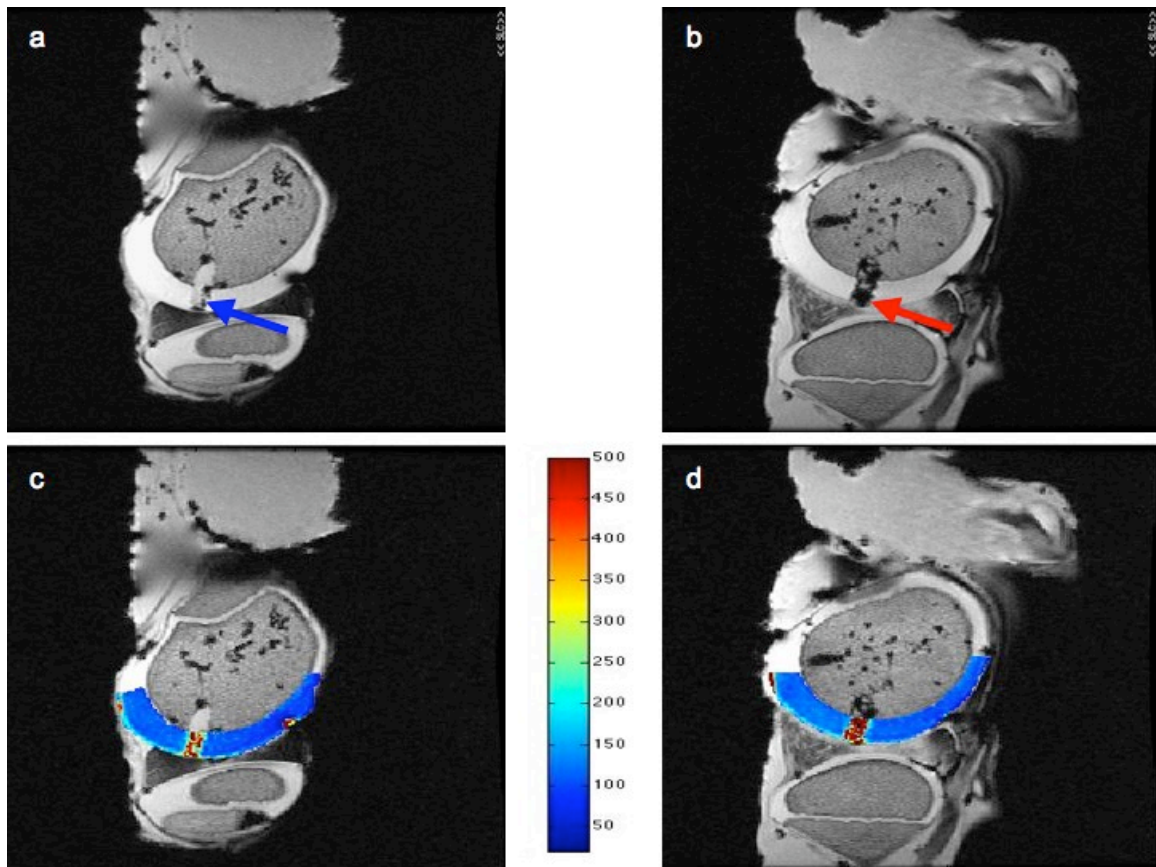


**Figure 6.10—*Ex vivo* MRI of implanted cells within a bovine osteochondral defect. SPGR imaging (TE/TR = 6.7/15 ms) of (a) unlabeled MSCs; and (b) MPIO-labeled MSCs. Labeled cells are visible as a distinct void with blooming artifact, as compared to unlabeled cells that appear to have a similar SI to native cartilage. Colormap overlaid on a SPGR image of (c) unlabeled MSCs; (d) MPIO-labeled MSCs. The colorbar shows the associated $T_{1\rho}$ values (ms). Both unlabeled cells and labeled cells in the Puramatrix hydrogel show elevated $T_{1\rho}$ values compared to native cartilage. (Concentration = $5x10^6$ cells/mL)**

For comparison, unlabeled cells at the same concentration were injected into the soleus muscle of a separate mouse hind limb. As shown in Figure 6.11b, unlabeled cells cannot be distinguished from the surrounding tissue.

*6.3.4   Chondrogenic Differentiation*

In order to assess the effect of MPIO labeling on MSC chondrogenesis, MPIO-labeled rMSCs underwent *in vitro* differentiation. Safrinin-O and H&E staining was used to visually assess the differentiation capacity of MPIO-labeled rMSCs. This dye combination stains GAG red-pink, nuclei blue-purple, and the cytoplasm green.
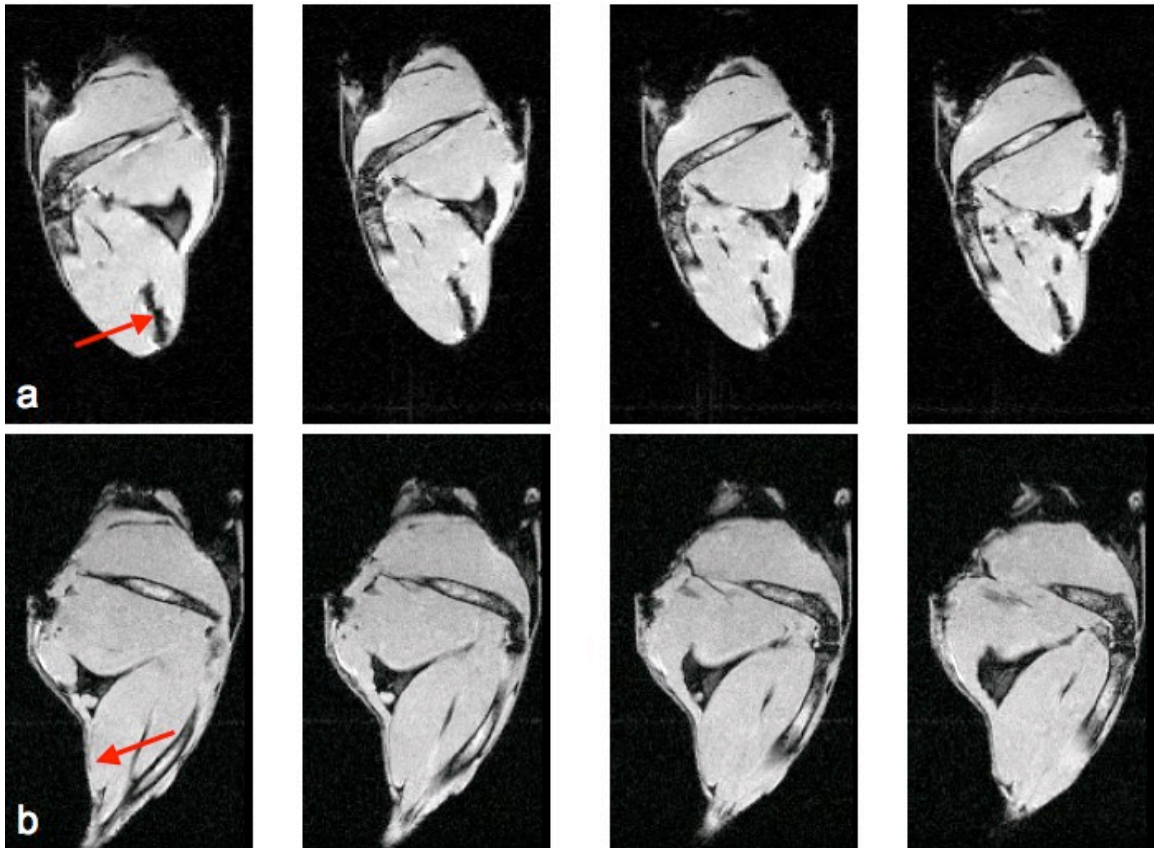


**Figure 6.11—3D GRE imaging of MPIO-labeled cells following *ex vivo* implantation within the soleus muscle of the mouse rear hind limb. (a) 4 consecutive slices of a mouse rear hind-limb injected with 1x10^{6} labeled cells; (b) 4 consecutive slices of a control mouse rear hind-limb injected with 1x10^{6} unlabeled cells. MPIO labeling results in a distinct signal void (arrow) not present when unlabeled cells are injected. (TE/TR = 2.19/25 ms; flip angle = 12°; resolution = 125x117x250 $\mu$m$^3$)**

Figure 6.12a shows a representative image of staining throughout the pellet for unlabeled control cells. The presence of red-pink staining indicates GAG production, which is further demonstrated via higher magnification (Figure 6.12b). However, in the case of MPIO-labeled cells, while pellet formation did occur during the 4-week chondro-

differentiation procedure, the presence of aggregated iron throughout the pellet hinders

ECM visualization (Figure 6.12c). Higher magnification examination (Figure 6.12d)

reveals traces of positive GAG staining (arrows).
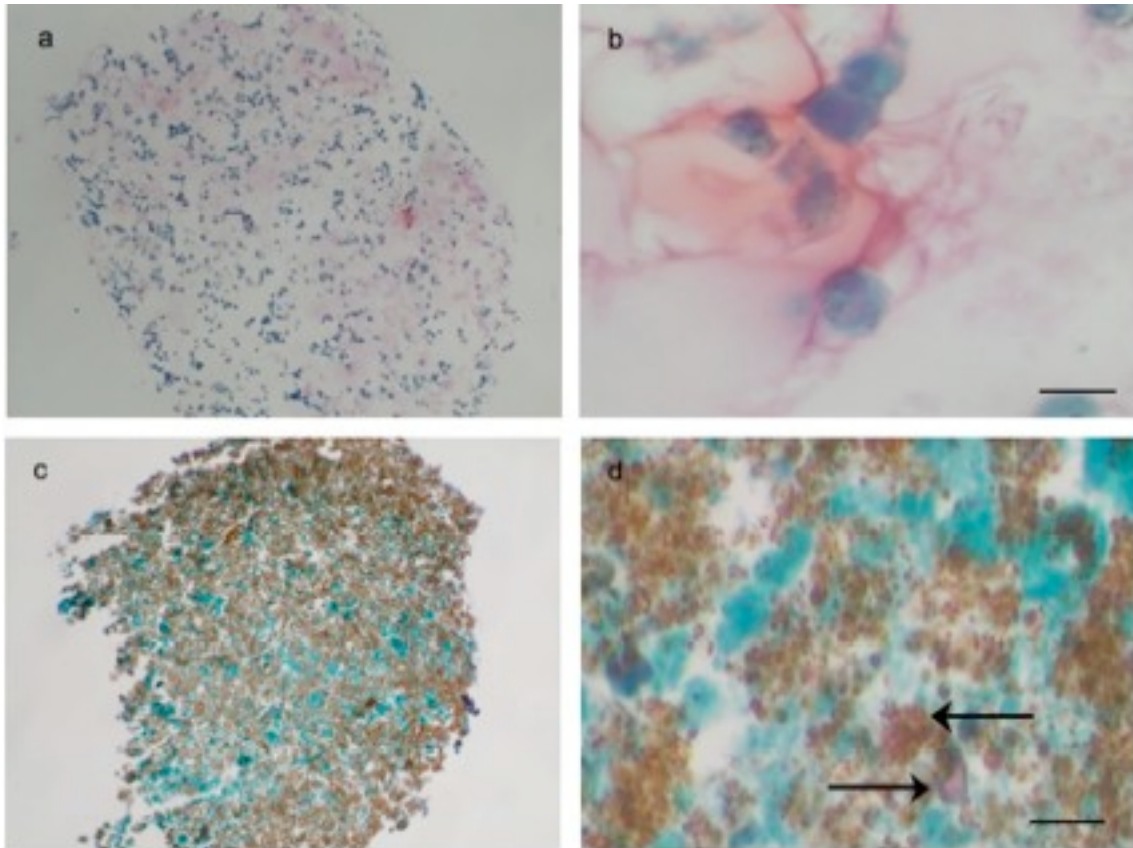


**Figure 6.12—Chondro-differentiation of MPIO-labeled rMSCs. H&E and safranin-O/fast green dye combination stains GAG red-pink, nuclei blue-purple, and the cytoplasm green. (a) unlabeled cells showing positive GAG staining (pink/red) throughout the pellet; (b) high magnification section of unlabeled cell pellet demonstrating positive GAG staining; (c) MPIO-labeled cells showing considerable aggregation of iron throughout the pellet which hinders visualization of the ECM; (d) high magnification section of labeled cell pellet. While labeled sections demonstrate traces of positive GAG staining (black arrows), iron aggregates are most apparent. (Scale bar = 20 μm)**

In addition, quantitative assessment of proteoglycan production using a DMMB assay

shows no significant difference (p<0.05) in GAG content per pellet (Figure 6.13) between

MPIO-labeled cells and unlabeled cell pellets following *in vitro* chondrogenesis.
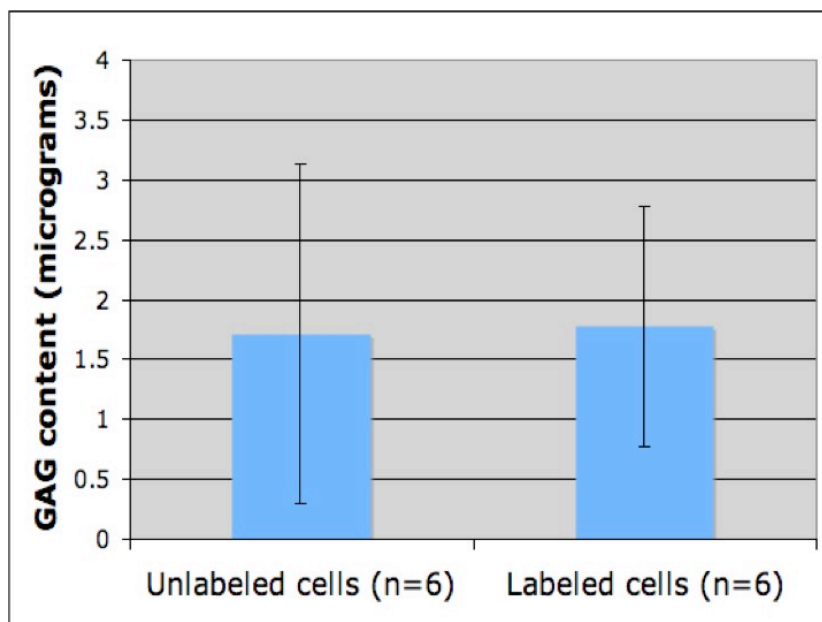
**Figure 6.13—Quantitative analysis of MPIO-labeled rMSC chondrogenesis. Results of DMMB assay to determine GAG content in labeled and unlabeled cell pellets. No significant difference was found between labeled and unlabeled cells (p<0.05). (Data is presented as mean±standard deviation for n=6 samples)**

### 6.3.5  Excess Iron Analysis

To determine whether excess unincorporated iron oxide particles were present following the labeling procedure and PBS washing, fluorescence imaging of co-labeled cells was performed (Figure 6.14). A representative image of MPIO-labeled rMSCs that were Hoechst labeled in order to stain the nucleus is shown in Figure 6.14b. While the images shows MPIO particles associated with cells (surrounding the nucleus), there also appears to be excess iron particles not associated with cells. The presence of excess iron oxide particles following PBS washing is further demonstrated in Figure 6.14c, which shows a region of iron oxide particles without the presence of cells.
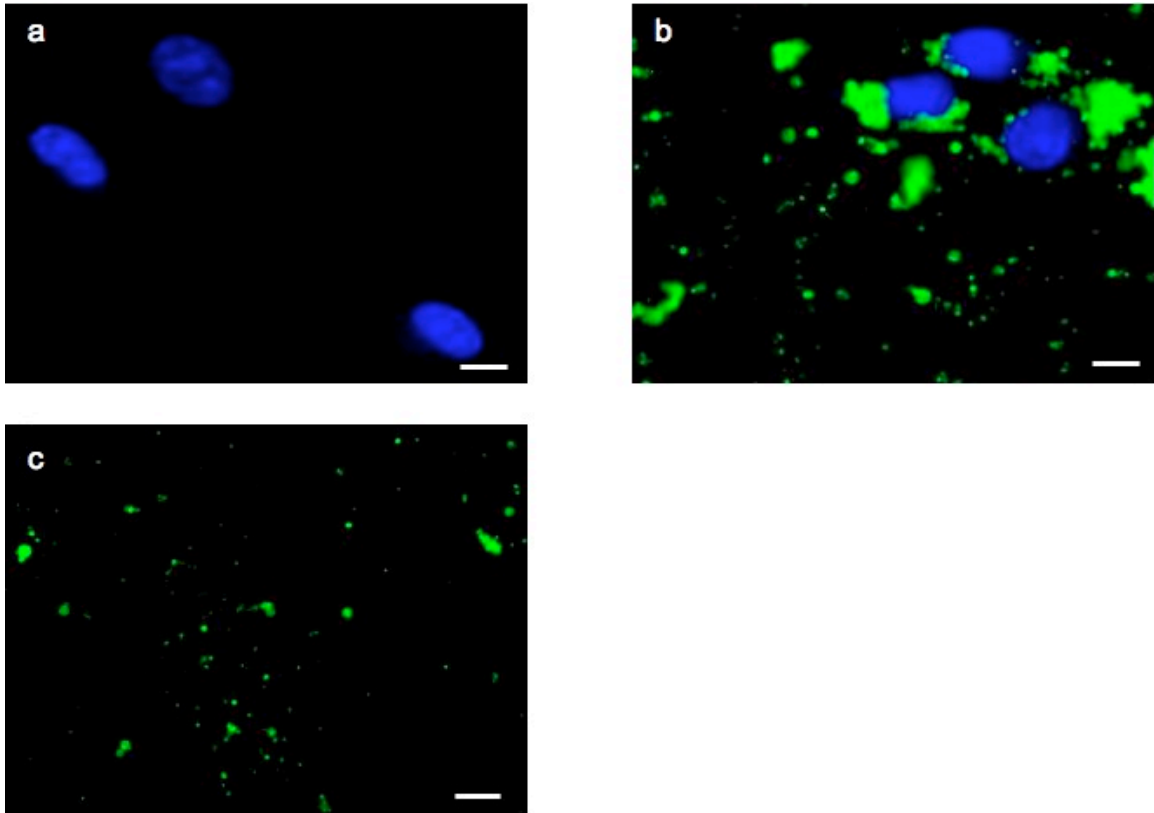
**Figure 6.14—Fluorescence microscopy of MPIO labeling and Hoechst staining of rMSCs. (a) unlabeled cells stained with Hoechst; (b) MPIO-labeled cells stained with Hoechst as well as excess particles not associated with cells (bottom left of image); (c) region of culture slide containing MPIO particles without the presence of cells. The fluorescence associated with residual iron oxide particles indicates that PBS washing alone does not completely remove contrast agent that is not taken up by cells during the labeling procedure. (Scale bar = 20 μm)**

## 6.4    Discussion

The promise of stem cell-based tissue engineering is enhanced considerably with an effective minimally invasive method for assessment following implantation. MRI is non-invasive, capable of *in vivo* assessment, and able to allow for longitudinal imaging at successive time points. MPIO labeling of stem cells results in a hypo-intense region that can be distinguished on the corresponding MR image. While MR tracking of MPIO-labeled cells has been investigated previously, application to tissue engineering of the musculoskeletal system has not been examined to date. In particular, the application to

regeneration of articular cartilage has not been investigated. Application of this technique to the regeneration of cartilage and other tissues of the musculoskeletal system is important because the ability to track implanted MSCs within the body would be valuable as a means of non-invasively monitoring the repair and regeneration process. This ultimately allows for a method to assess the effectiveness of such treatment plans. As demonstrated by this study, MPIO labeling and tracking of cells using MRI has promise as a means for studying stem cell regeneration of articular cartilage specifically, as well as other parts of the musculoskeletal system.

The *in vitro* results show efficient rMSC uptake of MPIOs, along with the associated hypo-intense region, and corresponding loss in SI using both GRE and SE imaging. The SI loss resulting from labeling of rMSCs is strongest on GRE images (Figures, 6.1, 6.3, 6.4, and 6.6), which is to be expected since GRE sequences are highly sensitive to susceptibility differences between tissues. Loading of cells with MPIOs creates a large field inhomogeneity resulting in rapid SI loss. While SE sequences are intended to minimize the effect of susceptibility differences through the use of a 180° refocusing pulse, because of water proton diffusion prior to and following refocusing, SI loss can still be clearly visualized using these sequences as well.

While 3T imaging demonstrates the ability to track populations of MPIO-labeled cells, 14T imaging with near cellular resolution provides the potential to image single cells or small clusters of cells. GRE imaging at 14T (Figure 6.4) shows that at a concentration of $5 \times 10^5$ cells/mL MPIO labeling appears to result in saturation of signal loss in which the entire sample appears dark. At the lower concentration ($5 \times 10^4$ cells/mL), it is possible to make out the labeled cells as distinct signal voids within the

background signal associated with the hydrogel. The apparent saturation of signal loss at 14T associated with labeling is also apparent using SE imaging (Figure 6.5) for the higher concentration of cells, although as expected it is not as severe as images obtained using GRE imaging. The quantitative analysis of the images obtained at 14T appears to support these results (Figure 6.6). For GRE imaging of $5x10^5$ cells/mL the signal loss at the center of the line profile is the strongest and does not rapidly return to background values with increased distance from the center. This is likely because the SI at a given point in the line profile is influenced not only by the associated particles at the center of the line profile but other particles in the immediate environment resulting from the high density of labeled cells throughout the tube. When the concentration is reduced to $5x10^4$ cells/mL the SI loss at the center of the line profile is less pronounced compared to the higher concentration of cells, and the return to background intensity values with increased distance from the center is clear. Although SE imaging demonstrates an overall weaker effect from MPIO labeling, a similar trend holds with a more rapid return to background intensity values for the lower concentration of labeled cells.

MPIOs have been used to label a variety of cells including CD34^{+} cells (100), hepatocytes (102), fibroblasts (102), neural progenitors (103), macrophages (104), and T-cells (105). Owing to their larger size, MPIOs have several advantages over conventional nanometer-sized iron oxide particles. First, the use of nanometer-sized iron oxide particles requires millions of particles per cell for MR detection, necessitating highly efficient labeling techniques that often include the use of a transfection agent to label MSCs (46,95). In this study, cells were labeled with close to 90% efficiency without the use of a transfection agent. This efficiency is similar to results by Hinds *et al*. (100) who

report 100% labeling efficiency of MSCs and 90% for non-adherent cells. One issue in labeling cells with iron oxides is determining whether the particles are internalized by the cells or only attached to the surface of the cell; surface attachment is undesirable because of its transient nature. This study utilized confocal microscopy to verify internalization of the MPIO particles. In addition, using a similar labeling procedure, Hinds *et al.* (100) demonstrated internalization of MPIOs into cellular endosomes using the marker CM-DiI. Another advantage of this methodology is that the large particle size of MPIOs also inherently reduces the number particles per cell needed for detection while still maintaining similar iron load. This will likely facilitate clinical imaging of smaller populations of transplanted cells. While 3T imaging in this study was used to detect populations of labeled cells, the 14T imaging results demonstrate the ability to detect very few cells with the potential for single cell imaging. Lastly, given that multiple cell divisions cause rapid dilution of iron within each cell (56), the ability to track fewer particles has the potential to facilitate detection of labeled cells for longer time periods.

This study examined for the first time, the ability to longitudinally track MPIO-labeled MSCs *in vitro.* Based on the MR imaging results, it is possible to detect labeled cells throughout a 6-week time period. In addition, DIC imaging confirmed the presence of MPIO particles throughout the time course. Immediately following labeling, there was an abundance of particles internalized by the cells. Over time, as cell division occurs, the number of particles within the cell is diluted, and ultimately is the determining factor in the ability to track cells longitudinally. A major consideration in the use of iron oxide particles for stem cell tracking is the length of time that cells can be monitored, and how quickly the iron oxide concentration is diluted out within the cell. Delo *et al.*

demonstrated the ability to track MPIO-labeled stem cells *in vivo* within the heart for up to 4 weeks post injection (106). While the present study demonstrated tracking for a longer period of time, future investigations should investigate the ability to longitudinally track MSCs *in vivo*. Ultimately, the length of time needed will likely depend on the particular therapeutic application of interest. Finally, it is also important to consider the eventual fate of MPIO particles, such as their potential release from cells over time. For example, Amsalem *et al*. have reported macrophage uptake of iron oxide particles released by cells following implantation into an infracted myocardium rat model (107). This is a concern as it could lead to an incorrect MR-based assessment of the ability to specifically track implanted cells.

MPIO-rMSCs were also detected *ex vivo* within a bovine osteochondral defect model, as well as within the soleus muscle of a mouse hind limb. In both cases labeled cells could be distinguished from the surrounding tissue. This is the first demonstration of MPIO-labeled cell detection within articular cartilage. Jing *et al*. have demonstrated *in vivo* imaging of cells labeled with conventional iron oxide particles for up to 12 weeks (108). In this case the labeling was performed using a Fe-Pro complex, and a rabbit osteochondral defect was used for implantation. In the present study, a bovine knee was chosen based on the thickness of the cartilage, which makes visualization easier than in the rabbit knee where cartilage thickness is approximately 200 μm.

Prior to implantation, labeled cells were encapsulated within a Puramatrix hydrogel scaffold. Implanted MSC populations require a scaffold to promote cell adherence, proliferation, and differentiation (3). For MR tracking it is important to consider the signal characteristics of the scaffold and ensure that they do not interfere with detection

of the labeled cells themselves. Among a wide variety of synthetic polymers, the use of hydrogels as 3D scaffolds for cell implantation has been well documented (86). The Puramatrix hydrogel used in this study is commercially available and has been shown to support growth and differentiation of MSCs (13,14,109). The polymerization characteristics of Puramatrix allow implantation of the hydrogel in liquid form and then formation of the gel upon exposure to *in vivo* physiological conditions. For *in vitro* culture, polymerization occurs upon exposure to normal cell culture media, which was used for gel formation in this study. As shown in Figure 6.4, one potential issue to consider is the formation of bubbles during polymerization of the hydrogel, which leads to a signal void on MR images; this signal void could potentially be mistaken as labeled cells. However, this potential issue can be overcome by using various techniques such as de-gasing to remove the presence of bubbles following polymerization. Based on the results presented here, encapsulation within Puramatrix does not appear to inhibit MR detection of MPIO-labeled rMSCs. Detection of MPIO-labeled cells within Puramatrix hydrogels has not been reported to date, although previous work has demonstrated MR detection of Fe-Pro labeled cells within PEG hydrogels (95), as well as MR detection of iron oxide-labeled cells within collagen-based gel scaffolds using 11.7T MRI (110).

In this study, $T_{1\rho}$ imaging of labeled cells implanted within an osteochondral defect was also performed. $T_{1\rho}$ describes longitudinal relaxation in the rotating frame and is sensitive to spin-lattice energy exchange between water and large molecules such as those present within the ECM of articular cartilage. Disruption of proteoglycan content within the cartilage matrix is known to cause an elevation in $T_{1\rho}$ resulting from increased water molecule motion (96-98). The results indicate strongly elevated $T_{1\rho}$ values for the

region corresponding to the constructs for both unlabeled and MPIO-labeled cells, likely due to the extremely high water content of the hydrogels and associated water molecule motion. It is important to consider the effect that labeling will have on MRI-based functional assessment techniques. As an example, ideally iron oxide labeling should allow for tracking of cell bio-distribution but should not inhibit $T_{1\rho}$ imaging, which can be used to evaluate the integrity of the newly formed tissue and the surrounding cartilage. From this study, immediately following encapsulation and implantation, $T_{1\rho}$ imaging appears to be dominated by the high water content of the hydrogel, independent of labeling. However, over time, as implanted cells differentiate and produce ECM, the effect on $T_{1\rho}$ imaging remains to be seen, including any potential effects of iron oxide labeling. While $T_2$ imaging is also often used to analyze cartilage (111), in this study it was not utilized because of the strong sensitivity of $T_2$ to the presence of iron oxides.

Previously, there has been controversy about the effect of iron oxide labeling on MSC chondrogenesis. Kostura *et al.* using poly-L-lysine-coated Feridex reported inhibition of chondrogenesis mediated by the presence of the iron oxide (112). Given the considerable differences in particle size, iron content, and transfection agent requirements of MPIOs compared to conventional nanometer-sized iron oxide particles, this study investigated MPIO labeling effects on MSC chondrogenesis. The results indicate that MPIO-labeling does not quantitatively inhibit GAG production, but extracellular iron aggregation limits visualization of the ECM. This limits the ability to use conventional staining techniques to examine proteoglycan production and qualitatively assess chondrogenic differentiation. The source of the aggregated iron is possibly a result of the excess MPIOs present following the labeling procedure and PBS washing. During

chondrogenesis, aggregation of these excess particles is likely promoted by the use of centrifugation to initiate formation of a cell pellet and remains aggregated within the pellet throughout the chondro-differentiation procedure. As such, the aggregation of excess particles may be further exacerbated by the particular method of *in vitro* chondrogenesis performed here, and future studies should be aimed at using 3D culture (9) to promote differentiation of MPIO-labeled MSCs.

One limitation of this technique as demonstrated in this study is the presence of excess unincorporated MPIO particles following labeling and PBS washing Figure 6.14b-c). The labeling method utilized here is based on a procedure described by Hinds *et al*. used to label porcine MSCs (100) and consists of a similar iron concentration used for labeling. In contrast to the present study, Hinds *et al*. report the ability to sufficiently remove excess particles with PBS washing following the labeling procedure. However, Tang *et al*. report the presence of excess MPIO particles following labeling of blood monocytes (57). The ability to successfully remove excess unincorporated particles is important because particles not associated with cells will result in improper localization of cells and limit the accuracy of this technique. As such, while MPIO labeling may provide several advantages over labeling with conventional nanometer-sized iron oxide particles, these potential benefits should be weighed against the proclivity for residual MPIOs to remain and aggregate following the labeling procedure. Future studies should investigate alternative washing methods, and other techniques for isolating labeled cells from excess MPIO particles not taken up during the labeling procedure. For example, the Dragon Green tag could be used to isolate labeled cells using fluorescence assisted cell sorting (FACS).

This study demonstrates the promise of MPIO labeling for monitoring cartilage generation, In addition, these studies highlight the potential use of this technique in the future development of stem cell-based tissue regeneration of the musculoskeletal system. Future studies aimed at ensuring the presence of only particles contained within cells, as well as longitudinal *in vivo* examination of MR tracking of MPIO-labeled MSCs throughout the tissue regeneration process will aid in the development of this methodology as a clinical tool for assessment of implanted stem cells.

## 6.5 <u>Acknowledgements</u>

# Chapter 7: Genetic Modification-based Iron Loading Studies

## 7.1   <u>Introduction</u>

In addition to labeling cells with iron oxide-based contrast agents in order to detect them using MRI, there has also been research focused on genetically modifying cells in order to increase their uptake take of iron. Compared to the use of contrast agents, genetic modification techniques have several potential advantages that make them attractive for MR-based cell tracking. First, genetic techniques remove the need to load cells with SPIOs prior to implantation into the body; cells over-expressing the gene of interest can potentially uptake endogenous iron (68). This ability also makes it possible for cells stably expressing the gene of interest to longitudinally take up iron within the body. In contrast, loading cells with SPIOs prior to implantation inherently limits the length of time that cells can be detected based on particle dilution resulting from cell division. In addition, Zurkiya *et al*. have demonstrated the ability to clone a gene relevant for MR-based cell tracking into a doxycycline inducible lentiviral vector (68). Using this model it is possible to maintain precise control over expression of the gene of interest. As such, the gene of interest can be maintained in an off state, and turned on with doxycycline administration prior to MR imaging. Lastly, while the presence of iron oxides does not necessarily mean that implanted cells are alive and viable, detection of iron based on genetic modification of cells increases the likelihood that detection of SI loss on MR images would correspond to live cells actively expressing proteins.

The first set of studies examining the ability to use genetic modification as a means to generate MR-based contrast is focused on expression of the magA gene present within MTB. In particular these studies examined the magA gene from two different strains of

MTB, the AMB-1 and MS-1 strain. Based on results from Zurkiya *et al*. (68) and Goldhawk *et al*. (69), the present study focuses on replicating these results by investigating the ability to stably express these genes in mammalian cells and whether their expression leads to increased iron uptake and detection via MRI. The second set of studies is focused on over-expressing the ferritin gene in mammalian cells in order to increase uptake of iron and promote subsequent MR-based detection. In particular these studies separately examined expression of both the FTH and FTL subunit of ferritin.

## 7.2    Materials and Methods

### 7.2.1    Molecular Biology
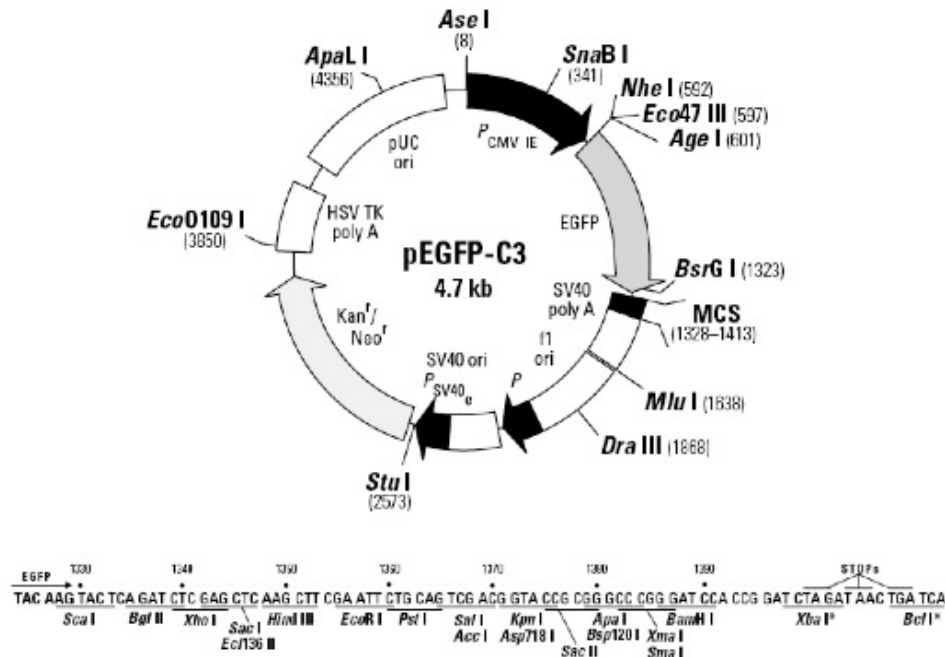


**Figure 7.1—Plasmid vector map for pEGFP-C3 showing the location of the gene insert, flanking restriction enzymes, the EGFP fusion protein, as well as the sites of drug resistance. (Image obtained from www.clonetech.com)**

The magA genes from the AMB-1 and MS-1 MTB strains were provided by Dr. James Onuffer and Dr. Wendell Lim (Cell Propulsion Lab, UCSF, San Francisco, CA, USA). The genes were provided as a cloned insert within pEGFP-C3 (Figure 7.1;

Clonetech, Mountain View, CA, USA) under control of the cytomegalovirus promoter. Of note, pEGFP-C3 is a fusion plasmid that links expression of the gene of interest, in this case magA, to expression of green fluorescent protein (GFP). In this way it is possible to confirm transfection of cells with the plasmid, and create high-expressing stable cell lines based on the use of GFP during FACS.

For ferritin-based experiments, both the FTH and FTL subunits were cloned into expression vectors. Human FTH and FTL sequences were ordered (Open Biosystems, Huntsville, AL, USA) using the appropriate accession number obtained from Genebank. Sense and anti-sense primers for amplification of the DNA were designed using A Plasmid Editor (Ape; M. Wayne Davis, Univ. Utah, Salt Lake City, USA) and Gene Designer (DNA 2.0, Menlo Park, CA, USA). In particular, Kozac sequences, and a start codon were added to each sense sequence. In addition, a BamHI restriction site was added to the 5' side of both the FTH and FTL sequences, while a NotI restriction site, and XbaI site were added to the 3' end of the FTH and FTL sequence respectively. The designed primers were obtained from Integrated DNA Technologies (IDT; Coralville, IA, USA) and were used to amplify the FTH and FTL sequences via PCR (C1000 Thermal Cycler, Bio-Rad, Hercules, CA, USA) using settings provided by the manufacturer. Following PCR, the DNA was purified using a 1% agarose gel, and extracted using a QIAquick Gel Extraction Kit (Qiagen, Venlo, Netherlands).

The amplified FTH and FTL sequences were separately cloned into pCR 4Blunt-TOPO vectors using the Zero Blunt TOPO PCR Cloning Kit (Invitrogen). Cloning was performed according to the manufacturer's protocol, and vectors containing either the FTH or FTL insert were separately transformed into chemically competent *E. coli* cells.
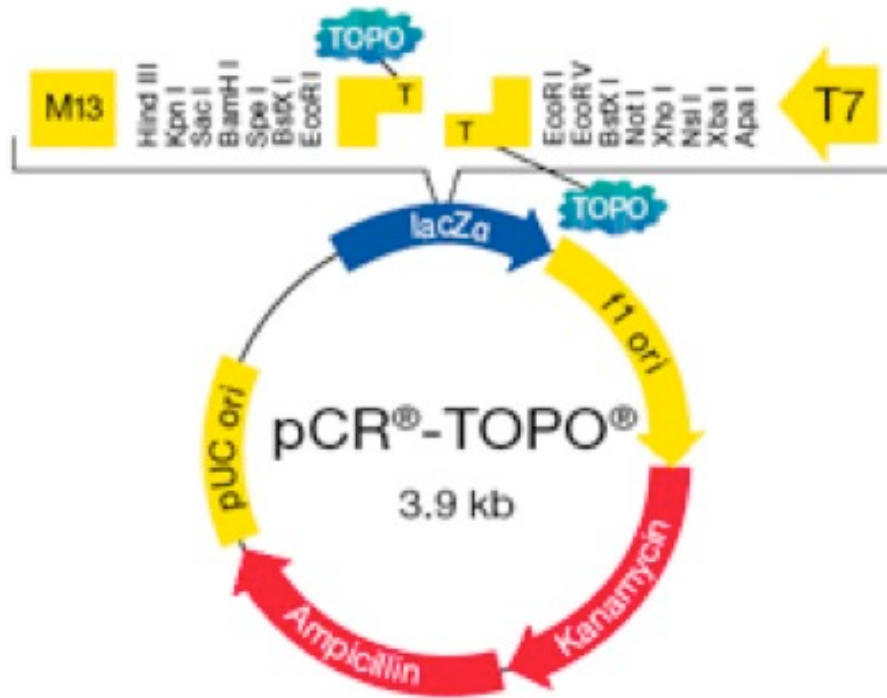
**Figure 7.2—Plasmid vector map for pCR TOPO showing the location of the gene insert, flanking restriction enzymes, promoters for sequencing, as well as the sites of drug resistance. (Image obtained from www.invitrogen.com)**

Figure 7.2 shows the restriction map for pCR TOPO, which highlights the location of the gene sequence, flanking restriction enzymes sites, promoters for sequencing, as well as the sites of drug resistance to Ampicillin and Kanamycin. Following the manufacturer's instructions, cells were seeded on agar-plates containing Ampicillin in order to select for transformed (drug resistant) cells. Furthermore, a blue-white screen was used in order to identify transformed colonies successfully containing either the FTH or FTL insert. As such, the agar-plates contained X-gal (Invitrogen), which allows for identification of colonies containing the gene insert (white) versus colonies that contain only the vector backbone without the insert (blue). Following overnight culture of the plated cells, white colonies were selected from each of the FTH and FTL plates and cultured overnight in lysogeny broth (LB) containing Ampicillin. The following day, DNA was isolated from

the bacterial cells using a QIAprep Spin Miniprep Kit (Qiagen), and sequenced (IDT) in order to verify successful gene insertion into the plasmid backbone.

Plasmid vectors containing either the FTH or FTL insert were digested using the appropriate restriction enzymes (BamHI/NotI for FTH, and BamHI/XbaI for FTL) according to the suggested protocol from New England BioLabs (Ipswich, MA, USA). In addition, the pcDNA 3.1+ backbone expression vector (Invitrogen) was also digested using the same restriction enzyme combination used for either FTH or FTL. Figure 7.3 shows the restriction map for pcDNA 3.1+/-, highlighting the location of the restriction enzyme sites for insertion of the gene of interest, as well as the Ampicillin and Neomycin drug resistance sites. Of note, this plasmid is under control of the cytomegalovirus promoter.

Cloning was performed according to the manufacturer's protocol, and vectors containing either the FTH or FTL insert were separately transformed into chemically competent *E. coli* cells. Following the manufacturer's instructions, cells were seeded on agar-plates containing Ampicillin in order to select for transformed (drug resistant) cells. Following overnight culture of the plated cells, colonies were selected from each of the FTH and FTL plates and cultured overnight in lysogeny broth (LB) containing Ampicillin. The following day DNA was isolated from bacterial cells using a QIAprep Spin Miniprep Kit (Qiagen), and sequenced (IDT) in order to verify successful gene insertion into the pcDNA 3.1+ plasmid backbone.
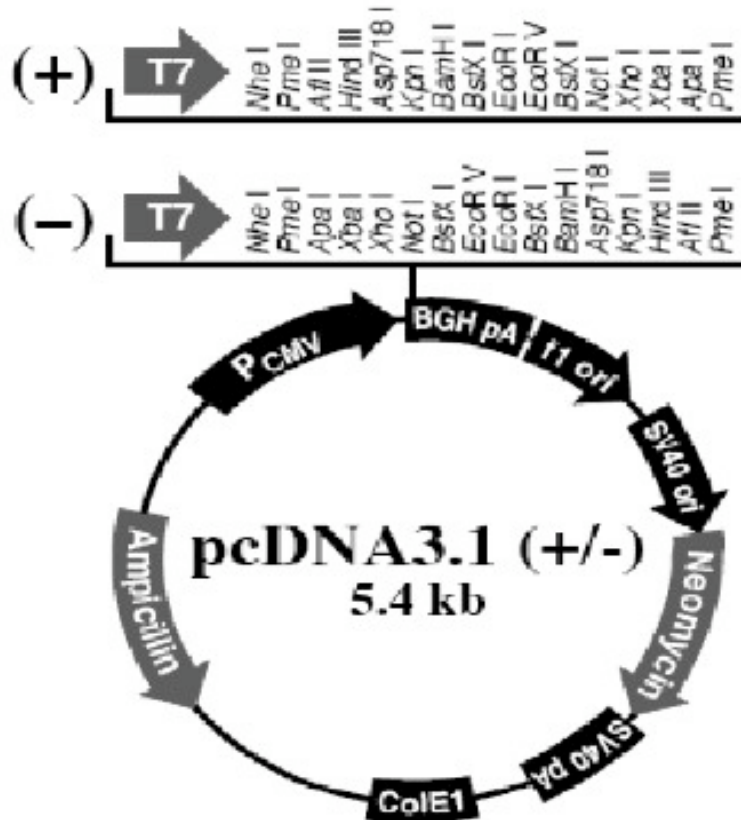
**Figure 7.3—Plasmid vector map for pcDNA 3.1+/- showing the location of the restriction enzyme site for gene insertion, as well as the sites of drug resistance. (Image obtained from www.invitrogen.com)**

### 7.2.2   Cell Culture and Transfection

All transfection experiments were performed using HEK 293 cells obtained from the American Type Culture Collection (ATCC; Manassas, VA, USA). Cells were cultured in 75 cm$^2$ tissue culture flasks containing standard tissue culture media: high glucose DMEM (Invitrogen) with 10% FBS and 1% penicillin/streptomycin. Cells were maintained under standard conditions (37°C and 5% CO$_2$), and passaged 1:10 at 80-90% confluence. Cells were sub-cultivated using 0.25% trypsin with 1 mM EDTA. Gene transfection experiments using 293 cells were performed separately for the bacterial magA gene and the mammalian ferritin genes.

Transfection of 293 cells with the pEGFP-C3 vector containing the magA gene from either the AMB-1 or MS-1 strain was performed using Lipofectamine LTX (Invitrogen) according to the manufacturer's instructions. Amounts of each reagent in the transfection solution were determined based on the size of the culture dish used for cell experiments and the table provided in the manufacturer's instructions. Briefly, the day before transfection, 293 cells were reseeded at 50% confluence in order to ensure that the cells would not become confluent during the 48-hour transfection period. The following day plasmid DNA was diluted in Opti-MEM I Reduced Serum Medium (Invitrogen) and mixed thoroughly. Next, Lipofectamine LTX was added to the solution, mixed thoroughly, and incubated for 30 minutes at room temperature. Of note, pMAX GFP (Lonza) was used a positive control to validate the transfection procedure, and untransfected cells were utilized as a negative control.

Transfection of 293 cells with the pcDNA 3.1+ vector containing either the FTH or FTL gene was performed using Lipofectamine LTX according to the manufacturer's instructions. Amounts of each reagent in the transfection solution were determined based on the size of the culture dish used for cell experiments and the table provided in the manufacturer's instructions. Briefly, the day before transfection, 293 cells were reseeded at 50% confluence in order to ensure that the cells would not become confluent during the 48-hour transfection period. The following day, the plasmid DNA was diluted in Opti-MEM I Reduced Serum Medium (Invitrogen) and mixed thoroughly. Next, Lipofectamine LTX was added to the solution, mixed thoroughly, and incubated for 30 minutes at room temperature. Of note, pMAX GFP was used as a positive control to

110

validate the transfection procedure, and untransfected cells were utilized as a negative control.

### 7.2.3  *Fluorescence Microscopy and Transfection Efficiency*

Two days after transfection and prior to iron feeding, cells were imaged via fluorescence microscopy using a Nikon Eclipse Ti microscope with a 488 nm excitation wavelength and a 30 nm pass-band centered at 515 nm (green). Images were acquired as green fluorescence overlaid on a bright field image. Cells were imaged within the dishes used for culture, and pMAX transfected cells were imaged as a positive control, while untransfected cells were imaged as a negative control.

A Guava easyCyte 8HT flow cytometry system (Millipore, Billerica, MA, USA) was used to determine the transfection efficiency of cells transfected with the magA gene from the AMB-1 or MS-1 bacterial strain. In addition, the Guava system was used to determine the percentage of 293 cells expressing the magA gene after generation of stable cell lines based on sorting with the EGFP present in the vector plasmid and drug selection. Cells were prepared by fixing using BD Cytofix Fixation Buffer (BD Biosciences) according to the manufacturer's instruction. After fixation, cells were resuspended in PBS containing 0.1% bovine serum albumin (BSA). Untransfected cells were used to setup the forward and side scatter, and the parameters conserved for all samples run. Data obtained from the system was analyzed using Flojo Cytometry Analysis Software (Treestar Inc., Ashland, Oregon, USA) in order to determine efficiency immediately after transfection, as well as after creation of stable cell lines.

### 7.2.4  *FACS and Stable Cell Line Generation*

Stable magA expressing cell lines were created using transfected 293 cells for both the AMB-1 and MS-1 strain. Following the 48-hour transfection period, cells were trypsinized, collected, and resuspended in PBS at a concentration of $1 \times 10^7$ cells/mL. FACS analysis was performed on the cell samples (using the GFP fusion protein) in order to isolate the top 10% of cells as well as the middle 50% of cells expressing the magA gene; this was done for both the AMB-1 and the MS-1 strain. FACS was performed at the UCSF Laboratory for Cell Analysis (San Francisco, CA, USA) using a BD FACSAria IIu system (BD Biosciences) equipped with an excitation laser and detection range of 515-545 nm. The forward and side scatter were set using untransfected 293 cells and the parameters conserved between all samples. One million cells from each sorted sample were seeded in 75 cm$^2$ tissue culture flasks containing media and allowed to attach overnight. The following day, Geneticin (G418; Invitrogen) was added to each flask at a concentration of 400 μg/mL, and cells were maintained under drug selection for the duration of cell culture.

### 7.2.5   Iron Feeding and Staining

For experiments with magA expressing 293s, cells were seeded on Poly-D-lysine (PDL) coated 35 mm glass bottom dishes (MatTek, Ashland, MA, USA) at 15% confluence; pMAX transfected cells and untransfected cells were also seeded on separate glass bottom dishes as controls. The following day after cells had attached to the PDL-coated glass surface, 250 μM ferric citrate was added to the cell culture media. Following 72-hour iron feeding, cells were washed three times with PBS to remove excess iron. Cells were then fixed in 10% neutral buffered formalin for 10 minutes. Following a PBS

rinse, cells were exposed to 0.5% Triton X-100 (Sigma) for 10 minutes in order to permeabilize the cell membrane.

For experiments with FTH and FTL expressing 293s, cells were seeded on 20 cm$^2$ plastic tissue culture dishes at 15% confluence; pMAX transfected cells and untransfected cells were also seeded on separate plastic tissue culture dishes as controls. The following day after cells had attached to the dishes, 250 μM or 1 mM ferric citrate was added to the cell culture media. Following 72-hour iron feeding, cells were washed three times with PBS to remove excess iron. Cells were then fixed in 10% neutral buffered formalin for 10 minutes. Following a PBS rinse, cells were exposed to 0.5% Triton X-100 for 10 minutes in order to permeabilize the cell membrane.

Staining for iron was performed using the Prussian Blue Iron Stain Kit (Polysciences, Warrington, PA, USA) according to the manufacturer's instructions. The stain was added directly to the tissue culture dishes containing fixed cells. Enhancement of the Prussian Blue stain was performed using the 3,3-Diaminobenzidine (DAB) Liquid Substrate System (Sigma) according to the manufacturer's instructions. DAB is oxidized by hydrogen peroxide in the presence of iron and results in a dark brown color that is often easier to detect than the conventional Prussian Blue stain. All samples for a single experiment were exposed to DAB for the same period of time in order to limit background staining issues.

### 7.2.6  MRI

All imaging was performed using a 600 MHz Varian scanner with a 10 mm broadband coil. Cells used for imaging were trypsinized, collected, and suspended at concentrations of $1x10^4$-$1x10^7$ cells/mL in 1.0 mL of Ficoll to prevent settling during

imaging. The suspensions were imaged in NMR tubes using the 10 mm coil, and all *in vitro* experiments were performed in duplicate. GEMS 2D imaging was performed using a TE/TR = 4.48-26.88/250 ms, and flip angle = 50°. SEMS 2D imaging was performed using a TE/TR = 16-90/1000 ms with a scan time of ~ 17 minutes. Both sequences were acquired with a slice thickness = 0.4 mm, FOV = 10 mm, and matrix size = 256x256, resulting in an in-plane resolution of 40 μm.

## 7.3    <u>Experimental Results</u>

### 7.3.1   *magA Gene Transfection and Stable Cell Lines*

Initial experiments focused on transfecting 293 cells with the pEGFP-C3 plasmid containing the AMB-1 or MS-1 magA strain. Based on the EGFP fusion protein, it is possible to visually assess transfection efficiency using fluorescence microscopy (Figure 7.4). 293 cells transfected with pMAX are shown as a positive control, while untransfected cells are depicted as a negative control. From the images it is possible to see that magA from both the AMB-1 strain and MS-1 were successfully transfected into 293 cells after 48 hours using Lipofectamine LTX. As expected, transfection efficiencies are not as high as the positive control (pMAX).

In order to quantify transfection efficiency of plasmids containing the magA gene from either the AMB-1 or MS-1 strain after 48 hours, cells were analyzed using flow cytometry. Transfection efficiency (Figure 7.5) of the magA gene from the AMB-1 strain in 293 cells after 48 hours was 33%. In the case of magA from the MS-1 strain, transfection efficiency was considerably higher with a value of 65%.
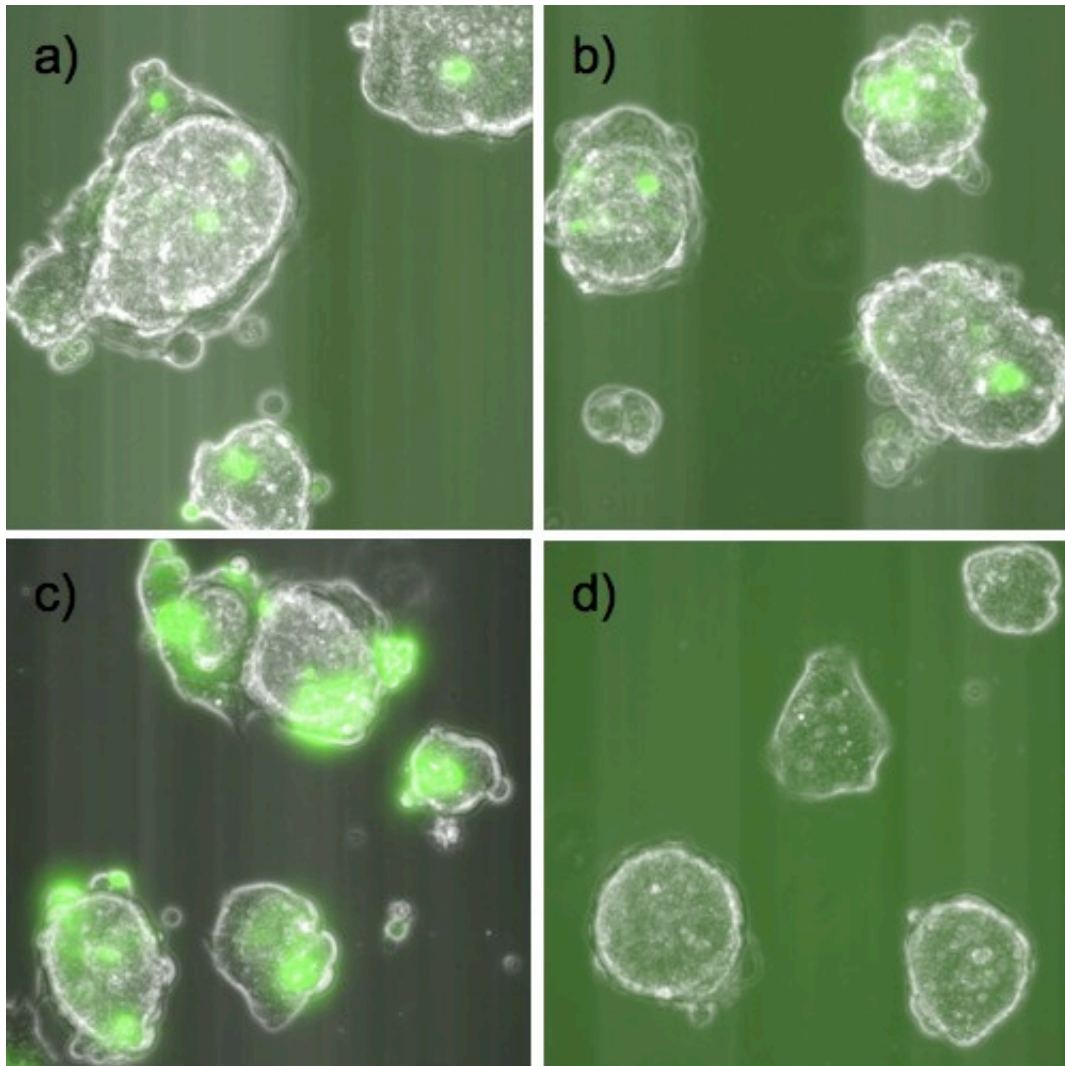
**Figure 7.4—Fluorescence microscopy of 293 cells 48 hours after transfection of magA using Lipofectamine LTX. (a) AMB-1 strain; (b) MS-1 strain; (c) pMAX (positive control); (d) untransfected cells (negative control). (Magnification = 20x)**

Figure 7.5 also shows histograms indicating the range of expression levels 48 hours after transfection. Based on the logarithmic scale, for AMB-1 the majority of cells appear to have expression levels ranging from $10^1$-$10^3$. In contrast, for MS-1, the distribution of expression levels is considerably narrower with a range from $10^1$-$10^2$. These expression levels are based on gating for forward and side scatter using untransfected control 293 cells.
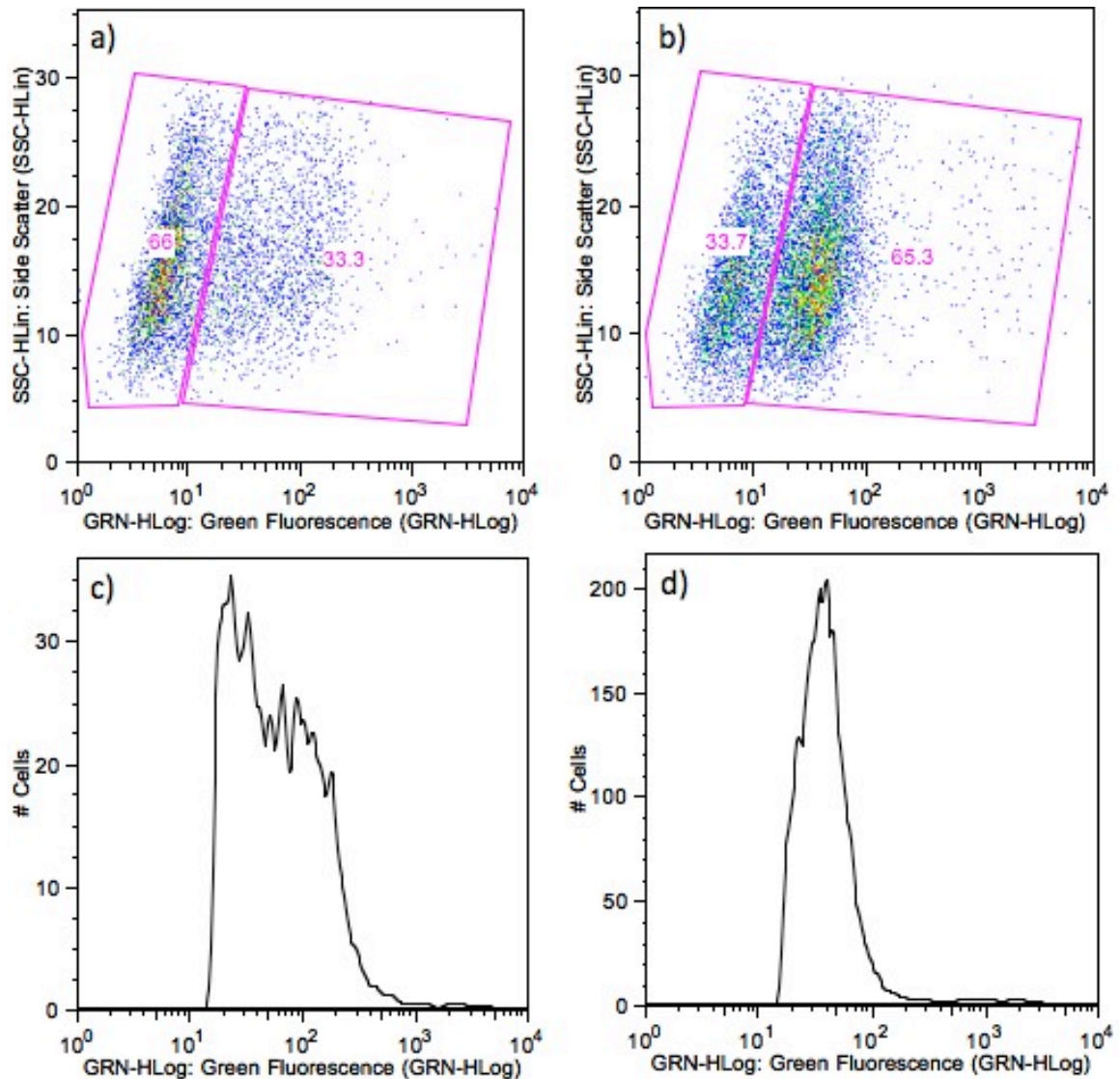
**Figure 7.5—Quantitative analysis of magA transfection efficiency. Plots show 33% transfection efficiency for the (a) AMB-1 strain; and 65% efficiency for the (b) MS-1 strain. Gating was performed using untransfected cells with a 1% positive threshold. Histograms showing expression levels on a logarithmic scale are shown for the (c) AMB-1 strain; (d) MS-1 strain.**

In separate experiments, 293 cells were transfected with either the AMB-1 or MS-1 strain of magA, sorted to isolate the top 10% and middle 50% of cells expressing the gene, and maintained under drug selection in order to create stable cell lines. Following this procedure, cells were analyzed to determine expression levels, and percentage of cells expressing the magA gene. For the MS-1 strain, sorting for the 10% of expression

116

levels, and maintaining the cells under drug selection increased expression in the stable

population to 79.6%. For the population based on the middle 50% sort, the expression

percentage was 71.9%. For the AMB-1 strain, the percentages were 97.4% for the

population based on the top 10% sort, and 94.8% for the population based on the middle

50% sort.
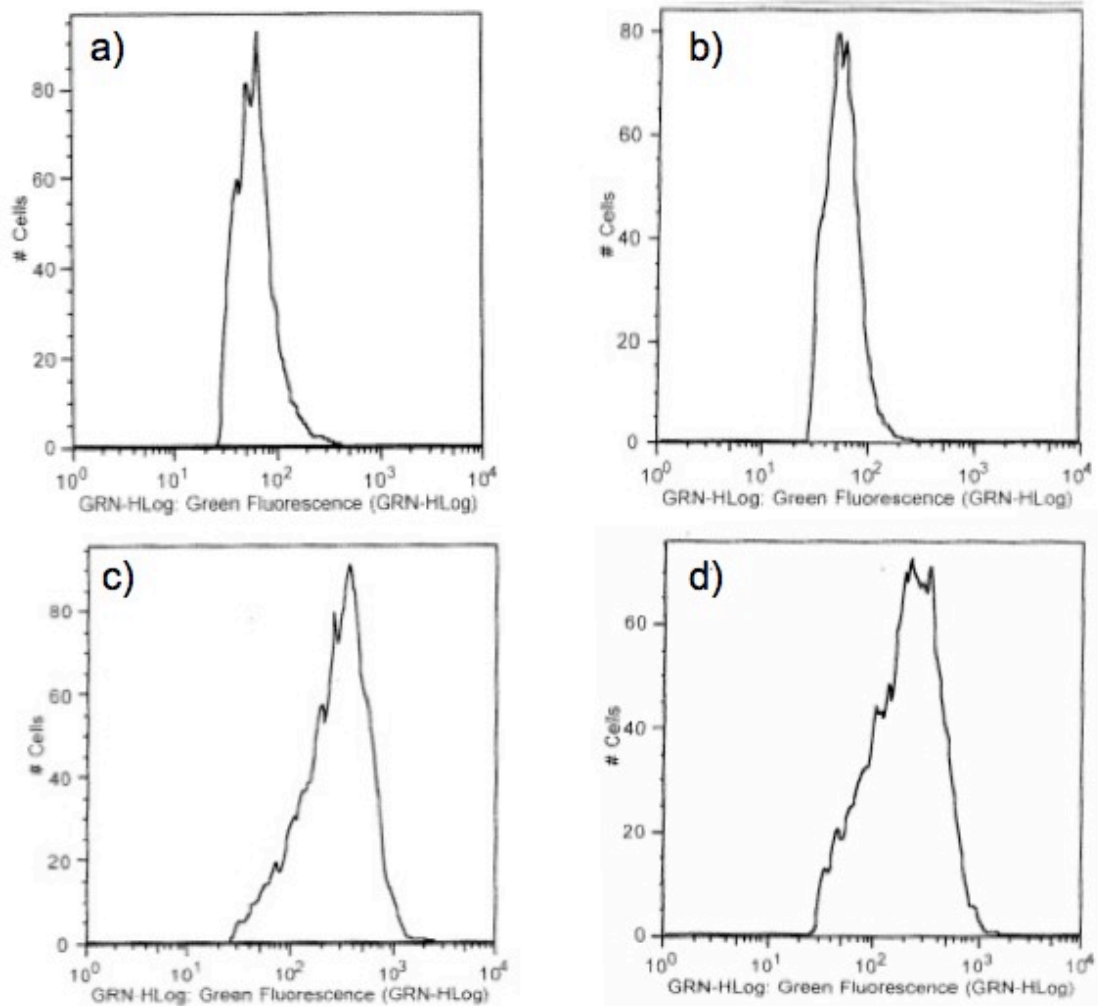


**Figure 7.6—Expression profiles for 293 stable cell lines. Plots show expression profiles for 293 cells expressing the magA gene following sorting for the top 10% and middle 50% and culture under drug selection. (a) MS-1 top 10%; (b) MS-1 middle 50%; (c) AMB-1 top 10%; (d) AMB-1 middle 50%. (Histograms show expression levels on a logarithmic scale)**

Figure 7.6 shows the expression profiles for the top 10% and middle 50% sorted

populations for both the MS-1 strain and the AMB-1 strain. From Figure 7.6, it is

apparent that the expression profile is considerably narrower for the MS-1 strain compared to the AMB-1 strain. This indicates a much larger range of expression levels in the cell population for the AMB-1 strain.

### 7.3.2 Histological Staining of magA Expressing Cells

Following transient transfection with the pEGFP-C3 vector containing the magA gene, and 72-hour feeding with 250 μM ferric citrate, Prussian Blue staining was performed to detect the presence of iron (Figure 7.7).
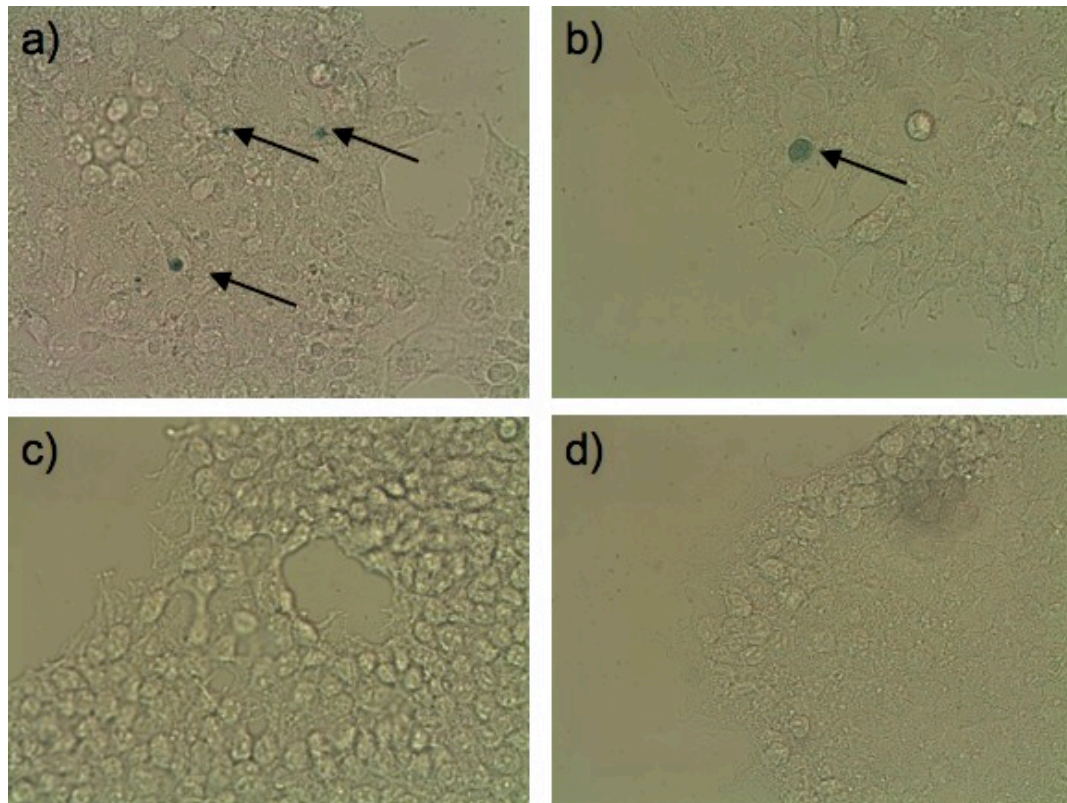


**Figure 7.7—Prussian Blue staining following transient magA transfection and 250 μM iron feeding. (a) MS-1 strain; (b) AMB-1 strain; (c) untransfected cells; (d) pMAX transfected cells. MS-1 and AMB-1 samples show distinct pockets of punctate blue staining (arrows), but overall do not show increased iron uptake associated with magA gene expression. (Magnification = 10x)**

Overall transient expression of magA from either the AMB-1 or MS-1 strain did not result in a marked increase in iron uptake as assessed by Prussian Blue staining. As

shown in Figure 7.7a-b the majority of cells did not demonstrate positive staining for Prussian Blue. While multiple distinct regions with punctate positive blue staining were discovered, one negative control sample also displayed a distinct blue region similar to the AMB-1 and MS-1 samples (not shown).
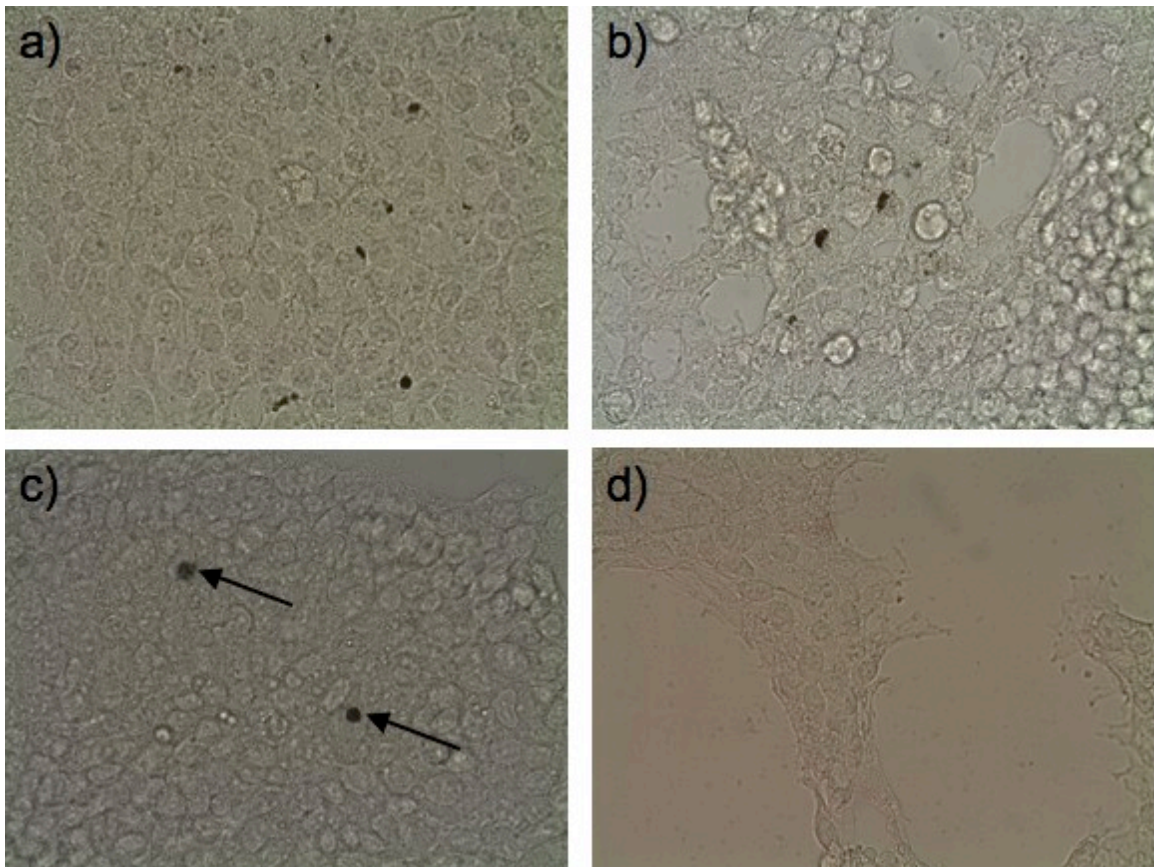


**Figure 7.8—DAB-enhanced Prussian Blue staining following transient magA transfection and 250 μM iron feeding. (a) MS-1 strain; (b) AMB-1 strain; (c) untransfected cells; (d) pMAX transfected cells. MS-1 and AMB-1 samples show distinct pockets of punctate brown staining but overall do not show increased iron uptake associated with magA gene expression. In addition, the negative control sample also has a distinct region of punctate brown staining (arrows). (Magnification = 10x)**

In order to further analyze iron uptake via histological staining, DAB enhancement of the Prussian Blue stain was also performed. Often, the brown color associated with DAB is more easily detectable than the light-blue color of the Prussian Blue stain. The DAB-enhanced staining results are shown in Figure 7.8, and further confirm the results

obtained from Prussian Blue staining alone. Overall, expression of the magA gene does not appear to increase uptake. While there are distinct regions of intense brown straining, in the AMB-1 and MS-1 samples, the majority of cells do not demonstrate positive staining. In addition, as shown in Figure 7.8c the negative control sample also shows two distinct regions of brown staining.
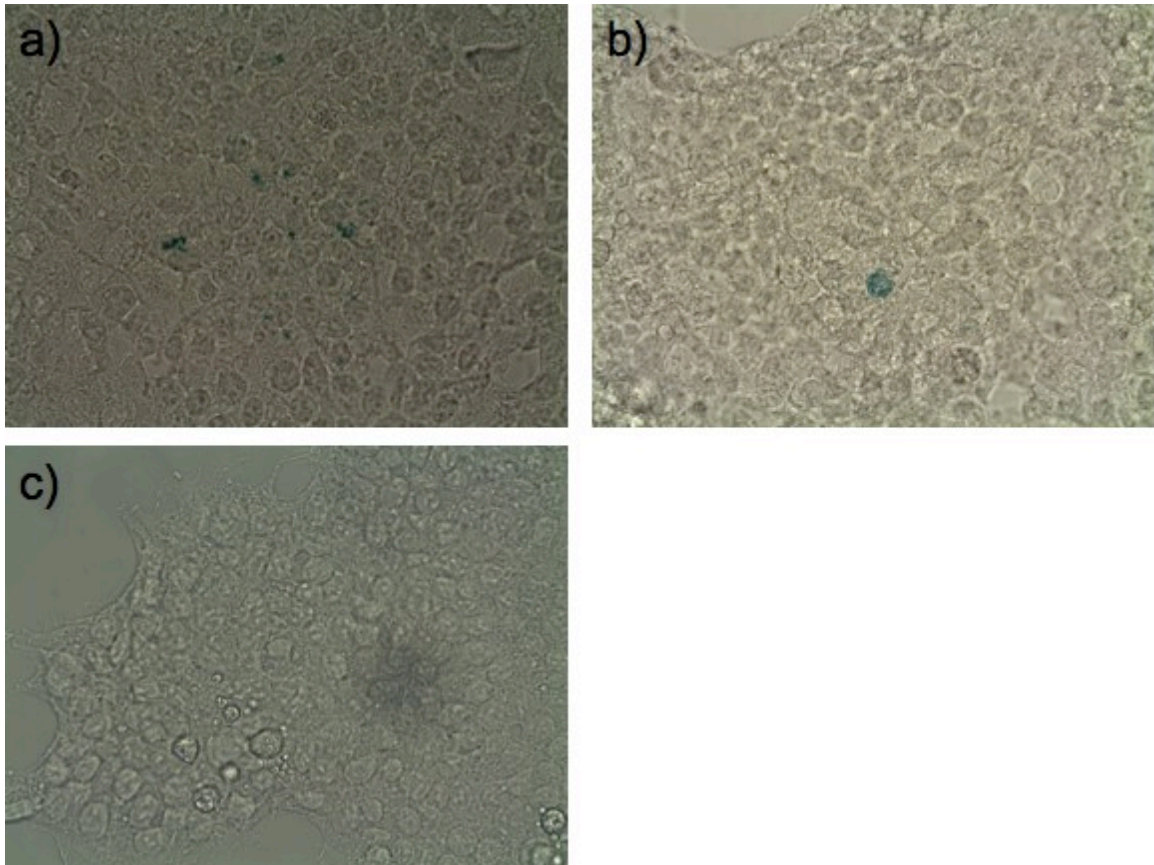


**Figure 7.9—Prussian Blue staining of stable cells expressing magA following 250 μM iron feeding. (a) MS-1 strain; (b) AMB-1 strain; (c) untransfected cells. MS-1 cells show increased pockets of staining compared to control cells but the majority of cells do not show increased iron uptake. AMB-1 cells do not show increased iron uptake compared to control cells. (Magnification = 10x)**

Prussian Blue staining, with and without DAB enhancement was performed on stable cell lines expressing magA from either the AMB-1 strain or the MS-1 strain after 72 hours of iron feeding. Figures 7.9 and 7.10 show the Prussian Blue staining and the DAB-enhanced results respectively for the top 10% cell populations derived from each strain.

In the case of magA from the AMB-1 strain, stable cells expressing the gene do not show any increased positive Prussian Blue staining (Figure 7.9b) compared to cells not expressing magA.
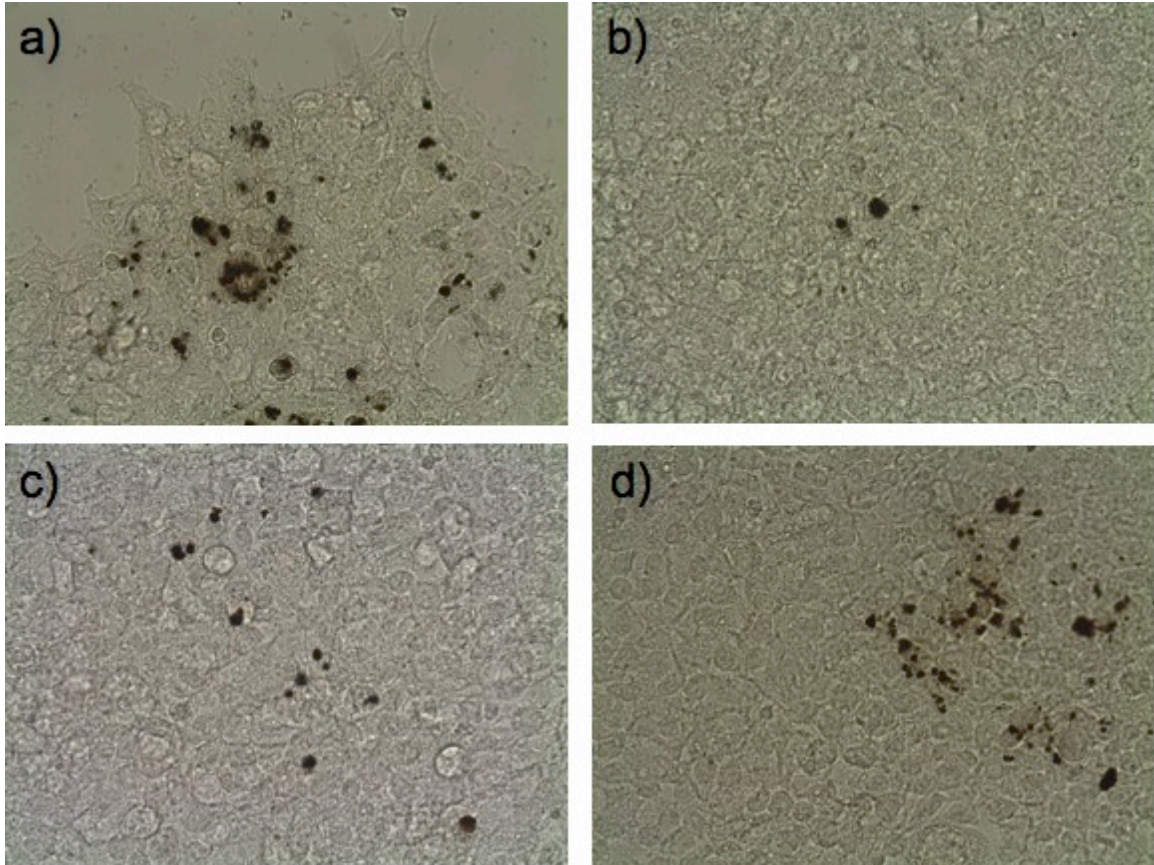


**Figure 7.10—DAB-enhanced Prussian Blue staining of stable cells expressing magA following 250 μM iron feeding. (a) MS-1 strain; (b) MS-1 strain; (c) AMB-1 strain; (d) negative control. MS-1 cells show regions of intense staining as well as regions with minimal staining. AMB-1 cells show limited pockets of staining. However, control cells also show regions of positive intense staining suggesting that magA expression does not contribute to increased iron uptake. (Magnification = 10x)**

In the case of the MS-1 strain, Prussian Blue staining did show increased positive staining (Figure 7.9a) compared to control cells, or cells transiently transfected with the magA gene from the MS-1 strain. However, overall the majority of stable cells did not show positive staining, indicating that magA expression predominately does not lead to increased iron uptake that can be detected via Prussian Blue. Results using DAB

enhancement (Figure 7.10) were similar to those found using Prussian Blue staining alone. Stable cells expressing magA from the AMB-1 strain did not show increased staining compared to control cells. Stable cells expressing magA from the MS-1 strain showed increased regions of intense brown staining within the tissue culture dish (Figure 7.10a). However, the majority of cells were not positively stained. Furthermore, control cells also had a region of significant punctate brown staining as shown in Figure 7.10d. These results together indicate that stable expression of magA does not lead to increased iron uptake in 293 cells.

### 7.3.3   MRI of magA Expressing Cells

Imaging of 293 cells expressing magA was performed to determine if gene expression leads to increased iron uptake that is detectable via MRI. In particular, MRI was performed on stable cell lines expressing magA from either the AMB-1 or MS-1 strain. The MRI results indicate that expression of magA does not lead to increased iron uptake that is detectable via imaging. Figure 7.11 shows example GRE images for stable cells (top 10% derived population) after 72 hours of iron feeding; while images for a single TE are shown, results were similar for all other TEs. Images are shown for cells imaged at a concentration of $1\times10^5$ (Figure 7.11a-c) and $1\times10^6$ cells/mL (Figure 7.11d-f). From the images it is clear that stable cells transfected with magA and cultured in iron rich medium are indistinguishable from untransfected cells cultured in medium containing iron at the same concentration. Similar results were obtained for SE imaging of stably transfected cells expressing magA (top 10% derived population), which are indistinguishable from untransfected cells (Figure 7.12). While images for a single TE is shown, results were similar for all other TEs.
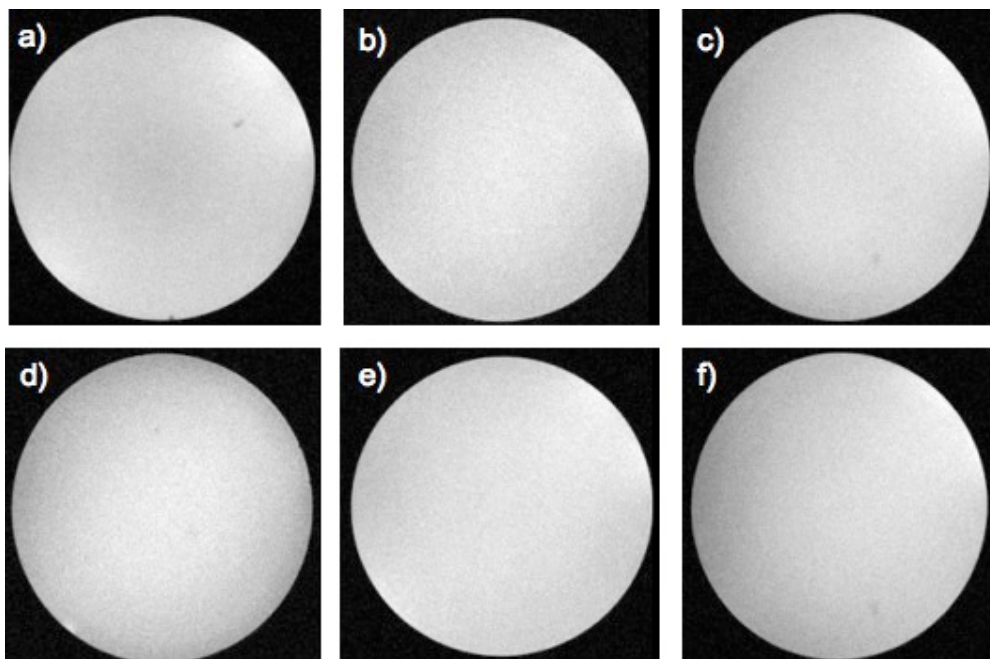
**Figure 7.11—GRE imaging of stably transfected magA expressing cells after 72 hours of iron feeding. Top row show cells at a concentration of $1x10^5$ cells/mL while the bottom row shows cells imaged at a concentration of $1x10^6$ cells/mL. (a) & (d) magA expressing cells from AMB-1 strain; (b) & (e) magA expressing cells from MS-1 strain; (c) & (f) untransfected cells (negative control). Stable cells supplemented with iron are indistinguishable from untransfected cells cultured in iron rich media at the same concentration. (TE/TR = 8.96/250 ms)**

### 7.3.4   Ferritin Gene Transfection

Experiments were also performed transfecting 293 cells with ferritin, in order to assess the effect of over-expression of this gene on iron uptake. In particular, transfection with FTH and FTL was examined separately after cloning each of the genes into the pcDNA 3.1+ vector backbone. Figure 7.13 shows the gel separation results for FTH and FTL following PCR of each gene. In Figure 7.13 the bands for FTH and FTL, which are both approximately 500 base pairs (bp) in length, appear at the correct location based on comparison with the molecular weight ladder.
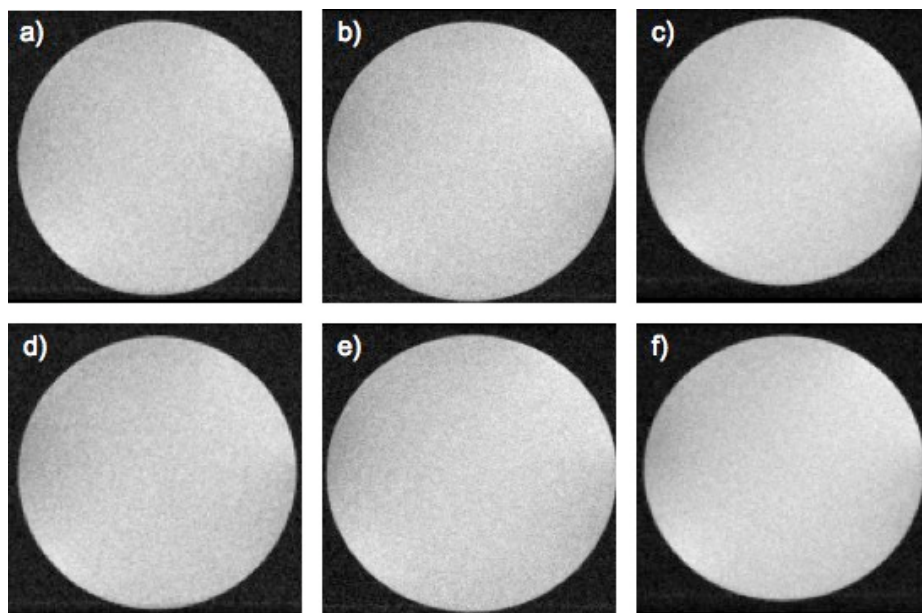
**Figure 7.12—SE imaging of stably transfected magA expressing cells after 72 hours of iron feeding. Top row show cells at a concentration of 1x10$^5$ cells/mL while the bottom row shows cells imaged at a concentration of 1x10$^6$ cells/mL. (a) & (d) magA expressing cells from AMB-1 strain; (b) & (e) magA expressing cells from MS-1 strain; (c) & (f) untransfected cells (negative control). Stable cells supplemented with iron are indistinguishable from untransfected cells cultured in iron rich media at the same concentration. (TE/TR = 16/1000 ms)**

This indicates successful PCR of both the FTH and FTL gene using the designed primers.

Following cloning into the pcDNA 3.1+ backbone, 293 cells were transfected with either

the FTH or FTL gene. Figure 7.14 depicts fluorescence microscopy images of cells

transfected with each gene after 48 hours. In addition, cells transfected with pMAX were

utilized as a positive control, while untransfected cells were used as a negative control.

Of note, unlike the EGFP fusion backbone utilized for magA experiments, the pcDNA

3.1+ backbone does not contain GFP. However, the use of pMAX can be used to

indirectly assess transfection efficiency of 293 cells with the gene of interest. Figure 7.14

demonstrates high transfection efficiency of the positive control pMAX gene. As

expected positive green fluorescence is not present for cells transfected with either the

FTH of FTL gene, as well as for the untransfected cells. However, the high level of

124

positive fluorescence for the pMAX control is a strong indicator of successful transfection of 293 cells with pcDNA 3.1+ containing either the FTH or FTL gene.
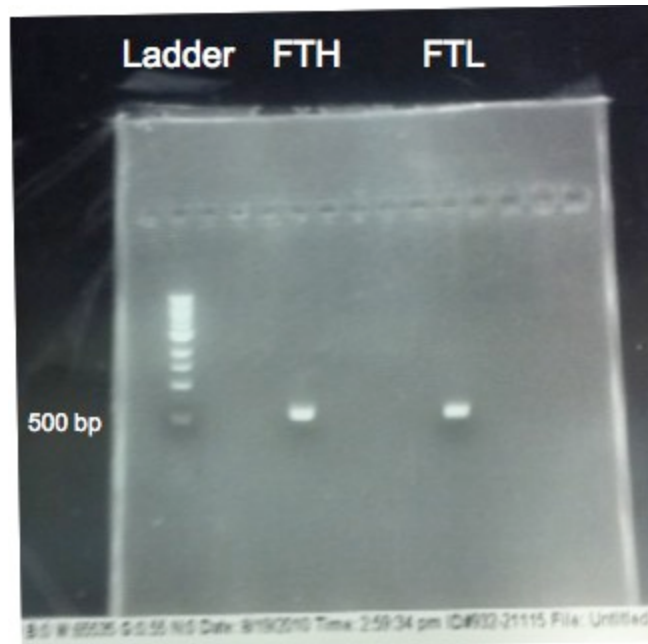


**Figure 7.13—Gel purification results following PCR of FTH and FTL genes. The gel bands for FTH and FTL, which are both approximately 500 bp in length, appear at the correct approximate location based on comparison to the molecular weight ladder. This indicates successful PCR of the two genes using the designed primers.**

*7.3.5   Histological Staining of Ferritin Expressing Cells*

Cells transfected with either the FTH or FTL gene were cultured in medium containing supplemental ferric citrate (either 250 μM or 1 mM) for a period of 72 hours. Following the culture period, PBS washing, and fixing of the cells, Prussian Blue staining was performed to detect the presence of iron. Of note, untransfected cells fed iron at both concentrations were utilized as negative controls. Figure 7.15 shows the results of the Prussian Blue staining for 293 cells supplemented with 250 μM iron. As shown in Figure 7.15a, well-distributed positive blue staining was found for cells transfected with FTH. This positive staining was present throughout the cell culture dish indicating increased iron uptake resulting from FTH gene transfection.
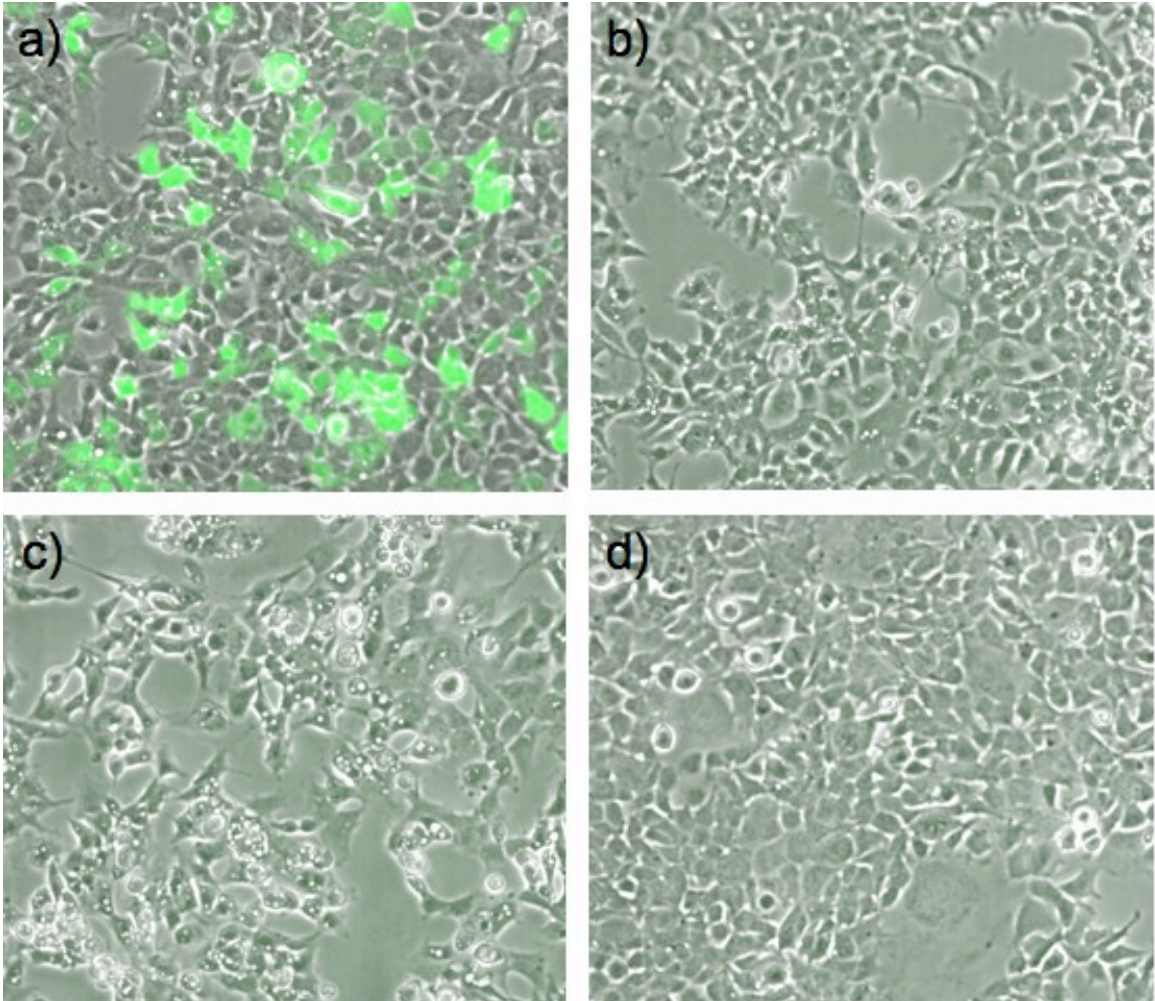
**Figure 7.14—Fluorescence microscopy of 293 cells 48 hours after transfection of ferritin using Lipofectamine LTX. (a) pMAX (positive control); (b) FTH gene; (c) FTL gene; (d) untransfected cells. The high levels of pMAX transfection suggest successful transfection of 293 cells with the ferritin genes using Lipofectamine LTX. (Magnification = 10x)**

There were regions that did not show positive staining, but this is likely because transient transfections do not result in all cells expressing the gene of interest. This staining pattern was not found in the FTL sample or either of the control samples. Figure 7.16 shows the results of the Prussian Blue staining for 293 cells supplemented with 1 mM iron and further supports increased iron uptake with FTH gene transfection. Similar to the staining resulting with the lower iron feeding concentration, cells transfected with FTH and supplemented with 1 mM iron for 72 hours show well-distributed blue staining present in

many regions of the culture dish. In addition, there does not appear to be a difference in staining resulting from feeding cells with 250 μM or 1 mM iron.
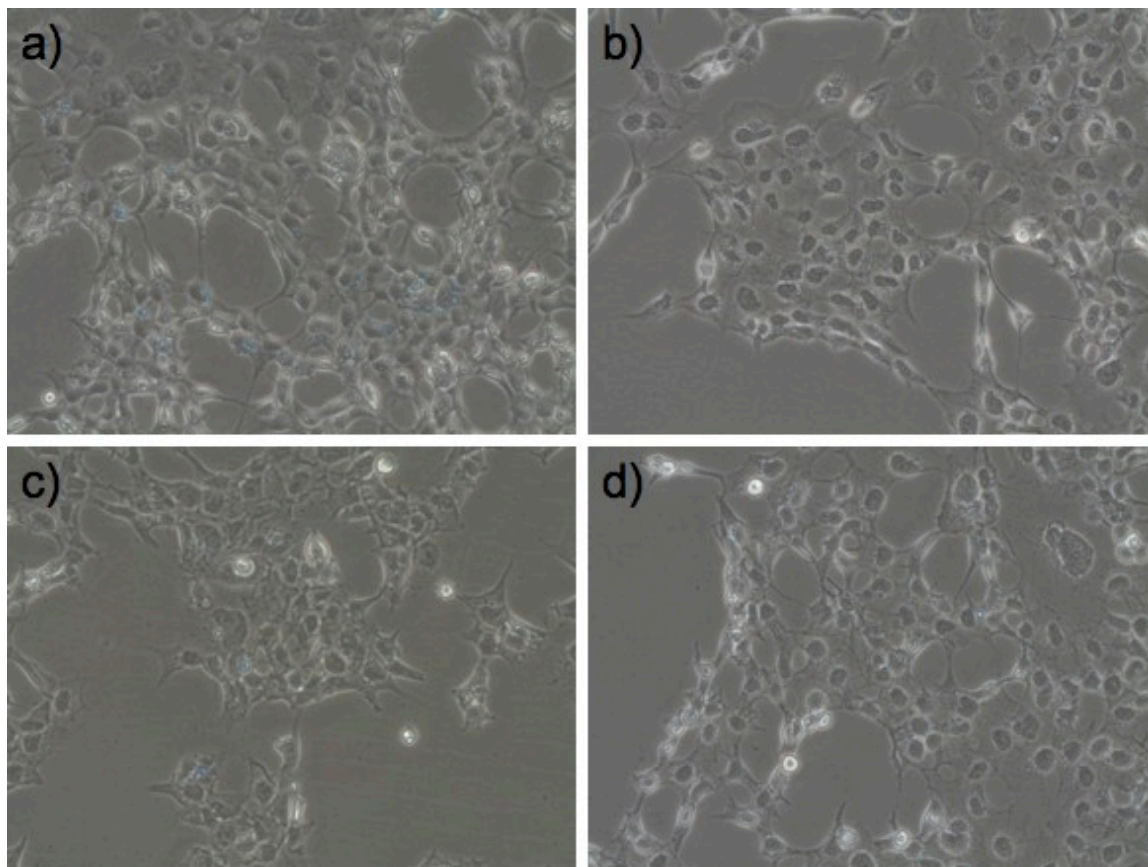


**Figure 7.15—Prussian Blue staining of transfected cells after 250 μM iron feeding for 72 hours. (a) FTH gene transfected cells; (b) pMAX transfected cells; (c) FTL gene transfected cells; (d) untransfected cells (negative control). FTH transfected cells show well-distributed blue staining that can be detected throughout the culture dish. This indicates increased iron uptake resulting from FTH gene transfection. This staining is not present in the control samples or the FTL transfect sample. (Magnification = 10x)**

### 7.3.6   MRI of Ferritin Expressing Cells

MRI was also performed on 293 cells transiently transfected with either the FTH or FTL gene after 72 hours of iron feeding. Cells were cultured in media supplemented with either 250 μM or 1mM ferric citrate and imaged as concentrations of $1x10^6$ or $1x10^7$ cell/mL. In general, the results indicate that transient transfection with either FTH or FTL

and subsequent culture in iron rich medium does not result in detection of cells using 14T

MR imaging.
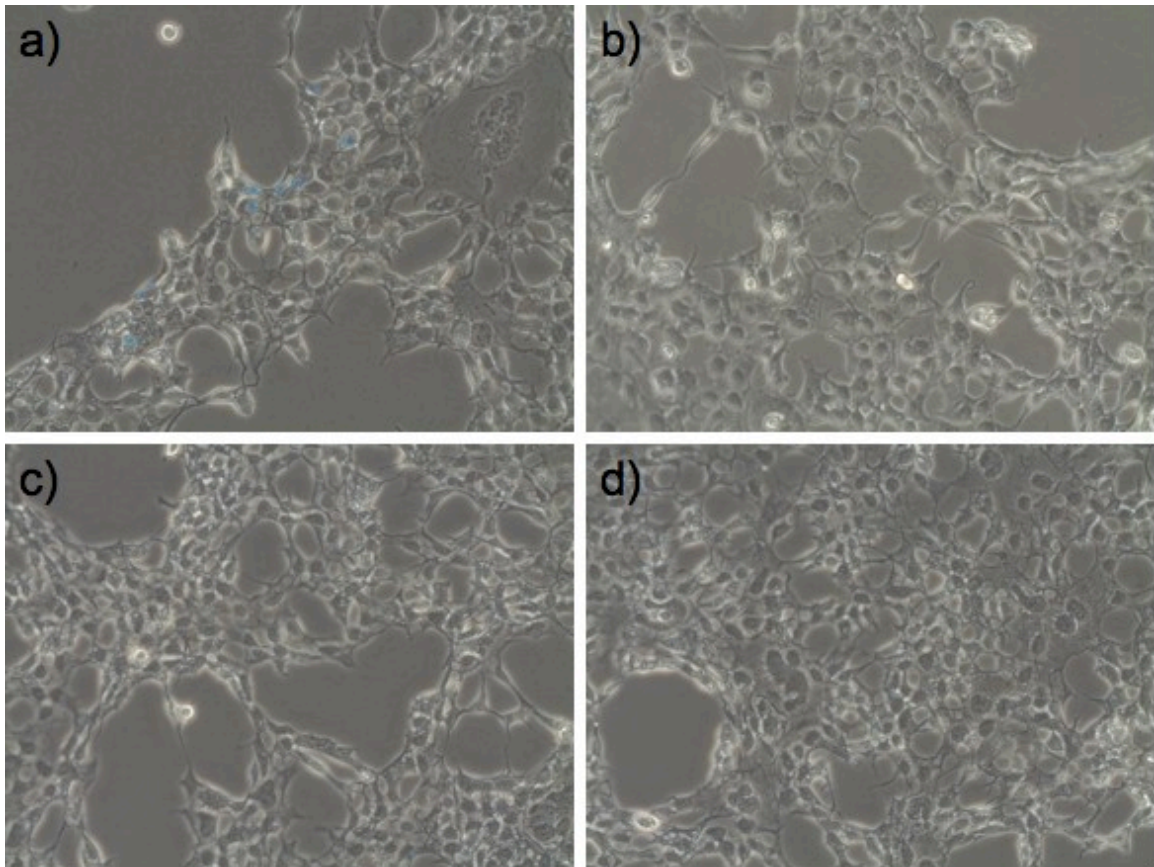


**Figure 7.16—Prussian Blue staining of transfected cells after 1 mM iron feeding for 72 hours. (a) FTH gene transfected cells; (b) pMAX transfected cells; (c) FTL gene transfected cells; (d) untransfected cells (negative control). FTH transfected cells show well-distributed blue staining that can be detected throughout the culture dish. This indicates increased iron uptake resulting from FTH gene transfection. This staining is not present in the control samples or the FTL transfect sample. (Magnification = 10x)**

Figure 7.17 shows the GRE imaging results for FTH and FTL transfected cells as well as

untransfected control cells. While images for a single TE are shown, results were similar

for all other TEs. In addition, results are shown for cells supplemented with 1 mM ferric

citrate; imaging results for cell supplemented with 250 µM were similar (not shown).
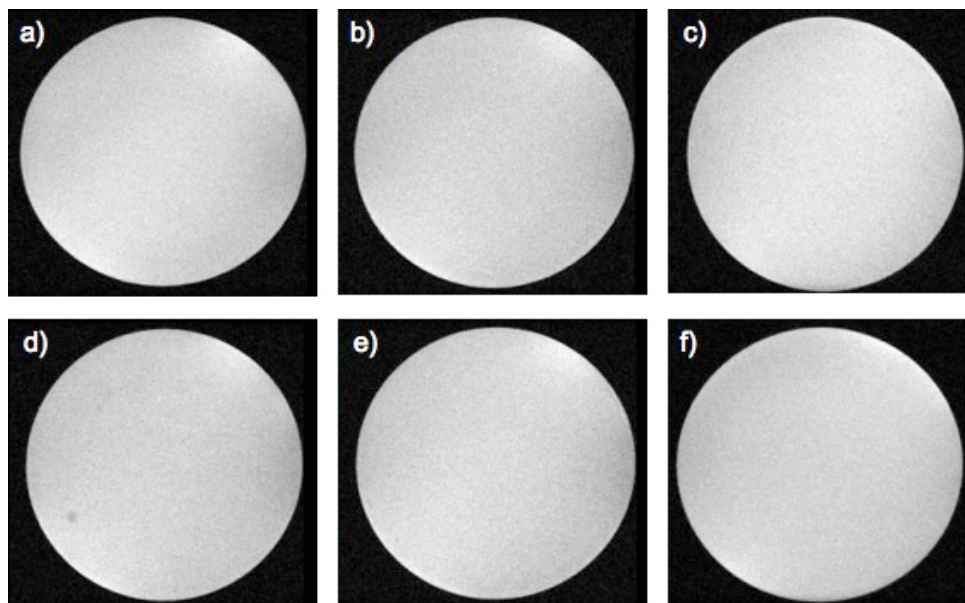
**Figure 7.17—GRE imaging of transiently transfected ferritin expressing cells after 72 hours of iron feeding (1 mM ferric citrate). Top row shows cells at a concentration of $1\text{x}10^6$ cells/mL while the bottom row shows cells imaged at a concentration of $1\text{x}10^7$ cells/mL. (a) & (d) 293 cells expressing FTH; (b) & (e) 293 cells expressing FTL; (c) & (f) untransfected cells (negative control). Transiently transfected cells expressing either FTH or FTL and supplemented with iron are indistinguishable from untransfected cells cultured in iron rich media at the same concentration. (TE/TR = 8.96/250 ms)**

Results for SE imaging of 293 cells transiently transfected with FTH or FTL were similar to that obtained for GRE imaging. Following 72-hour culture in the presence of either 250 μM or 1 mM ferric citrate, cells transiently expressing FTH or FTL could not be distinguished from untransfected cells supplemented with iron at the same concentration. Figure 7.18 shows SE imaging with a TE/TR = 16/1000 ms for cells supplemented with 1 mM ferric citrate; images obtained for other TEs were similar as well as those for 250 μM iron supplementation.

## 7.4    Discussion

Genetically modifying cells to increase their uptake of iron is an alternative technique to conventional methods that load cells with iron oxide-based contrast agents. This

technique has several potential advantages such as the ability to allow endogenous uptake of iron, and avoidance of issues associated with contrast agent dilution that limits the length of time that implanted cells can be tracked with MRI (68).
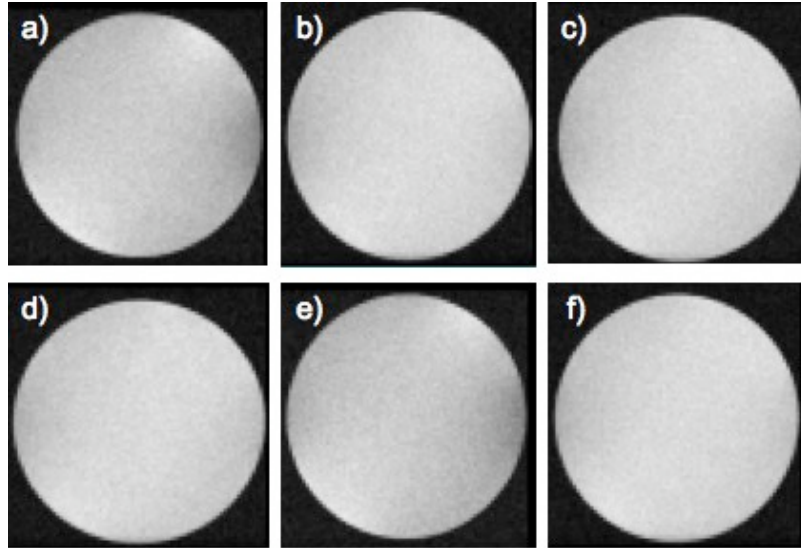


**Figure 7.18—SE imaging of transiently transfected magA expressing cells after 72 hours of iron feeding (1 mM ferric citrate). Top row shows cells at a concentration of $1x10^6$ cells/mL while the bottom row shows cells imaged at a concentration of $1x10^7$ cells/mL. (a) & (d) 293 cells expressing FTH; (b) & (e) 293 cells expressing FTL; (c) & (f) untransfected cells (negative control). Transfected cells supplemented with iron are indistinguishable from untransfected cells cultured in iron rich media at the same concentration. (TE/TR = 16/1000 ms)**

In addition, because active gene expression is required for cells to uptake iron, this can provide an indicator that cells are not only present at the ROI, but that they are also functionally viable. In these studies two different types of genes were examined for their ability to promote cellular uptake of iron. The first gene is magA, which is present in MTB and has been shown to play a role in the formation of iron-storing magnetosomes within these bacteria. The second gene, ferritin is found within mammalian cells (as well as other cell types) and is responsible for iron storage and controlled release.

The first set of studies indicates that magA gene expression alone is not sufficient to increase cellular uptake of iron and facilitate detection using MR imaging. These results

were demonstrated for both transient transfection of the magA gene as well as for stable cell lines generated using FACS and culture under drug selection. In both cases, culture of cells in medium containing 250 μM ferric citrate did not result in increased iron uptake and detection via MRI. In addition Prussian Blue staining to detect the presence of iron did not show differences between magA expressing cells and untransfected controls.

The results obtained are in contrast to results obtained by Zurkiya *et al.* who have reported increased iron uptake and subsequent MR detection of HEK 293FT cells expressing magA (68). In their study, a lentiviral vector was utilized to introduce the gene into cells, which generally leads to extremely high (near 100%) transfection efficiencies and expression levels within cells. While this may be a factor in the different results obtained, the stable cell lines generated in the present study resulted in high percentages of cells expressing magA and high levels of expression within cells. Furthermore, in the results reported by Zurkiya *et al.* MR imaging of cells was performed in highly concentrated 100 μL pellets containing $1x10^7$ cells. While magA expressing cells supplemented with iron show the strongest signal loss in their study, signal voids are also present for non-expressing cells supplemented with iron, as well as magA expressing cells cultured without iron supplementation. This is to be expected, as the aggregation of a large quantity of cells into a pellet will create a susceptibility artifact with respect to the surrounding environment. Lastly, in the results by Zurkiya *et al.* the presence of intracellular iron was detected using transmission electron microscopy (TEM), which was not performed in the present study.

The current results presented also differ from those of Goldhawk *et al.* who report increased uptake of iron by magA expressing stable N2A cells when cultured in media

supplemented with either 62.5 µM or 250 µM ferric citrate (69). This increase in iron uptake was assessed using DAB-enhanced Prussian Blue staining as well as with MR imaging at 11T. While the staining results presented by Goldhawk *et al.* show positive staining for N2A cells expressing magA when supplemented with 62.5 µM iron, the results for non-expressing cells are not shown. Given that wild-type cells uptake iron as part of normal homeostatic processes, this makes it difficult to assess whether magA expression in fact causes increased iron uptake. Furthermore, the DAB enhancement reaction is time dependent, and lengthy exposures can lead to high background; as such it is important to compare staining results with a negative control. Of note, Goldhawk *et al.* also examined cells expressing a magA mutant known to eliminate magnetic properties, but these cells demonstrate positive staining when supplemented with 250 µM iron. Although Goldhawk *et al.* report detection of magA expressing cells via MRI, non-expressing cells are not shown, and cells expressing the magA mutant show distinct signal voids as well. This combined with the presence of large artifacts within the images makes it difficult to assess the positive effect of magA expression on MR detection.

While the results of the present studies indicate that magA expression alone does not lead to increased iron uptake and subsequent MR detection, future studies focused on expression of MTB genes should investigate other genes involved in magnetosome formation. For example, Arakaki *et al.* identified the proteins encoded by the gene Mms5, Mms6, Mms7, and Mms13 as being directly involved in magnetite crystal formation within the AMB-1 strain of MTB (62). As such, these genes should be investigated for their ability to promote iron uptake in mammalian cells and subsequent MR detection. Furthermore, given the complex relationship and interplay between genes that is

necessary for protein expression, future studies should also investigate simultaneous co-expression of multiple gene combinations in order to promote increased iron uptake. Lastly while developmental work can be more easily performed in 293 cells, successful validation will eventually need to be confirmed in MSCs so that this technique can be applied to MR-based monitoring of tissue regeneration therapies.

The present set of studies also examined the effect of ferritin over-expression on the ability to increase iron uptake and promote detection of cells via MRI. In these studies, cells were transiently transfected with either the FTH or FTL gene and supplemented with media containing either 250 μM or 1 mM iron. Prussian Blue staining showed positive results for cells transfected with FTH, while FTL transfected cells did not show increased iron uptake. In particular, cell cultures containing the FTH gene showed well-distributed staining without the need for DAB enhancement. Of note, while not all cells showed positive staining, this is to be expected based on the transient transfection methods used in these studies. While cells expressing FTH demonstrated positive staining for iron, this was not detectable using GRE and SE MR imaging at 14T. Cells supplemented with iron and imaged at varying concentrations could not be distinguished from untransfected cells cultured in iron-rich medium.

Similar to the results presented in the current study, Naumova *et al*. have reported increased iron uptake in C2C12 cells expressing FTH supplemented with 1 mM ferric citrate; iron presence was detected by Prussian Blue staining (70). However unlike the present study, Naumova *et al*. also report *in vitro* MR detection of iron-supplemented cells expressing FTH at 3T. One potential reason for this difference is that Naumova *et al*. used stable cell lines resulting in high expression of the FTH gene. In addition,

detection at 3T was of a highly concentrated pellet containing $6\times10^7$ cells. In the present study, cells were imaged in a well-distributed suspension. This combined with the heterogeneously expressing cell population resulting from transient transfection would likely make it more challenging to detect subtle increases in iron uptake via MRI. Of note, Deans *et al*. also report MR detection of iron-supplemented C17 cells stably expressing FTH when imaged as concentrated cell pellets at 1.5T (72).

The FTH gene expression results obtained in the present study as well as the results reported in other studies suggest that future steps should focus on stable expression of the FTH gene in 293 cells. This can be achieved by cell sorting and drug selection, or through the use of viral transduction methods. In order to create stable cell lines using FACS, it would be necessary to clone the FTH gene into a pEGFP vector; the pcDNA vector does not contain the EGFP protein. Once in this vector, cells can be sorted based on their expression of EGFP and consequently the FTH gene of interest. In sorting it is common to isolate cell populations based on their varied expression levels. While the highest levels of gene expression (top 10%) are clearly desired, it is important to determine whether expression of foreign DNA has any effect on cell viability and proliferation. As such, it is often useful to isolate the middle 50% of cells expressing the gene of interest. These populations can then be maintained under drug selection in order to obtain stable cell lines with high viability and expression of the gene of interest (i.e. FTH). This stable population of cells could potentially lead to more significant increased iron uptake and resulting MR detection.

Similar to studies focused on expression of bacterial genes, future studies should focus on generating stable cell lines co-expressing multiple genes. For example, Genove

*et al*. have reported MR detection of human lung cancer cells over-expressing the FTH and FTL gene (114). In addition, Deans *et al*. have reported increased iron uptake and MR detection resulting from co-expression of FTH and transferrin (72). As such, generation of stable cell lines expressing combinations of these genes, as well as others important in iron internalization and storage will likely further genetic modification techniques as a means of facilitating MR contrast. Lastly, these gene expression studies will ultimately need to be carried out in MSCs, in order to ensure that this technique can be applied to MR-based monitoring of stem cell tissue engineering therapies.

## 7.5    **Acknowledgements**

# Chapter 8: Conclusion

## 8.1 Research Outcomes

Overall, these research studies have focused on the ability to non-invasively and longitudinally track cells using MRI after implantation into the body for tissue regeneration purposes. In particular, the majority of this work has focused on the application of this technology to stem cell tracking during tissue engineering of the musculoskeletal system. A technique to track stem cells in this manner would be highly useful in the continued development of stem cell-based tissue engineering strategies for the musculoskeletal system, as well as in the eventual transition of these techniques into the clinic. Furthermore, this technique also has broader potential application to a variety of pathological conditions in which stem cells have shown promise in the regeneration of damaged or diseased tissue. Currently, the majority of stem cell-based therapies are still being investigated within animal models, and highly invasive histological methods are employed in order to assess therapy. While these assessment techniques may be acceptable for use on animals within a research setting, they are clearly not applicable in a clinical setting as part of patient treatment. As such the development of these MRI-based techniques in parallel with the continued development of stem cell-based therapies is critically important.

### 8.1.1 Iron Oxide Contrast Agent-based Studies

The first set of research studies focused on cellular uptake of iron oxide-based contrast agents that are detectable via MRI using GRE and SE imaging. The studies included analysis of conventional nanometer-sized particles along with considerably

larger 1.63 μM iron oxide particles. The results indicate the ability to successfully label MSCs with both types of particles, although nanometer-sized particles require the use of a TA in order to facilitate cellular uptake. In addition, cells labeled with both types of contrast agents are detectable via MRI at both 3T and 11T. 3T imaging allows imaging of a population of labeled cells while 11T imaging provides the capability to achieve near cellular resolution and thus potentially image single cells labeled with multiple contrast agent particles.

Focusing on the application of these techniques to musculoskeletal tissue engineering, cells labeled with iron oxides can be encapsulated within hydrogels without affecting their viability, and encapsulated cell constructs also exhibit characteristic signal voids on MR images. These studies also demonstrate *ex vivo* detection of iron oxide-labeled cells within a rat model of IVD degeneration, bovine knee articular cartilage, and a mouse hind-limb muscle model. These results suggest the effectiveness of detecting labeled cells within a native musculoskeletal tissue environment.

The results of these studies as well as those reported by others indicate potential limitations of these techniques however. First while differentiation of labeled MSCs into multiple tissue types appears feasible, questions remain about the ability to differentiate iron oxide-labeled cells particularly along the chondrogenic lineage. These issues partly arise from the presence of excess extracellular iron oxide particles that are present following labeling and PBS washing. This is especially true when micrometer-sized particles are used, and their tendency to aggregate is further exacerbated by the process of pellet formation utilized during *in vitro* chondrogenesis. However, based on the promise

of iron-oxide labeling and its potential importance in the desire to non-invasively monitor implanted cells, further studies to address these issues are certainly warranted.

### 8.1.2   *Genetic Modification-based Studies*

While the use of iron oxides focuses on generating contrast at the cellular level via internalization of particles, genetic modification techniques aim to control MR contrast at the even more basic DNA level. Essentially the goal is to introduce foreign DNA into the cell in order to modulate its uptake, processing, sequestration, and long-term storage of iron. In this way it is possible to generate contrast between gene transfected cells and the surrounding tissue environment. This set of research studies examined HEK 293 expression of both bacterial genes and mammalian cell genes in order to promote contrast and subsequent MR detection.

While mammalian cell expression of the bacterial gene magA has been reported as being capable of promoting increased iron uptake and MR detection, those were results do not agree with the current results obtained in these research studies. In the present studies, both transient and stable expression of magA did not lead to increased iron uptake or the ability to distinguish cells as signal voids on MR images. However, there are numerous other genes from MTB that have been implicated as having a role in iron uptake and storage within magnetosomes. As such, these genes should be investigated to determine their potential in facilitating increased iron uptake in mammalian cells and promoting detection via MRI. It is also highly likely that multiple genes acting in concert will need to be expressed simultaneously in order for this technique to be viable. As a result, research into the complex interaction between these different magnetotactic genes is necessary to better understand the underlying mechanisms involved.

Preliminary studies were also conducted investigating over-expression of ferritin as a means of promoting iron uptake and generating MR contrast in mammalian cells. Based on transient transfection experiments in HEK 293 cells, it appears that transfection with the FTH gene leads to increased iron uptake that can be detected with Prussian Blue staining. However, this amount of increased iron uptake does not allow detection of cells via MRI, suggesting that future experiments with stable cell lines expressing FTH should be performed. MR detection of cells expressing FTH has been previously reported, but generally requires cells to be localized into highly concentrated pellets to facilitate MR detection. However, the clinical utility of this technique for visualization is limited since in many applications implanted cell populations will likely distribute within the implanted tissue. Consequently, in order for MRI-based tracking techniques to be robust they should be able to monitor cells distributed throughout native tissue even if only for a short period of time. Lastly, as suggested for future studies involving bacterial genes, over-expression of ferritin in combination with other genes critical to normal iron uptake and storage should be investigated.

## 8.2    Final Considerations

The ultimate success of MRI cell tracking as a technique for monitoring stem cell-based tissue engineering depends on a several important factors that must be considered as part of the ongoing development of this methodology. In an ideal case it would be possible to monitor implanted stem cells via MRI indefinitely. In reality, cell division, iron release, and potential differentiation effects will likely limit the length of time that cells can be accurately monitored. Given this limitation, it is important to consider the length of time that cells can be tracked in the context of the amount of time necessary for

successful stem cell-based tissue repair. This will likely vary depending on several factors such as the tissue of interest, the extent of repair needed, and the effectiveness of the body's natural repair processes.

Another consideration is the long term of fate of the increased iron content present within implanted cells. For examples, when cells divide or die, it is important to understand what happens to any remaining iron. For example, it is possible that the iron is internalized by other highly phagocytic cells (e.g. macrophages), which is potentially undesirable. Given that large amounts of iron can be toxic, it is also important that any residual iron does not accumulate within the body and lead to any potentially harmful effects.

This set of research studies has largely focused on using MRI to assess the bio-distribution of implanted cells. However, it is also important to assess whether implanted cells are functioning appropriately and achieving effective tissue repair. While MRI is primarily utilized for its excellent anatomical capabilities, it is increasingly being investigated for its ability to provide functional information (e.g. $T_{1\rho}$ imaging). In addition, advancements in technology have made it possible to combine imaging modalities. For example the development of combined MRI/positron emission tomography (PET) scanners makes it possible to gain functional information with corresponding anatomical localization. Thus the techniques investigated in the current research studies should ideally not interfere with other MR-based functional assessment techniques or the capabilities of other imaging modalities.

The results obtained from these studies suggest the promise of iron-based techniques for monitoring stem cell tissue engineering of the musculoskeletal system via MRI. The

results also highlight the future work necessary for further validation and optimization of this technique. While significant research is still necessary before these techniques can be transitioned into a clinical setting, the clear potential benefits of their successful development are a strong motivation for continued investigative efforts.

# References

1.   Sekiya I, Larson BL, Smith JR, Pochampally R, Cui JG, Prockop DJ. Expansion of human adult stem cells from bone marrow stroma: conditions that maximize the yields of early progenitors and evaluate their quality. Stem Cells 2002;20(6):530-541.

2.   Bonfield TL, Caplan AI. Adult mesenchymal stem cells: an innovative therapeutic for lung diseases. Discov Med;9(47):337-345.

3.   Raghunath J, Rollo J, Sales KM, Butler PE, Seifalian AM. Biomaterials and scaffold design: key to tissue-engineering cartilage. Biotechnol Appl Biochem 2007;46(Pt 2):73-84.

4.   McGrath MH. Peptide growth factors and wound healing. Clin Plast Surg 1990;17(3):421-432.

5.   Choi NY, Kim BW, Yeo WJ, Kim HB, Suh DS, Kim JS, Kim YS, Seo YH, Cho JY, Chun CW, Park HS, Shetty AA, Kim SJ. Gel-type autologous chondrocyte (Chondron) implantation for treatment of articular cartilage defects of the knee. BMC Musculoskelet Disord;11:103.

6.   Dragoo JL, Samimi B, Zhu M, Hame SL, Thomas BJ, Lieberman JR, Hedrick MH, Benhaim P. Tissue-engineered cartilage and bone using stem cells from human infrapatellar fat pads. J Bone Joint Surg Br 2003;85(5):740-747.

7.   Westreich R, Kaufman M, Gannon P, Lawson W. Validating the subcutaneous model of injectable autologous cartilage using a fibrin glue scaffold. Laryngoscope 2004;114(12):2154-2160.

8.   Bryant SJ, Anseth KS. Hydrogel properties influence ECM production by chondrocytes photoencapsulated in poly(ethylene glycol) hydrogels. J Biomed Mater Res 2002;59(1):63-72.

9.   Williams CG, Kim TK, Taboas A, Malik A, Manson P, Elisseeff J. In vitro chondrogenesis of bone marrow-derived mesenchymal stem cells in a photopolymerizing hydrogel. Tissue Eng 2003;9(4):679-688.

10.  Bryant SJ, Anseth KS, Lee DA, Bader DL. Crosslinking density influences the morphology of chondrocytes photoencapsulated in PEG hydrogels during the application of compressive strain. J Orthop Res 2004;22(5):1143-1149.

11.  Bryant SJ, Bender RJ, Durand KL, Anseth KS. Encapsulating chondrocytes in degrading PEG hydrogels with high modulus: engineering gel structural changes to facilitate cartilaginous tissue production. Biotechnol Bioeng 2004;86(7):747-755.

12. Bryant SJ, Chowdhury TT, Lee DA, Bader DL, Anseth KS. Crosslinking density influences chondrocyte metabolism in dynamically loaded photocrosslinked poly(ethylene glycol) hydrogels. Ann Biomed Eng 2004;32(3):407-417.

13. Henriksson HB, Svanvik T, Jonsson M, Hagman M, Horn M, Lindahl A, Brisby H. Transplantation of human mesenchymal stems cells into intervertebral discs in a xenogeneic porcine model. Spine 2009;34(2):141-148.

14. Dickhut A, Gottwald E, Steck E, Heisel C, Richter W. Chondrogenesis of mesenchymal stem cells in gel-like biomaterials in vitro and in vivo. Front Biosci 2008;13:4517-4528.

15. Beadle OA. The intervertebral discs: observations on their normal and morbid anatomy in relation to certain spinal deformities. Medical Research Council Special Report Series 1931;161.

16. Boos N, Weissbach S, Rohrbach H, Weiler C, Spratt KF, Nerlich AG. Classification of age-related changes in lumbar intervertebral discs: 2002 Volvo Award in basic science. Spine 2002;27(23):2631-2644.

17. Leung VY, Chan D, Cheung KM. Regeneration of intervertebral disc by mesenchymal stem cells: potentials, limitations, and future direction. Eur Spine J 2006;15 Suppl 3:S406-413.

18. Battie MC, Videman T. Lumbar disc degeneration: epidemiology and genetics. J Bone Joint Surg Am 2006;88 Suppl 2:3-9.

19. Pfirrmann CW, Metzdorf A, Zanetti M, Hodler J, Boos N. Magnetic resonance classification of lumbar intervertebral disc degeneration. Spine 2001;26(17):1873-1878.

20. Raj PP. Intervertebral disc: anatomy-physiology-pathophysiology-treatment. Pain Pract 2008;8(1):18-44.

21. Pearce RH, Grimmer BJ, Adams ME. Degeneration and the chemical composition of the human lumbar intervertebral disc. J Orthop Res 1987;5(2):198-205.

22. Urban JP, Winlove CP. Pathophysiology of the intervertebral disc and the challenges for MRI. J Magn Reson Imaging 2007;25(2):419-432.

23. Errico TJ. Lumbar disc arthroplasty. Clin Orthop Relat Res 2005(435):106-117.

24. Strassburg S, Richardson SM, Freemont AJ, Hoyland JA. Co-culture induces mesenchymal stem cell differentiation and modulation of the degenerate human nucleus pulposus cell phenotype. Regen Med;5(5):701-711.

25. Sakai D, Mochida J, Yamamoto Y, Nomura T, Okuma M, Nishimura K, Nakai T, Ando K, Hotta T. Transplantation of mesenchymal stem cells embedded in

Atelocollagen gel to the intervertebral disc: a potential therapeutic model for disc degeneration. Biomaterials 2003;24(20):3531-3541.

26. Zhang YG, Guo X, Xu P, Kang LL, Li J. Bone mesenchymal stem cells transplanted into rabbit intervertebral discs can increase proteoglycans. Clin Orthop Relat Res 2005(430):219-226.

27. Sakai D, Mochida J, Iwashina T, Hiyama A, Omi H, Imai M, Nakai T, Ando K, Hotta T. Regenerative effects of transplanting mesenchymal stem cells embedded in atelocollagen to the degenerated intervertebral disc. Biomaterials 2006;27(3):335-345.

28. Sakai D, Mochida J, Iwashina T, Watanabe T, Nakai T, Ando K, Hotta T. Differentiation of mesenchymal stem cells transplanted to a rabbit degenerative disc model: potential and limitations for stem cell therapy in disc regeneration. Spine 2005;30(21):2379-2387.

29. Mandelbaum BR, Browne JE, Fu F, Micheli L, Mosely JB, Jr., Erggelet C, Minas T, Peterson L. Articular cartilage lesions of the knee. Am J Sports Med 1998;26(6):853-861.

30. Newman AP. Articular cartilage repair. Am J Sports Med 1998;26(2):309-324.

31. Buckwalter JA, Mankin HJ. Articular cartilage: tissue design and chondrocyte-matrix interactions. Instr Course Lect 1998;47:477-486.

32. Bentley G, Minas T. Treating joint damage in young people. Bmj 2000;320(7249):1585-1588.

33. Temenoff JS, Mikos AG. Review: tissue engineering for regeneration of articular cartilage. Biomaterials 2000;21(5):431-440.

34. Tatebe M, Nakamura R, Kagami H, Okada K, Ueda M. Differentiation of transplanted mesenchymal stem cells in a large osteochondral defect in rabbit. Cytotherapy 2005;7(6):520-530.

35. Liu Y, Shu XZ, Prestwich GD. Osteochondral defect repair with autologous bone marrow-derived mesenchymal stem cells in an injectable, in situ, cross-linked synthetic extracellular matrix. Tissue Eng 2006;12(12):3405-3416.

36. Schenck JF. The role of magnetic susceptibility in magnetic resonance imaging: MRI magnetic compatibility of the first and second kinds. Med Phys 1996;23(6):815-850.

37. Demas V. Magnetic resonance for *in vitro* medical diagnostics: superparamagnetic nanoparticle-based magnetic relaxation switches. New Journal of Physics 2011;13(2).

38. Schlorf T, Meincke M, Kossel E, Gluer CC, Jansen O, Mentlein R. Biological properties of iron oxide nanoparticles for cellular and molecular magnetic resonance imaging. Int J Mol Sci;12(1):12-23.

39. Lunov O, Zablotskii V, Syrovets T, Rocker C, Tron K, Nienhaus GU, Simmet T. Modeling receptor-mediated endocytosis of polymer-functionalized iron oxide nanoparticles by human macrophages. Biomaterials;32(2):547-555.

40. Frank JA, Miller BR, Arbab AS, Zywicke HA, Jordan EK, Lewis BK, Bryant LH, Jr., Bulte JW. Clinically applicable labeling of mammalian and stem cells by combining superparamagnetic iron oxides and transfection agents. Radiology 2003;228(2):480-487.

41. Kalish H, Arbab AS, Miller BR, Lewis BK, Zywicke HA, Bulte JW, Bryant LH, Jr., Frank JA. Combination of transfection agents and magnetic resonance contrast agents for cellular imaging: relationship between relaxivities, electrostatic forces, and chemical composition. Magn Reson Med 2003;50(2):275-282.

42. Arbab AS, Bashaw LA, Miller BR, Jordan EK, Lewis BK, Kalish H, Frank JA. Characterization of biophysical and metabolic properties of cells labeled with superparamagnetic iron oxide nanoparticles and transfection agent for cellular MR imaging. Radiology 2003;229(3):838-846.

43. Guzman R, Uchida N, Bliss TM, He D, Christopherson KK, Stellwagen D, Capela A, Greve J, Malenka RC, Moseley ME, Palmer TD, Steinberg GK. Long-term monitoring of transplanted human neural stem cells in developmental and pathological contexts with MRI. Proc Natl Acad Sci U S A 2007;104(24):10211-10216.

44. Unger EC. How can superparamagnetic iron oxides be used to monitor disease and treatment? Radiology 2003;229(3):615-616.

45. Hoehn M, Kustermann E, Blunk J, Wiedermann D, Trapp T, Wecker S, Focking M, Arnold H, Hescheler J, Fleischmann BK, Schwindt W, Buhrle C. Monitoring of implanted stem cell migration in vivo: a highly resolved in vivo magnetic resonance imaging investigation of experimental stroke in rat. Proc Natl Acad Sci U S A 2002;99(25):16267-16272.

46. Arbab AS, Jordan EK, Wilson LB, Yocum GT, Lewis BK, Frank JA. In vivo trafficking and targeted delivery of magnetically labeled stem cells. Hum Gene Ther 2004;15(4):351-360.

47. Auer VJ, Bucher J, Schremmer-Danninger E, Paulmurugan R, Maechler P, Reiser MF, Stangl MJ, Berger F. Non-Invasive Imaging of Ferucarbotran Labeled INS-1E Cells And Rodent Islets In Vitro and In Transplanted Diabetic Rats. Curr Pharm Biotechnol.

48. Reddy AM, Kwak BK, Shim HJ, Ahn C, Lee HS, Suh YJ, Park ES. In vivo tracking of mesenchymal stem cells labeled with a novel chitosan-coated superparamagnetic iron oxide nanoparticles using 3.0T MRI. J Korean Med Sci;25(2):211-219.

49. Addicott B, Willman M, Rodriguez J, Padgett K, Han D, Berman D, Hare JM, Kenyon NS. Mesenchymal stem cell labeling and in vitro MR characterization at 1.5 T of new SPIO contrast agent: Molday ION Rhodamine-B. Contrast Media Mol Imaging;6(1):7-18.

50. Rief M, Wagner M, Franiel T, Bresan V, Taupitz M, Klessen C, Hamm B, Asbach P. Detection of focal liver lesions in unenhanced and ferucarbotran-enhanced magnetic resonance imaging: a comparison of T2-weighted breath-hold and respiratory-triggered sequences. Magn Reson Imaging 2009;27(9):1223-1229.

51. Higashihara H, Murakami T, Kim T, Hori M, Onishi H, Nakata S, Osuga K, Tomoda K, Nakamura H. Differential diagnosis between metastatic tumors and nonsolid benign lesions of the liver using ferucarbotran-enhanced MR imaging. Eur J Radiol;73(1):125-130.

52. Cohen ME, Muja N, Fainstein N, Bulte JW, Ben-Hur T. Conserved fate and function of ferumoxides-labeled neural precursor cells in vitro and in vivo. J Neurosci Res;88(5):936-944.

53. Ke YQ, Hu CC, Jiang XD, Yang ZJ, Zhang HW, Ji HM, Zhou LY, Cai YQ, Qin LS, Xu RX. In vivo magnetic resonance tracking of Feridex-labeled bone marrow-derived neural stem cells after autologous transplantation in rhesus monkey. J Neurosci Methods 2009;179(1):45-50.

54. Arbab AS, Yocum GT, Kalish H, Jordan EK, Anderson SA, Khakoo AY, Read EJ, Frank JA. Efficient magnetic cell labeling with protamine sulfate complexed to ferumoxides for cellular MRI. Blood 2004;104(4):1217-1223.

55. Pawelczyk E, Arbab AS, Pandit S, Hu E, Frank JA. Expression of transferrin receptor and ferritin following ferumoxides-protamine sulfate labeling of cells: implications for cellular magnetic resonance imaging. NMR Biomed 2006;19(5):581-592.

56. Shapiro EM, Skrtic S, Koretsky AP. Sizing it up: cellular MRI using micron-sized iron oxide particles. Magn Reson Med 2005;53(2):329-338.

57. Tang KS, Hann B, Shapiro EM. On the Use of Micron-Sized Iron Oxide Particles (MPIOS) to Label Resting Monocytes in Bone Marrow. Mol Imaging Biol.

58. Rohani R, de Chickera SN, Willert C, Chen Y, Dekaban GA, Foster PJ. In Vivo Cellular MRI of Dendritic Cell Migration Using Micrometer-Sized Iron Oxide (MPIO) Particles. Mol Imaging Biol.

59. Chen A, Siow B, Blamire AM, Lako M, Clowry GJ. Transplantation of magnetically labeled mesenchymal stem cells in a model of perinatal brain injury. Stem Cell Res;5(3):255-266.

60. Blakemore R. Magnetotactic bacteria. Science 1975;190(4212):377-379.

61. Arakaki A, Nakazawa H, Nemoto M, Mori T, Matsunaga T. Formation of magnetite by bacteria and its application. J R Soc Interface 2008;5(26):977-999.

62. Arakaki A, Webb J, Matsunaga T. A novel protein tightly bound to bacterial magnetic particles in Magnetospirillum magneticum strain AMB-1. J Biol Chem 2003;278(10):8745-8750.

63. Fukuda Y, Okamura Y, Takeyama H, Matsunaga T. Dynamic analysis of a genomic island in Magnetospirillum sp. strain AMB-1 reveals how magnetosome synthesis developed. FEBS Lett 2006;580(3):801-812.

64. Suzuki T, Okamura Y, Calugay RJ, Takeyama H, Matsunaga T. Global gene expression analysis of iron-inducible genes in Magnetospirillum magneticum AMB-1. J Bacteriol 2006;188(6):2275-2279.

65. Nakamura C, Burgess JG, Sode K, Matsunaga T. An iron-regulated gene, magA, encoding an iron transport protein of Magnetospirillum sp. strain AMB-1. J Biol Chem 1995;270(47):28392-28396.

66. Nakamura C, Kikuchi T, Burgess JG, Matsunaga T. Iron-regulated expression and membrane localization of the magA protein in Magnetospirillum sp. strain AMB-1. J Biochem 1995;118(1):23-27.

67. Matsunaga T, Okamura Y, Fukuda Y, Wahyudi AT, Murase Y, Takeyama H. Complete genome sequence of the facultative anaerobic magnetotactic bacterium Magnetospirillum sp. strain AMB-1. DNA Res 2005;12(3):157-166.

68. Zurkiya O, Chan AW, Hu X. MagA is sufficient for producing magnetic nanoparticles in mammalian cells, making it an MRI reporter. Magn Reson Med 2008;59(6):1225-1231.

69. Goldhawk DE, Lemaire C, McCreary CR, McGirr R, Dhanvantari S, Thompson RT, Figueredo R, Koropatnick J, Foster P, Prato FS. Magnetic resonance imaging of cells overexpressing MagA, an endogenous contrast agent for live cell imaging. Mol Imaging 2009;8(3):129-139.

70. Naumova AV, Reinecke H, Yarnykh V, Deem J, Yuan C, Murry CE. Ferritin overexpression for noninvasive magnetic resonance imaging-based tracking of stem cells transplanted into the heart. Mol Imaging;9(4):201-210.

71. Liu J, Cheng EC, Long RC, Yang SH, Wang L, Cheng PH, Yang J, Wu D, Mao H, Chan AW. Noninvasive monitoring of embryonic stem cells in vivo with MRI transgene reporter. Tissue Eng Part C Methods 2009;15(4):739-747.

72. Deans AE, Wadghiri YZ, Bernas LM, Yu X, Rutt BK, Turnbull DH. Cellular MRI contrast via coexpression of transferrin receptor and ferritin. Magn Reson Med 2006;56(1):51-59.

73. Bloch F, Hansen WW, Packard M. Nuclear Induction. Physical Review 1946;70(7-8):460-474.

74. Purcell E, Torrey HC, Pound RV. Resonance Absorption by Nuclear Magnetic Moments in a Solid. Physical Review 1946;69(1-2):37-38.

75. Lauterbur PC. Image formation by induced local interactions. Examples employing nuclear magnetic resonance. . Nature 1973;242(5394):190-191.

76. Sepponen R. Rotating Frame and Magnetization Transfer. Stark D, editor: Mosby-Year Book; 1992. 204-218 p.

77. Li X, Pai A, Blumenkrantz G, Carballido-Gamio J, Link T, Ma B, Ries M, Majumdar S. Spatial distribution and relationship of T1rho and T2 relaxation times in knee cartilage with osteoarthritis. Magn Reson Med 2009;61(6):1310-1318.

78. Boos N, Wallin A, Schmucker T, Aebi M, Boesch C. Quantitative MR imaging of lumbar intervertebral disc and vertebral bodies: methodology, reproducibility, and preliminary results. Magn Reson Imaging 1994;12(4):577-587.

79. Muller RN, Gillis P, Moiny F, Roch A. Transverse relaxivity of particulate MRI contrast media: from theories to experiments. Magn Reson Med 1991;22(2):178-182; discussion 195-176.

80. Miller AJ, Joseph PM. The use of power images to perform quantitative analysis on low SNR MR images. Magn Reson Imaging 1993;11(7):1051-1056.

81. Yablonskiy D, Haacke, EM. Theory of NMR signal behavior in magnetically inhomogeneous tissues: the static dephasing regime. Magn Reson Med 1994;32(6):749-763.

82. Cunningham CH, Arai T, Yang PC, McConnell MV, Pauly JM, Conolly SM. Positive contrast magnetic resonance imaging of cells labeled with magnetic nanoparticles. Magn Reson Med 2005;53(5):999-1005.

83. Elisseeff J, Ferran A, Hwang S, Varghese S, Zhang Z. The role of biomaterials in stem cell differentiation: applications in the musculoskeletal system. Stem Cells Dev 2006;15(3):295-303.

84. Arbab AS, Yocum GT, Rad AM, Khakoo AY, Fellowes V, Read EJ, Frank JA. Labeling of cells with ferumoxides-protamine sulfate complexes does not inhibit function or differentiation capacity of hematopoietic or mesenchymal stem cells. NMR Biomed 2005;18(8):553-559.

85. O'Halloran D M, Pandit AS. Tissue-Engineering Approach to Regenerating the Intervertebral Disc. Tissue Eng 2007.

86. Brandl F, Sommer F, Goepferich A. Rational design of hydrogels for tissue engineering: impact of physical factors on cell behavior. Biomaterials 2007;28(2):134-146.

87. Peretti GM, Randolph MA, Villa MT, Buragas MS, Yaremchuk MJ. Cell-based tissue-engineered allogeneic implant for cartilage repair. Tissue Eng 2000;6(5):567-576.

88. Sykova E, Jendelova P. Magnetic resonance tracking of implanted adult and embryonic stem cells in injured brain and spinal cord. Ann N Y Acad Sci 2005;1049:146-160.

89. Masaryk TJ, Ross JS, Modic MT, Boumphrey F, Bohlman H, Wilber G. High-resolution MR imaging of sequestered lumbar intervertebral disks. AJR Am J Roentgenol 1988;150(5):1155-1162.

90. Pearce RH, Thompson JP, Bebault GM, Flak B. Magnetic resonance imaging reflects the chemical changes of aging degeneration in the human intervertebral disk. J Rheumatol Suppl 1991;27:42-43.

91. Raininko R, Manninen H, Battie MC, Gibbons LE, Gill K, Fisher LD. Observer variability in the assessment of disc degeneration on magnetic resonance images of the lumbar and thoracic spine. Spine 1995;20(9):1029-1035.

92. Schiebler ML, Camerino VJ, Fallon MD, Zlatkin MB, Grenier N, Kressel HY. In vivo and ex vivo magnetic resonance imaging evaluation of early disc degeneration with histopathologic correlation. Spine 1991;16(6):635-640.

93. Tertti M, Paajanen H, Laato M, Aho H, Komu M, Kormano M. Disc degeneration in magnetic resonance imaging. A comparative biochemical, histologic, and radiologic study in cadaver spines. Spine 1991;16(6):629-634.

94. Thompson JP, Pearce RH, Schechter MT, Adams ME, Tsang IK, Bishop PB. Preliminary evaluation of a scheme for grading the gross morphology of the human intervertebral disc. Spine 1990;15(5):411-415.

95. Saldanha KJ, Piper SL, Ainslie KM, Kim HT, Majumdar S. Magnetic resonance imaging of iron oxide labelled stem cells: applications to tissue engineering based regeneration of the intervertebral disc. Eur Cell Mater 2008;16:17-25.

96. Regatte RR, Akella SV, Borthakur A, Kneeland JB, Reddy R. Proteoglycan depletion-induced changes in transverse relaxation maps of cartilage: comparison of T2 and T1rho. Acad Radiol 2002;9(12):1388-1394.

97. Regatte RR, Akella SV, Borthakur A, Kneeland JB, Reddy R. In vivo proton MR three-dimensional T1rho mapping of human articular cartilage: initial experience. Radiology 2003;229(1):269-274.

98. Duvvuri U, Reddy R, Patel SD, Kaufman JH, Kneeland JB, Leigh JS. T1rho-relaxation in articular cartilage: effects of enzymatic degradation. Magn Reson Med 1997;38(6):863-867.

99. Johnstone B, Hering TM, Caplan AI, Goldberg VM, Yoo JU. In vitro chondrogenesis of bone marrow-derived mesenchymal progenitor cells. Exp Cell Res 1998;238(1):265-272.

100. Hinds KA, Hill JM, Shapiro EM, Laukkanen MO, Silva AC, Combs CA, Varney TR, Balaban RS, Koretsky AP, Dunbar CE. Highly efficient endosomal labeling of progenitor and stem cells with large magnetic particles allows magnetic resonance imaging of single cells. Blood 2003;102(3):867-872.

101. Li X, Han ET, Busse RF, Majumdar S. In vivo T(1rho) mapping in cartilage using 3D magnetization-prepared angle-modulated partitioned k-space spoiled gradient echo snapshots (3D MAPSS). Magn Reson Med 2008;59(2):298-307.

102. Shapiro EM, Skrtic S, Sharer K, Hill JM, Dunbar CE, Koretsky AP. MRI detection of single particles for cellular imaging. Proc Natl Acad Sci U S A 2004;101(30):10901-10906.

103. Sumner JP, Shapiro EM, Maric D, Conroy R, Koretsky AP. In vivo labeling of adult neural progenitors for MRI with micron sized particles of iron oxide: quantification of labeled cell phenotype. Neuroimage 2009;44(3):671-678.

104. Williams JB, Ye Q, Hitchens TK, Kaufman CL, Ho C. MRI detection of macrophages labeled using micrometer-sized iron oxide particles. J Magn Reson Imaging 2007;25(6):1210-1218.

105. Shapiro EM, Medford-Davis LN, Fahmy TM, Dunbar CE, Koretsky AP. Antibody-mediated cell labeling of peripheral T cells with micron-sized iron oxide particles (MPIOs) allows single cell detection by MRI. Contrast Media Mol Imaging 2007;2(3):147-153.

106. Delo DM, Olson J, Baptista PM, D'Agostino RB, Jr., Atala A, Zhu JM, Soker S. Non-invasive longitudinal tracking of human amniotic fluid stem cells in the mouse heart. Stem Cells Dev 2008;17(6):1185-1194.

107. Amsalem Y, Mardor Y, Feinberg MS, Landa N, Miller L, Daniels D, Ocherashvilli A, Holbova R, Yosef O, Barbash IM, Leor J. Iron-oxide labeling

and outcome of transplanted mesenchymal stem cells in the infarcted myocardium. Circulation 2007;116(11 Suppl):I38-45.
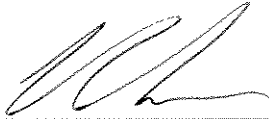
108.    Jing XH, Yang L, Duan XJ, Xie B, Chen W, Li Z, Tan HB. In vivo MR imaging tracking of magnetic iron oxide nanoparticle labeled, engineered, autologous bone marrow mesenchymal stem cells following intra-articular injection. Joint Bone Spine 2008;75(4):432-438.

109.    Erickson IE, Huang AH, Chung C, Li RT, Burdick JA, Mauck RL. Differential maturation and structure-function relationships in mesenchymal stem cell- and chondrocyte-seeded hydrogels. Tissue Eng Part A 2009;15(5):1041-1052.

110.    Heymer A, Haddad D, Weber M, Gbureck U, Jakob PM, Eulert J, Noth U. Iron oxide labelling of human mesenchymal stem cells in collagen hydrogels for articular cartilage repair. Biomaterials 2008;29(10):1473-1483.

111.    Taylor C, Carballido-Gamio J, Majumdar S, Li X. Comparison of quantitative imaging of cartilage for osteoarthritis: T2, T1rho, dGEMRIC and contrast-enhanced computed tomography. Magn Reson Imaging 2009;27(6):779-784.

112.    Kostura L, Kraitchman DL, Mackay AM, Pittenger MF, Bulte JW. Feridex labeling of mesenchymal stem cells inhibits chondrogenesis but not adipogenesis or osteogenesis. NMR Biomed 2004;17(7):513-517.

113.    Saldanha KJ, Doan RP, Ainslie KM, Desai TA, Majumdar S. Micrometer-sized iron oxide particle labeling of mesenchymal stem cells for magnetic resonance imaging-based monitoring of cartilage tissue engineering. Magn Reson Imaging;29(1):40-49.

114.    Genove G, DeMarco U, Xu H, Goins WF, Ahrens ET. A new transgene reporter for in vivo magnetic resonance imaging. Nat Med 2005;11(4):450-454.

**Publishing Agreement**

*It is the policy of the University to encourage the distribution of all theses, dissertations, and manuscripts. Copies of all UCSF theses, dissertations, and manuscripts will be routed to the library via the Graduate Division. The library will make all theses, dissertations, and manuscripts accessible to the public and will preserve these to the best of their abilities, in perpetuity.*

***Please sign the following statement:***

*I hereby grant permission to the Graduate Division of the University of California, San Francisco to release copies of my thesis, dissertation, or manuscript to the Campus Library to provide access and preservation, in whole or in part, in perpetuity.*

_____          5/27/11
Author Signature                                                        Date